INFORMATION TO USERS

This manuscript has been reproduced from the microfilm master. UMI films the text directly from the original or copy submitted. Thus, some thesis and dissertation copies are in typewriter face, while others may be from any type of computer printer.

The quality of this reproduction is dependent upon the quality of the copy submitted. Broken or indistinct print, colored or poor quality illustrations and photographs, print bleedthrough, substandard margins, and improper alignment can adversely affect reproduction.

In the unlikely event that the author did not send UMI a complete manuscript and there are missing pages, these will be noted. Also, if unauthorized copyright material had to be removed, a note will indicate the deletion.

Oversize materials (e.g., maps, drawings, charts) are reproduced by sectioning the original, beginning at the upper left-hand corner and continuing from left to right in equal sections with small overlaps. Each original is also photographed in one exposure and is included in reduced form at the back of the book.

Photographs included in the original manuscript have been reproduced xerographically in this copy. Higher quality 6" x 9" black and white photographic prints are available for any photographs or illustrations appearing in this copy for an additional charge. Contact UMI directly to order.
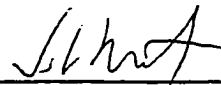
UMI®

Bell & Howell Information and Learning
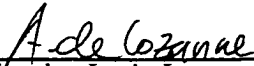300 North Zeeb Road, Ann Arbor, MI 48106-1346 USA
800-521-0600

Copyright

by

Koki Mochizuki

1998

Vortex Motion Studies of Superconductors

Using Mechanical Oscillators

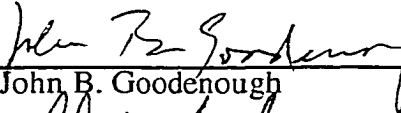**Approved by**
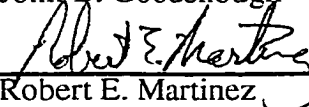**Dissertation Committee:**

_____
John T. Markert, Supervisor

_____
Alejandro L. de Lozanne

_____
James L. Erskine

_____
John B. Goodenough

_____
Robert E. Martinez

Vortex Motion Studies of Superconductors
Using Mechanical Oscillators

by

Koki Mochizuki, M.S.

Dissertation

Presented to the Faculty of the Graduate School of

The University of Texas at Austin

in Partial Fulfillment

of the Requirements

for the Degree of

Doctor of Philosophy

The University of Texas at Austin
December, 1998

UMI Number: 9937099

UMI

300 North Zeeb Road
Ann Arbor, MI 48103

Acknowledgments

I would like to acknowledge foremost Dr. Markert for his support. My project was tricky, to say the least. I would have given up a long time ago had his persistence and endless suggestions not sustained me. Not only did I learn so much from him, but also I truly enjoyed working with him. My friends on the thirteenth floor of RLM made my everyday life enjoyable and stimulating. Life in the physics graduate program tends to be stressful, but I managed to get through because of them. Especially I would like to thank Glenn Teeter for his friendship and help. I will miss coffee breaks with Ulrich and Jim. I further acknowledge my friends from church, especially Eri, Sarah and Elaine. Their prayers and friendship were a big help and comfort. Lastly, I want to express my gratitude to my parents for raising me in a loving family and for letting me pursue my dream. Thank you.

Vortex Motion Studies of Superconductors
Using Mechanical Oscillators

Publication No._____

Koki Mochizuki, Ph.D.

The University of Texas at Austin, 1998

Supervisor: John T. Markert

Results of direct measurements of the transverse force on moving vortices in single-crystal high-T_c superconductors using high-Q, double-torsional, single-crystal silicon mechanical oscillators are reported. The equation of motion for a vortex has been controversial for more than thirty years, with estimates of the transverse force differing by several orders of magnitude. Indirect measurements (e.g., Hall effect) have many complications. We have designed and built an apparatus to measure the force directly; our technique applies magnetic flux locally to the center of a single crystal, avoiding edge-pinning effects. For Bi2212, we have found that the upper limit of the transverse force per unit length is 2×10^{-12} N/m per vortex when the vortex velocity is 7.5×10^{-4} m/s. Using a conservative estimate $n_s = 5 \times 10^{26}$ m^{-3} and the form of the transverse force $F = \alpha \frac{h}{2} n_s v \times \hat{z}$, our data indicates $\alpha \leq 0.02$. This is much less than the classical result $\alpha = 1$, a value also obtained by recent theories. Our results support alternate theories where $\alpha \ll 1$ is predicted.

v

Table of Contents

vi

List of Tables

List of Figures

xiv

xvi

xvii

xviii

xix

xx

Chapter 1: Introduction

During my doctoral program, I have studied various aspects of superconductivity and magnetism. However, for the sake of coherence, I write only about vortex studies in superconductors in this dissertation. The forces on a vortex seem to be simple, yet their study has fueled controversy for many decades. More than 30 years ago, Nozière and Vinen wrote "There is, however, a certain freedom in the way in which the final equations may be written, so that this controversy is partly a matter of semantics.[1]" Though thirty years have passed, the situation has not changed. Sonin wrote in his paper published in 1997 "Among the sources of controversy there is semantics. Therefore it is important to define force terminology from the very beginning.[2]" Researchers don't all use the same 'language' to attack the problem. As a result, "Despite the tremendous progress made, however, the answer to one of the simplest questions, namely, the form of the equation of motion for a single isolated vortex, remains controversial.[3]"

It is difficult to determine the transverse force experimentally. Hall measurements have been used to determine the force. However, such indirect measurements have many complications. Therefore, we have designed and built an apparatus to measure the force directly.

---

[1] P. Nozière and W.F. Vinen, *Phil. Mag.* 14, 667, (1966)
[2] E.B. Sonin, *Phys. Rev. B* 55, 485, (1997).
[3] M.R. Geller, C. Wexler and D.J. Thouless, *Phys. Rev. B* 57, R8119 (1998).

1

1.1. ANOMALOUS HALL EFFECT

The Hall effect was first observed by Edwin Hall in 1879. As we have learned in a freshman physics course, charged particles experience a force when they move in a magnetic field. To refresh our memory let me explain the regular Hall effect. Let us think of a rectangular slab of metal. The applied field is assumed to be normal to the surface of the slab. The transport current is along the length of the slab. Because of the Lorentz force $f = qv \times B$, the carriers (either electrons or holes) are pushed to one side of the slab. Since they are charged, a non-uniform distribution of charged particles causes an electric field E across the width of the slab such that the forces on the charged particles will cancel each other in equilibrium. Thus, $E = vB$, if the transport current is perpendicular to the magnetic field. The transport current is $I = nqAv$, where n and A are the number density of the charged particles and the cross sectional area of the slab, respectively. Because $V = Ed$, where d is the width of the slab, the Hall voltage is

$$V_H = \frac{IBd}{nqA} = \frac{IB}{nqt},$$

where t is the thickness of the slab. The quantity $1/nq$ is called the Hall coefficient. From the sign and the amplitude of the Hall voltage one can tell the type of the carriers and their density. Conversely, if a known material and current are used, the magnetic field that penetrates the material can be calculated from the Hall voltage. The Hall effect is a very effective tool to study materials.

Because of the long tradition of the Hall effect measurements, it was natural that researchers measured the Hall voltage on high-T_c superconductors to

2

study their properties. However, the measured Hall voltage was all but ordinary; the sign of the voltage changed as high-T_c superconductors were cooled down below T_c. This anomaly turned out to be common among high-T_c superconductors, but is not limited to them; the sign change has been also observed for conventional vanadium and niobium superconductors.[4,5] Hagen *et al.*[6] have written a good review paper on this topic. Figure 1.1 epitomizes the anomalous Hall effect. Take $YBa_2Cu_3O_{7-\delta}$ for example. Above its T_c, the Hall resistivity ρ_{xy} ($=E_y/j_x$ for $B = B_z$) was positive since the carriers in the compound are holes like most of the high-Tc superconductors. However, as the temperature drops, the Hall resistivity begins to drop even at temperatures well-above T_c. The Hall resistivity keeps dropping and becomes negative at a temperature below T_c. Upon further cooling, the Hall resistivity began an upward trend to zero. A $Nd_{1.85}Ce_{0.15}CuO_{4-y}$ crystal showed a similar but opposite change in the Hall resistivity. Because this superconductor is electron-doped, the sign of the Hall resistivity is negative. Like YBCO, its sign changes at some temperature below T_c.

---

[4] A. K. Niessen, F. A. Staas, and C. H. Weijsenfeld, Phys. Lett. **25 A**, 33 (1967).
[5] K. Noto, S. Shinzawa, and Y. Muto, Solid State Commun. **18**, 1081 (1976).
[6] S. J. Hagen et al., Phys. Rev. B **47**, 1064 (1993).

3
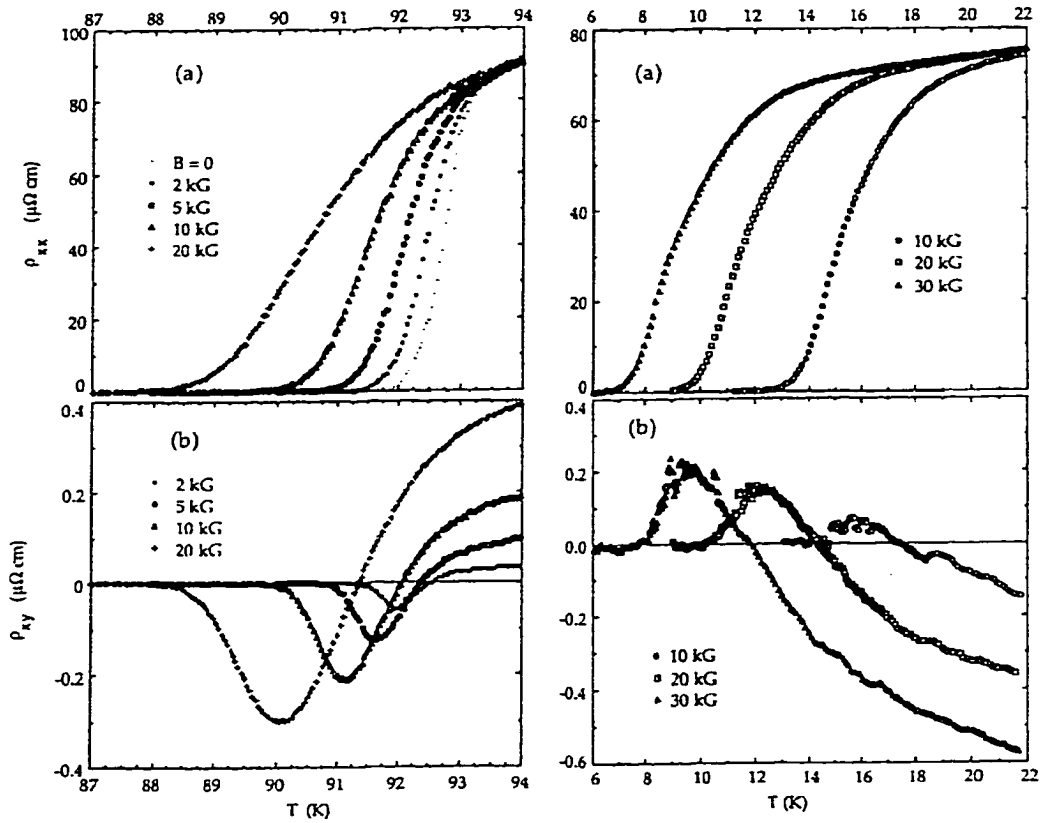
Fig. 1.1. Resistivity (top) and the Hall resistivity (bottom) for epitaxial YBa$_2$Cu$_3$O$_{7-\delta}$ film (left) and Nd$_{1.85}$Ce$_{0.15}$CuO$_{4-y}$ crystal (right). (Taken from Hagen et al.[7])

As Bardeen and Stephen wrote in their paper,[8] there can be no interior stresses associated with supercurrent flow. Therefore the Hall effect in superconductors, which is a stress, must come from the normal component or the boundary; namely vortices. So, if we interpret the sign change in a hydrodynamic

---

[7] S. J. Hagen et al., Phys. Rev. B **47**, 1064 (1993).
[8] J. Bardeen and M. J. Stephen, Phys. Rev. **140**, A1197 (1965).

4

picture, vortices seem to move sometimes along and other times against the transport current. This behavior is very different from the conventional vortex motion we know from the fluid dynamics, where vortices flow downstream with transport current. Therefore, numerous theories have been proposed to account for the anomaly, such as flux-pinning forces, thermoelectric effect, and two-band models. However, as Hagen *et al.* pointed out, the anomaly has been observed in so many materials that we should treat it as a general property. He concluded that the anomalous Hall behavior is pervasive among moderately clean ($l/\xi \sim 0.5$–5) superconductors, but does not occur in either very clean ($l >> \xi$) or dirty ($l << \xi$) cases. Here, l is the mean free path and ξ is the superconducting coherence length. They also state that a correct model of vortex dynamics should be able to explain the sign reversal. Hence it is important to know more about the motion of a vortex without relying on indirect methods such as the Hall effect measurement.

1.2. VORTEX MOTION

1.2.1. Two Simple Models

Many researchers have tried to understand the motion of vortices. In such attempts two simple models of vortex motion were published in the sixties; they were the Bardeen-Stephen model[9] (B-S model hereafter) and the Nozières-Vinen model[10] (N-V model hereafter). The B-S model assumes that the superconductor is local, which means that the order parameter $|\Psi|$ depends only on the local value of the velocity of superconducting carriers. It further assumes that the core

---

[9]J. Bardeen and M. J. Stephen, Phys. Rev. **140**, A1197 (1965).
[10]P. Nozières and W. F. Vinen, Phil. Mag. **14**, 667 (1966).

5

of a vortex is fully normal. The N-V model is very similar to the B-S model, but the transition region is shrunk to a mere discontinuity. Hence the N-V model assumes a plain cylinder of normal material. According to the B-S model, half the force on the vortex is experienced in the transition region.
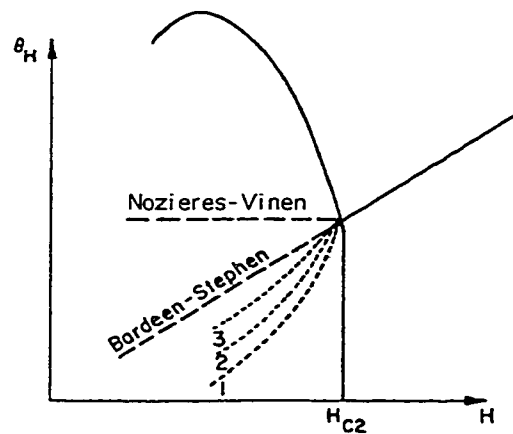
Fig. 1.2.   Theoretical and experimental Hall angles as a function of applied field. The N-V model predicts a constant Hall angle up to H_{c2} while the B-S model predicts Hall angle to be proportional to the applied field. The full line is an experimental result on dirty NbTa alloys. The dotted lines are results on very pure Nb. (Taken from Nozières and Vinen.)

Though the difference between them may seem small, the consequences of the two models are strikingly different. The B-S model predicts that the Hall angle is the same as that of the normal state, which is

$$\tan \theta_H = \frac{eH}{mc}\tau.$$

In contrast, the N-V model predicts that the Hall angle would be

6

$$\tan\theta_H = \frac{eH_{c2}}{mc}\tau.$$

Consequently, according to B-S model the Hall angle is proportional to the applied magnetic field, while the Hall angle should be constant at fields lower than H_{c2} according to N-V model (Fig. 1.2). However, neither model successfully explains the sign reversal of the Hall voltage.

1.2.2. Attempts to Explain the Hall Anomaly

Interesting observations like the Hall anomaly caused renewed interest in the problem. To explain the anomaly in the Hall effect, new theoretical calculations have been done using the time-dependent Ginzburg-Landau (TDGL) equations. In the dirty limit ($l \ll \xi$) the sign-reversal can be intrinsic and depends on the details of the normal-state electron spectrum[11]. In this limit the Hall effect is very small. Calculation in the clean limit has been done by Kopnin and Lopatin.[12] They found that in the superclean limit ($l \gg (E_F/\Delta)\xi$, where E_F is the Fermi energy and Δ is the superconducting gap), the Hall angle is similar to that for the normal state, namely $\pi/2$. In the moderately clean limit ($\xi \ll l \ll (E_F/\Delta)\ \xi$), the Hall angle is small yet the sign of the Hall effect may differ from that in the normal state depending on the detailed structure of the Fermi surface. In the super-clean limit, Blatter et al. [13] showed that there are three forces on vortices. The first is the Lorentz force, which is

$$f_L = \frac{\Phi_0}{c}j\times\hat{z},$$

[11] A. I. Larkin and Yu. N. Ovchinnikov, Phys. Rev. B **51**, 5965 (1995).
[12] N. B. Kopnin and A. V. Lopatin, Phys. Rev. B **51**, 16291 (1995).
[13] Blatter et al., Rev. Mod. Phys. **66**, 1125 (1994).

7

where j is the current density and $\hat{z}$ is a unit vector parallel to the field. In the presence of scattering, this Lorentz force has to balance the friction force and the Hall force at steady state (i.e., no net force):

$$\frac{\Phi_0}{c}j\times\hat{z} = \eta_l v_v + \alpha_l v_v\times\hat{z} \, ,$$

where v_v is the vortex velocity. The two coefficients are the viscosity

$$\eta_l = \frac{\Phi_0}{c}\rho_s\frac{\omega_0\tau}{1+\omega_0^2\tau^2}$$

and the transverse force coefficient

$$\alpha_l = \frac{\Phi_0}{c}\rho_s\frac{\omega_0^2\tau^2}{1+\omega_0^2\tau^2} \, ,$$

where ω_0 is the core level spacing and τ is the relaxation time. If there is no scattering, the net force on the vortex is called the Magnus force:

$$f_M = \rho_s\frac{\Phi_0}{c}(v_s-v_v)\times\hat{z} \, .$$

So, in the super-clean limit, the Magnus force is the only force on the vortex and the vortex flows with the transport current. The so-called Hall angle is defined as

$$\tan\theta_{Hall} = \frac{v_v{}^{||}}{v_v{}^{\perp}} = \frac{\alpha_l}{\eta_l} \, .$$

Usually the Hall angle is very small. Only in the super-clean limit does the Hall angle become $\pi/2$. The third force acting on the vortex is the pinning force, but we ignore this force for now.

8

1.2.3. New Controversy

Ao and Thouless concluded by Berry's phase calculations[14] that in the clean limit the vortex velocity part of transverse force is

$$F = \frac{h}{2} n_s v \times \hat{z} .$$

However, their arguments depended on a detailed model of the vortex structure. In a subsequent paper, Thouless, Ao and Niu[15] considered a single, isolated vortex force to move through an infinite superfluid with uniform velocity v_v by some moving pinning potential. They concluded that the transverse force has the form

$$F_v = \rho_s \kappa_s \times v_v.$$

Wexler[16] argued that the above force is a universal vortex velocity part of the Magnus force. He calculated the superfluid velocity part of the Magnus force and showed it is

$$F_s = -\rho_s \kappa_s \times v_s.$$

The most general Galilean invariant transverse force can be written as

$$F = A\kappa \times (v_v - v_s) + B\kappa \times (v_v - v_n)$$

where v_v, v_s, and v_n are velocities of a vortex, superfluid transport current, and normal transport current, respectively. He also determined that the unknown coefficient A is

$$A = \rho_s \frac{h}{m}.$$

---

[14]P. Ao and D. J. Thouless, Phys. Rev. Lett. **70**, 2158 (1993).
[15]D. J. Thouless, P. Ao and Q. Niu, Phys. Rev. Lett. **76**, 3758 (1996).
[16]C. Wexler, Phys. Rev. Lett. **79**, 1321 (1997).

9

where $\kappa = h/m$ in the case of a quantized vortex. Considering Thouless, Ao and Niu's result, it can be shown that

$$A + B = \rho_s \frac{h}{m}.$$

Thus, the coefficient B vanishes, meaning that there is no transverse force depending on the normal fluid velocity. Wexler concluded that the total transverse force per unit length acting on a vortex is

$$F = \rho_s \frac{h}{m} \hat{z} \times (v_v - v_s).$$

His conclusion stirred quite a controversy. For example, H. E. Hall and J. R. Hook wrote a comment[17] pointing out that Wexler's conclusion conflicts with the experimental facts for vortices in superfluid ^{3}He and ^{4}He. They wrote that Wexler's B has been deduced from mutual friction experiments. The transverse force due to the normal fluid is usually quoted as a dimensionless parameter $d = -B/A$. Therefore, they believe that there is an error in either Wexler's argument or that of Thouless, Ao and Niu. Since Wexler's argument is particularly straightforward, they suspect that Thouless, Ao and Niu's argument is wrong.

Feigel'man et al.[18] argued that Thouless, Ao and Niu's conclusion is correct only for the Galilean invariant case, where the density n and the superfluid density n_s coincide. Besides, superconductors are not Galilean invariant. According to their phenomenological derivation, the transverse force should be, in general,

$$F = \frac{h}{2}(n_\infty - n_0)\hat{z} \times v_v .$$

---

[17]H. E. Hall and J. R. Hook, Phys. Rev. Lett. **80**, 4356 (1998).
[18]M. V. Feigel'man et al., JETP Lett. **62**, 834 (1995).

10

The major differences between this transverse force and the Magnus force are 1) the n_∞, the density far from the vortex, is the total density rather than the superfluid density and 2) the additional term proportional to n_0, the density at the vortex axis, exists.

But when $n_\infty - n_0$ is much smaller than n_∞, the scattering should be treated more precisely. It turns out that the transverse force is

$$F = \frac{h}{2}(n_\infty - \frac{n_0}{1+(\omega_0\tau)^2})v_v\times\hat{z} .$$

The first term is the Magnus force and the second term is due to impurity scattering. This second force almost cancels the Magnus force in a conventional situation.

I have briefly reviewed the situation of the field. Clearly, theorists do not agree with one another. Even the terminology 'force' is controversial.[19] Experiments are difficult to interpret as well. So far, most of the measurements have been indirect, such as the Hall measurements. But interpretation of the Hall effect is not straightforward because it depends on the shape of the Fermi surface, the carrier type, and other effects, such as the presence of defects in the vortex lattice. Thus, we decided to measure the force on vortices directly. By doing so, we might be able to determine which theory is correct.

1.3. EXPERIMENTS

There are many theories of vortex motion that try to account for the Hall anomaly described above. To avoid the complication associated with the Hall

---

[19]E.B. Sonin, Phys. Rev. B **55**, 485, (1997).

11

effect, it would be beneficial to measure the force on vortices directly, without relying on Hall voltage measurements. Fortunately, we can do this kind of measurement with a double-torsional oscillator. So far, one group has done a similar experiment.[20] In their study, they used a superconducting film on a cantilever, which had a resonance frequency of about 400 Hz. They compared the amplitude of the transverse force on the superconducting film with the two theories and concluded that the Ao-Thouless theory fit the data best. Their experiment could only estimate that the force agreed with the Ao-Thouless within a factor "of order of" unity.
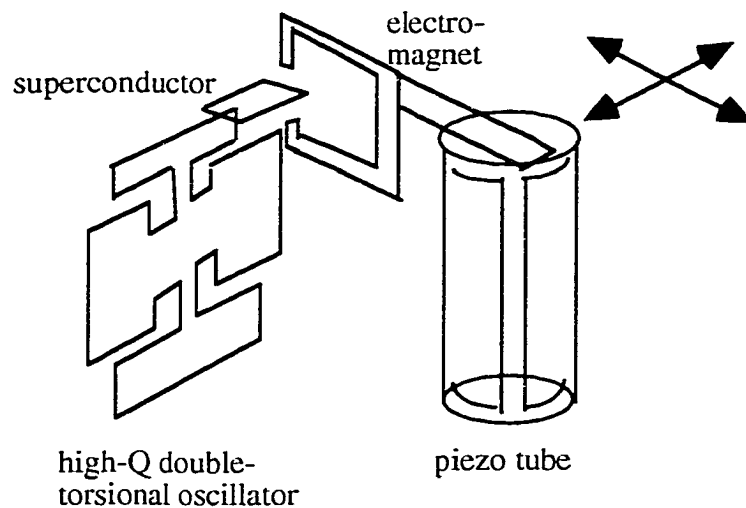
Fig. 1.3.   Experimental setup to measure the forces on a superconductor. If the piezo tube is driven perpendicular to the oscillator surface, the pinning/viscous forces will excite oscillator motion. If the piezo is driven parallel to the oscillator, then the transverse forces will excite oscillator motion.

[20]X.-M. Zhu, E. Brändström and B. Sundqvist, Phys. Rev. Lett. 78, 122 (1997).

12

Our advantage over the previous experiment is that our oscillators have very high Q's, and thus we can detect proportionally smaller forces. Using the same kind of oscillators, we have studied the thermally activated depinning. In this study we drove an oscillator in a constant magnetic field. We found two peaks in the dissipation curve as we swept the temperature.

The principle of our transverse force measurement is straightforward. The experimental setup is shown in Fig. 1.3. First, we attach a superconductor to the head of an oscillator. In the dissipation study, the superconducting crystal was attached to the surface of an oscillator. In the current study, the crystal was attached to the top sidewall of an oscillator. The electromagnet has a core that is smaller than the crystal, so we eliminate edge effects. We move the magnet at the resonance frequency of the torsional oscillator by driving the piezo tube connected to the magnet. Vortices are dragged in the direction of magnet movement. Because the piezo tube has four quadrants, we can drive it in any direction. To study the pinning/viscous force, we drive the piezo perpendicular to the surface of the oscillator; this way, only forces which are along the vortex motion will be detected. To study transverse forces, we drive the piezo parallel to the oscillator surface, so that only forces perpendicular to the vortex motion will excite the oscillator.

1.4. ESTIMATES OF FORCES

Initially, we estimated the expected amplitude of the forces to make sure the project was feasible. The transverse force is expected to be smaller than the

13

pinning force. We estimate the amplitude of transverse force in the following way.

In the formula derived by Feigel'man *et al.*, we assume that $n_\infty = n_0$. The following estimated values are used to estimate the size of the transverse force.

The total density of electrons $n_e = 1 \times 10^{21}$ cm^{-3}

The velocity of the vortex: 0.23 mm/s (assume the piezo is driven 40 Å at 9 kHz (4 Å/V))

The energy scale of the core level spacing for YBCO: 10 K

The relaxation time: 10^{-13} sec

$(\omega_0 \tau)^2 \sim 0.001$

The thickness of the crystal: 0.01 mm

The number of vortices: $\dfrac{HA}{\Phi_0} = \dfrac{2 \times 10^4 \, G \, (0.02 \, cm)^2 \, \pi}{2 \times 10^{-7} \, G \, cm^2} = 1 \times 10^8$

Hence Feigel'man *et al.* predicts a transverse force on one vortex of 1×10^{-12} dyne. Hence, the oscillator will be driven by the force on all vortices, which is 1×10^{-4} dyne $= 1 \times 10^{-9}$ N. The transverse force according to Ao and Thouless is 1×10^{-9} dyne per vortex. This makes 1×10^{-1} dyne $= 1 \times 10^{-6}$ N on all the vortices.

As can be seen, predictions of the amplitude of the transverse force differ by three orders of magnitude. Moreover, the force sensitivity of our oscillator is $\sim 10^{-9}$ N when capacitive detection is used. Therefore, we concluded that the experiment would be feasible and that we should be able to set limits on the amplitude transverse forces.

14

Chapter 2: Fabrication of Experimental Components

2.1. OSCILLATOR FABRICATION—OVERVIEW
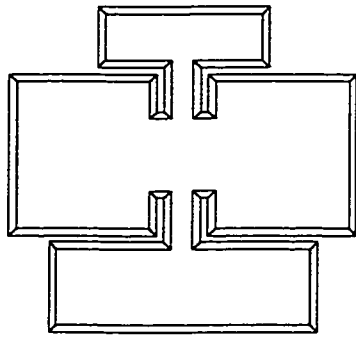
Fig. 2.1. A high-Q, double-torsional oscillator. The figure is two and half times the actual size. For example, the actual wing span is 0.70 inches.

The outline of the oscillator fabrication process is the following. First, photolithography was performed on wafers on which a 750 Å-thick silicon-nitride film had been deposited by Low Pressure Chemical Vapor Deposition (LPCVD). Then the nitride film was removed by Reactive Ion Etch (RIE). Up to this point the process was performed in the cleanroom at the Microelectronics and Engineering Research Center (MER) on the Pickle Research Campus. Then in our own lab we etched the wafers with KOH. Once we got oscillators, we deposited a thin layer of metal on them for conduction. Then we attached lead wires to the oscillators and put epoxy bases on them.

2.2. OSCILLATOR FABRICATION—DETAILS

In this section, we describe the details of each step of the oscillator fabrication process.

15

2.2.1. Silicon Wafers

Silicon wafers were purchased from Nova Electronic Materials, Inc.[1] The Specifications were P-type 4-inch (100) single-side polished[2] test wafers with 750 Å LPCVD Si_3N_4. The doping was low, so that the resistivity was more than 10 Ω-cm. The silicon nitride film was put on as a mask for KOH etch. I also tried (110) wafers to make oscillators. The crystallographic direction is critical for oscillator fabrication. Virtually, KOH does not etch silicon in <111> direction. Thus, careful alignment between the crystallographic direction of the wafer and the edges of patterns on the mask is essential.

(100) wafers

<111> directions in (100) wafer are 35.26° out of the wafer surface. The projections of the <111> onto the wafer are parallel and normal to the [110] primary flat. Since {111} planes are 90° to each other, all edges will be straight provided edges are perpendicular to each other and that edges are aligned either parallel or perpendicular to the primary flat.

However, the edge will not be vertical; rather, it will be at 54.74° with respect to the surface of the wafer. So, one side of the structure is smaller than the other side. The typical etchant for (100) wafer is $KOH:H_2O:Propanol =$ 200g:800cc:200cc. Alcohol reduces the etch rate for the <110> direction, which increases the relative etch rate for the <100> direction over the <110> direction.

---

[1]Phone 972-664-0550; fax 972-664-1589.
[2]Double-side polished wafers may enable us to make oscillators with higher Q's.

16

The temperature is about 80°C. Such an etch takes about one day for a 0.4 mm wafer. Lower temperature can be used to slow the etch rate.

There is an interesting paper on non-conventional alignment.[3] The authors aligned the edges 45° from the [110] flat in a (100) silicon wafer. By doing so, the {100} sidewalls were etched vertically although they suffered an undercut that is equal to the etch depth. This may be worth trying; we'll get vertical edges. They used $KOH:H_2O = 41: 59$ in weight. The temperature they used was 55°C.

(110) wafers

For (110) wafers, the <111> directions are in the wafer plane and are 35.26° from the [110] primary flat. So, {111} planes will not be 90° to each other; rather they make 109.48° and 70.52°. Therefore one has to choose one direction in which the edge will be straight and smooth. Edges in other directions may turn out jagged. There is an advantage also; because <111> is in the wafer plane, {111} planes are normal to the wafer surface. Therefore, the etched cross-section will be vertical. When one has to make small features, this fact may be important. The typical etchant for (110) is $KOH:H_2O = 35g: 65cc$. The temperature is about 80°C.

---

[3]G. Schröpfer et al., J. Micromech. Microeng. 7, 71 (1997).

17

2.2.2. Photolithography

First, I applied the positive photoresist AZ5209E on a wafer that had been placed on the spinner. The wafer was spun at 4000 rpm for 30 seconds. Then, the wafer was placed on a hotplate[4] that I had preset to be 90 °C. I was told that 30 seconds was enough to dry the photoresist; but to make sure, I left wafers on the hotplate for a few minutes. After the photoresist was applied to all the wafers, I set the mask and the wafer to the aligner and exposed it to UV light. Then I developed the pattern with the developer AZ425. After development, I set the wafer on the hotplate at 120 °C for a post-bake . The wafers are ready for RIE.

2.2.3. Reactive Ion Etch (RIE)

After lithography was done, silicon nitride had to be patterned. To etch silicon nitride (Si_3N_4), RIE was used. Wet etch is not practical; straight HF eats photoresist fast and Buffered Oxide Etchant (BOE) cannot etch nitride. One could use boiling sulfuric acid, but RIE can etch thin films quickly. Besides, RIE etch is anisotropic. The following setting was used to etch a 750 Å silicon nitride film with the orange RIE in the cleanroom. Gas mixture was CHF_3 65% (of 100 sccm) and O_2 32% (of 10 sccm). The pressure of the gas mixture was set to 50 mTorr. An RF power of 75 W was used to etch the siliconnitride film. After being etched for two minutes, the 750 Å-nitride layer was completely removed. Film thickness was checked with an instrument and the thickness was below the resolution limit of the instrument, which was 20 Å.

---

[4]The reason I didn't use the regular oven was that hotplate was much faster. For a person who doesn't have an office at MER, I think the hotplate is much better than the oven.

18

After the RIE is done, the photoresist can be stripped off with acetone and an ultrasonic cleaner or with piranha (H_2O_2: H_3PO_4 = 1:2 by volume). I used piranha with success. I followed the instructions in the cleanroom when I made piranha.

2.2.4. KOH Anisotropic Etch

I first used (110) wafers aligning the axes of the oscillators 35° away from the primary flat. The reasoning was that I could have sharp, nice edges on the top and the bottom of the wings and the heads. But the results were confusing. The edges of the oscillators were not straight; instead, some edges were etched at several angles. The axes of the oscillators were etched so thin that they almost disappeared.[5]

(100) wafers gave me much better results. Instead of weighing KOH, I just used 200 cc of KOH by volume. It turned out that 200 cc KOH is approximately 200 g. Since precise concentration of KOH is not critical, measuring volume is good enough. Then I added 800 cc deionized water while stirring the mixture.[6] Then I added 200 cc isopropyl alcohol to the mixture. I have learned that I should pour chemicals onto water to avoid any danger, but in reality, when I poured KOH pellets into water, I caused many splashes around the beaker, which had high concentration of KOH. So, pouring liquid to solid was better, in this case.

---

[5]For details see Koki's lab book 6:49–56.
[6]Unless being stirred continuously, the solution might begin to boil.

19

I made a 4"-wafer holder made of Teflon. It could hold two wafers at a time to improve the turn-round time. The solution was kept stirred with a stirrer. I used various temperatures from 60 to 80°C. It seemed that only etch rate was affected by the temperature change. To be safe, I turned off the heat during the night to avoid over-etch. Because 4" wafers are thicker than 3" ones, oscillators did not fall off the wafer after being etched completely. Hence, I removed the wafer from the KOH solution and rinsed with DI water while oscillators were still attached to it. Then I gently pressed the oscillators to release them from the wafer.

After successful etches, I obtained six oscillators per 4" wafer. To remove the nitride film, which was still on the oscillators after the KOH etch, I immersed the oscillators in 49% hydrofluoric acid (HF) for three to five minutes until all nitride was removed. Straight HF passivates silicon; so there's no need to worry about overetch. One simple way to judge if the nitride is gone is to see whether water wets oscillators or not. Water on bare silicon makes large beads and slides off oscillators very easily. Nitride, in contrast, wets. It is easy to tell by the color, too. After the nitride was removed, I rinsed the oscillators with water and dried them with a Kimwipe.

2.2.5. Metallization

Oscillators must be conductive on their surfaces. To make them conductive, I evaporated gold on them. First, I wrapped the neck and the head of the oscillators with thinly-sliced Teflon tape. This was done to avoid film

20

evaporation on these parts of the oscillators. The reason why I didn't want any film on the neck was that I didn't want any cause of possible loss of energy; since the film was composed of chromium and gold, it was softer than silicon crystal. Thus, it might cause energy loss. A conductive film on the head might cause eddy currents; to eliminate these possible energy loss mechanisms, I covered the head and the neck of the oscillators with Teflon tape before the metal evaporation process.

Then thin films of chromium (20 Å) and gold (100 Å) were evaporated on the oscillators in this order at the physics cryogenic shop. The oscillator wings had to be conductive because they act as plates of capacitors. The base and the lower neck had to be conductive because we had to bias the oscillator at some high voltage (typically 250 V) to have high enough sensitivity. The details of capacitive excitation and detection can be found elsewhere in this dissertation. The thickness of the film was finally settled to be 20 Å chromium followed by 100 Å gold. When I attached the oscillators to the ring-shaped holder at the cryogenic shop, I simply clamped the oscillators at the head over the Teflon tape. If an oscillator were clamped at the base, it would be inevitable to have shadows of the clamps on the base. So, clamping on the head is better. Before I settled to use the film thickness written above, I had tried thicker films to ensure good conductivity. First, 100 Å gold didn't even have gold color. Also, in order for chromium to be effective between silicon and gold, one book suggested a thickness of about 100 Å. Thus, I tried up to 50 Å chromium and 200 Å gold. Although 100 Å difference in film thickness shouldn't seem to make any difference, it actually made a large difference; when the thicker film was used the

21

highest quality factor was 3.0×10^5 while the thinner film was used the highest quality factor was 4.9×10^5. Therefore, I decided to use the thinner film; which was 20 Å chromium and 100 Å gold.

2.2.6. Lead Wire

Oscillators need to be biased when being used. Thus, after the conductive film was evaporated onto the oscillators I fixed a piece of 22 AWG solid tin-coated copper wire (0.025 inch diameter) with silver epoxy to the lower part of the base. I did not use copper sheet to make lead wires as previously. Round wires were good enough. To make the oscillators as parallel to their bases as possible during the base cure, I used one long wire (about 1.4 inch). This way, the wire was fixed at the both ends in the epoxy mold, which kept the oscillator from sliding during epoxy cure. I applied a small amount of silver epoxy at two points on the wire so that there were two contacts between the wire and the oscillator. The reason for this was to ensure good contacts between the lead wire and the oscillator; I have seen silver epoxy fail several times. If there are two contacts, the lead wire and the oscillator are in contact even if one of the silver epoxy contacts fails. Silver epoxy was cured at 175°C on a block of aluminum for a few minutes; this temperature gives the best property to the epoxy by promoting rapid shrinkage.

22

2.2.7. Epoxy Base

Then, I made epoxy bases. I've found that the combination of Stycast 2850 MT (blue resin) and Catalyst 11 has the least energy loss. Stycast 2850 MT has lots of fillings and they settle on the bottom. So, before each use, the entire contents must be stirred completely. After mixing the resin with the catalyst, the mixture was pumped on until trapped air disappeared. This process took about 5 to 10 minutes. Then the mixture was poured into a mold made of Teflon. A former student put Teflon tubing on the bottom to make sure that the oscillator didn't protrude from the bottom of epoxy base. But it could be omitted by fixing a wire low enough on the base and by using a mold that was designed so that the bottom of the oscillator couldn't reach the bottom of the mold. After wiping excessive epoxy from the mold, the oscillator was placed in the mold. I tried to position the oscillator so that it was vertical. Catalyst 11 requires curing at an elevated temperature. So I placed the mold in an oven at 75 °C overnight. Then, the temperature was raised to about 120 °C for a couple of hours. This postbake supposedly improves the property of epoxy. After this, the oscillator was ready for experiments.

2.3. ELECTROMAGNET

2.3.1. Magnet Core Materials

The electromagnet inside the probe creates magnetic flux in a superconductor. To excite the oscillator, on which the superconductor crystal was glued, the magnet was moved by a piezo tube in an arbitrary direction. There are

23

two desirable properties for the magnet core. First, we want a core that produces a high magnetic inductance because the higher the magnetic field, the greater the force on the oscillator due to a greater number of vortices. Also, vortices are depinned at lower temperature with higher field. We expect a larger force at lower temperature because the amplitude of the order parameter is larger. Second, we want to achieve a high field with a low current through the coil, thus with little heating, for temperature stability. To choose the right magnetic core for my experiment, one has to understand the basics of magnetic materials.
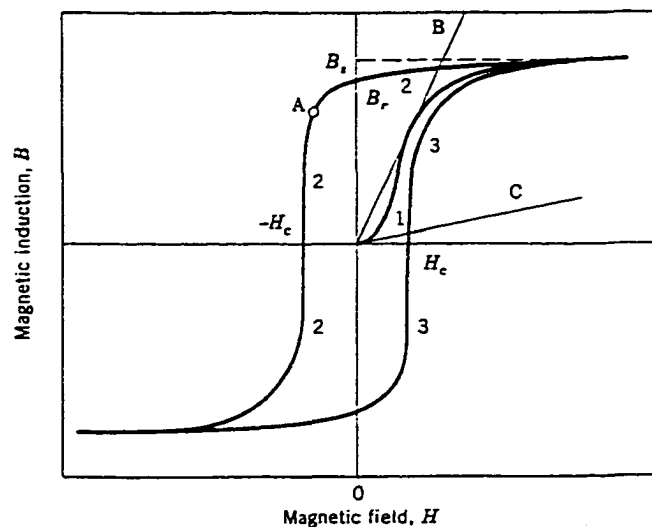
Fig. 2.2.   Magnetic hysteresis loop of an initially demagnetized material.

Figure 2.2 is a hypothetical magnetic hysteresis loop. B_s, B_r and H_c are called the saturation induction, the remanent induction, and the coercive force (or coercivity) of the magnetic material, respectively. Although the higher B_s, the

24

better for our experiment, we had to achieve saturation at a reasonable applied magnetic field because the coil wound around the core could not produce so much H field. Theoretically it produces 60 Oe.[7] In addition, heating from the coil turned out to be a problem; temperature change caused a resonance frequency shift and thus made interpretation of data difficult.

To achieve these goals I tried four kinds of pure metals or alloys. Readily available magnetic pure elements are iron and nickel. In addition to them, I attempted to make Supermendur and Supermalloy.

Supermalloy is an alloy consisting of 0.5% manganese, 5% molybdenum, 15% iron and 79% nickel by weight.[8] It has a remarkably high permeability of 75000. So, the virtue of using Supermalloy is that we can achieve its maximum induction with a low applied field, thus with small heating. However, its saturation induction is quite low: only 7800 gauss. The heat treatment is said to be the key to make Supermalloy. Closely controlled heat treatment is essential for all soft magnetic materials, but it is especially important for the Ni-Fe alloys. To make Supermalloy, the alloy has to be annealed at 1300°C in pure, high-quality, dry H_2 followed by an elaborate cooling cycle. It is said that the cooling rate is critical between 600°C and 300°C. The details of the heat treatment, however, were not available.

---

[7]Coil had 240 turns in 1 cm. Applied current was initially 0.2 A.
[8]Chih-Wen Chen, Magnetism and Metallurgy of Soft Magnetic Materials, North-Holland P.C., Amsterdam, 1977.

25
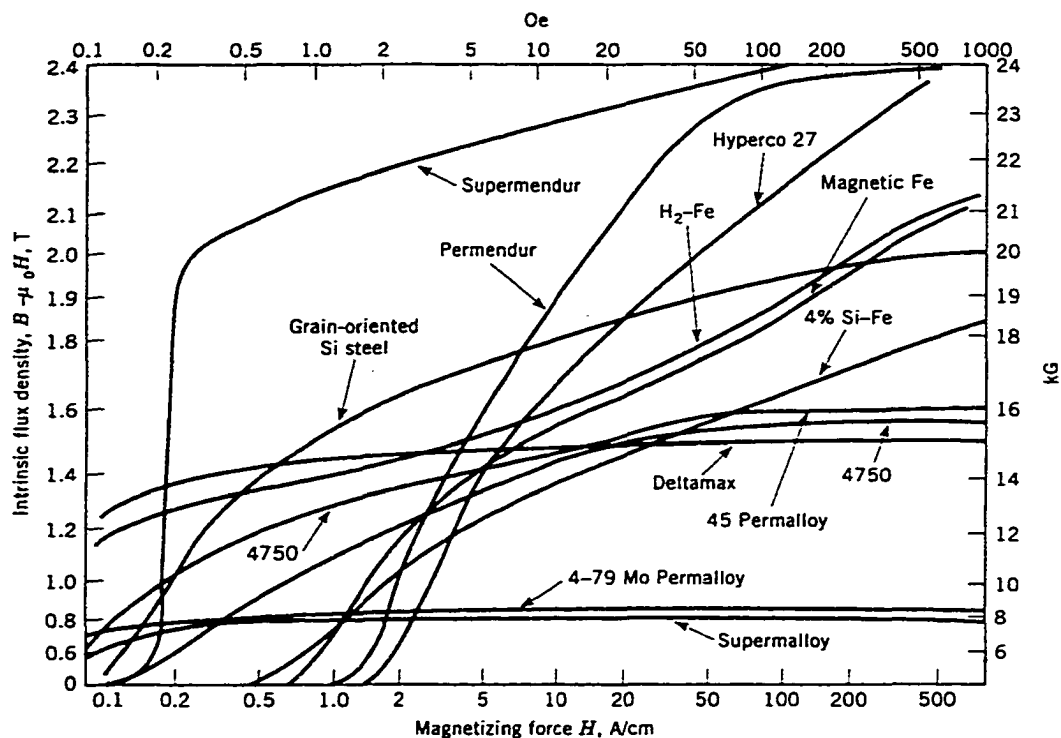
Fig. 2.3.   Magnetization curves of commercial soft magnetic materials. (Taken from Kirk-Othmer).

Supermendur seemed to be the best candidate for my experiment. It consists of 2% vanadium, 49% Cobalt and 49% iron by weight. Vanadium gives ductility to the alloy. It has a very high saturation induction of 2.3 T. In addition, its induction begins to rise sharply with an applied field of about 0.2 Oe (See Fig. 2.3). Once it gains its saturation induction, it retains 90% of its saturation induction even with the applied field turned off. The heat treatment for Supermendur is also complicated.[9] To remove interstitial impurities, wet and dry

[9] Kirk-Othmer ed., Encyclopedia of Chemical Technology, Fourth Ed., Vol. 15, John Wiley & Sons.

26

hydrogen treatment is necessary, followed by annealing in a magnetic field. Addition of vanadium requires quenching. By adding 4.5% Ni to the alloy, one can enhance the ductility. Moreover, it eliminates the need for close control during annealing. Brittleness of the alloy is a problem for my experiment. For this alloy, the details of the heat treatment were not available.

Although we want sharp transitions in the hysteresis loop when the magnet is on, it might be a tricky property for the experiment. To turn off the field, one has to apply the coercivity of 0.005 Oe for Supermalloy, 0.20 Oe for Supermendur. If the transition is steep, accurate control of the current to produce the coercivity would be difficult.
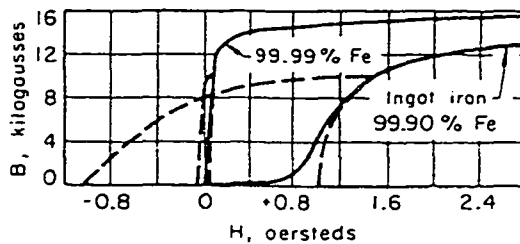
Fig. 2.4. Effect of iron purity on hysteresis loops. (Taken from Chih-Wen Chen[10])

Iron, on the other hand, has been well-known for thousands of years. Despite the old-fashioned image associated with iron, it has very attractive properties; its saturation is 2.15 T, which is just slightly shy of that of Supermendur. Moreover its permeability is as high as 227,000. In addition its hysteresis loss is quite small. The drawback of iron is its low resistivity (10 $\mu\Omega$-cm) compared to more modern alloys such as Supermalloy, whose resistivity is 60

[10]Chih-Wen Chen, Magnetism and Metallurgy of Soft Magnetic Materials, North-Holland P.C., Amsterdam, 1977.

27

$\mu\Omega$-cm. However this point would not pose any problem for my experiment since I use a dc-field, not an ac-field.

One important fact to be pointed out is that the purity of iron affects its properties dramatically. Figure 2.4 is a comparison of M-H curves and hysteresis loops for 99.99% pure iron and 99.9% pure iron. Solid curves are the magnetization curves and dotted curves are top halves of the hysteresis loops. As is apparent from the figure, an increase in purity from 99.9% to 99.99% dramatically improves both the magnetization curve and hysteresis loop.

The recommended heat treatments for the alloys was impossible for us to implement; first, small tube furnaces were rated for 1100°C, which means that it should not be used above 1000°C or their heating elements would burn out quickly. We had a large tube furnace, but it was rated for 1200°C; this meant that I could not anneal the alloys or metals in a specific gas flow (usually hydrogen) at the specified temperature. For example, Supermalloy requires annealing at 1300°C in hydrogen, but it was not within our reach. Hence, when I attempted to make Supermalloy, I placed the alloy in a tube furnace in hydrogen flow. Then I raised the temperature to 1200°C for only 13 minutes followed by lowering the temperature to 550°C at a rate of 1°C/min. Then I turned off the furnace at 550°C.

The heat treatment for iron requires very similar high temperature. Iron is annealed between 1300°C to 1500°C in one atmosphere of hydrogen. The hydrogen anneal removes interstitial impurities, such as carbon, oxygen and nitrogen.[11] However, in reality I could not achieve such a high temperature and one atmosphere of hydrogen at the same time.

---

[11]same as footnote 2.

28

Supermendur also requires a wet and dry hydrogen treatment to remove interstitial impurities followed by annealing in a magnetic field. To produce a 1/8" rod of the alloy, I used an arc furnace in an argon atmosphere that was slightly (about 10 PSI) lower than one atmosphere. Then, I used a tube furnace to anneal the alloy at 950°C in hydrogen atmosphere. After the anneal, however, its surface turned black. Moreover, it got harder and more brittle than before annealing. Then I tried annealing it in argon. Although argon is inert, the surface of the alloy turned dark. Apparently oxidation was taking place. To avoid it, I inserted the alloy with tantalum foil, which is an oxygen getter, into a quartz tubing. Then the tubing was sealed off using a gas torch after being evacuated. Then the tubing was placed in a long, cylindrical crucible. Then the crucible was put in a 906°C furnace for one hour. Then, the crucible was removed from the furnace and cooled down quickly to room temperature.

The rod's diameter was reduced with a rolling tool. After the diameter got small enough for a wire draw plate, I pulled the alloys through the holes in the plate and gradually made the diameter smaller. One problem was that the alloy got brittle after several rollings or pullings. So I had to repeatedly anneal the alloys during the shaping process. The product was a 0.020" wire that was used to shape the yoke-shaped magnets described next.

Table 2.1.   Magnetic properties of Supermendur and Supermalloy. (Taken from Kirk-Othmer)

Alloy type	Trade name	μ_i	μ_m	H_c (A/cm)	B_s (T)	B_r (T)
2V-49Co	Supermendur	1,000	60,000	0.16	2.40	2.15
5Mo-79Ni	Supermalloy	75,000	800,000	0.004	0.80	0.50

2.3.2. Electromagnet

After I made cores made of iron, nickel, Supermendur and Supermalloy, I wound coils around them and compared emf's from pick-up coils when we applied an ac-current to the driving coils. It turned out that the pure iron core produced the largest emf, thus we decided to use it. One reason why pure iron is better than more modern alloys is that it is very difficult to make the alloys properly. Thus we can expect much worse magnetic properties than the published data.

The ends of the core were polished flat so that the magnetic flux does not expand to much. After the polish, we annealed it because we have found that annealing is extremely important to maintain the magnetic properties of the core. If the iron core is bent, its magnetic properties are significantly altered. Therefore, after folding it into the desired shape, we again annealed the core in an evacuated quartz tube with tantalum at 900°C. It might have been better if we had annealed it at less than 800°C to avoid a phase transition in iron. The iron core had 0.020 inch diameter. The purity of the iron was 99.9%.

30
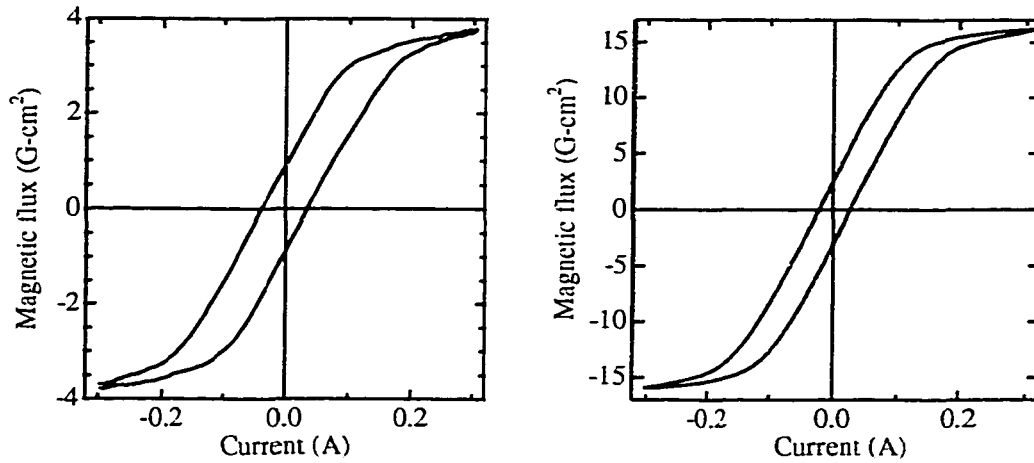
Fig. 2.5.   Magnetic flux generated by the electromagnet. A pick-up coil was placed in the gap (left plot). Flux is 3.0 G-cm^2 at 0.1 A. When a pick-up coil was place on the iron core (right plot), flux was about four times larger.

Coils were wound around the core with care taken not to bend the core. The driving coil was 200 turns of 38 AWG copper wire. Because it was difficult to measure the magnetic flux at dc, we used an ac method. We applied an alternating current of 0.3 A max to the driving coil. Several frequencies were tested: 5, 10, 50 and 100 Hz. The results were the same at any frequency we tested. The pick-up coils were wound tightly around the core so that it would not pick up any stray fields. We placed a six-turn pick-up coil at the gap and a forty-turn pick-up coil on the core. Their emf's were recorded with a digital oscilloscope. We integrated the emf to find out the flux. Figure 2.5 shows the hysteresis loops of the magnet. The magnetic flux values in the figures have been divided by the number of turns. They show that the flux at 0.1 A is 3.0 G-cm^2 in

31

the gap. The coercivity is about 0.03 A. The remanent flux is about 0.9 G-cm^2. The flux in the core is about four times larger than that in the gap. Most of the flux does not go through the gap. But for our best magnet, such a flux implied that about $N = \Phi/\Phi_0 = 3.0$ G-cm$^2/2.07 \times 10^{-7}$ G-cm$^2 = 1.5 \times 10^7$ vortices would be providing the force in our experiment, a sufficient number. And the small magnet diameter (0.020") allowed us to avoid edge pinning effects on the small crystals used (~0.100").

2.4. PIEZOELECTRIC TUBE

2.4.1. Piezoelectric Tube

A piezoelectric tube was used to move the small electromagnet at the resonance frequency of the oscillator. It was manufactured by Staveley Sensors Inc.[12] The type is "EBL #2," which is equivalent to "PZT-5A." The length, outer diameter and the wall thickness are one inch, 0.375 inches and 0.020 inches, respectively. Its polarization is OD positive. Its outer electrode is divided into four quadrants. The inner wall is a single electrode. When equal and opposite voltages were applied to opposite quadrants, the tip of the tube moves

$$\Delta x \ (\text{or } \Delta y) = \frac{0.9 d_{31} V L^2}{d_m t}$$

where L=length, V=voltage, t=wall thickness, $d_m = (OD+ID)/2$. d_{31} is a property of the material and is temperature dependent. At 293 K, $d_{31} = -1.73$ Å/V. At 4.2 K, $d_{31} = -0.31$ Å/V. At 73 K, $d_{31} = -0.75$ Å/V; thus, the piezo tube should move 95 Å/V at the temperature of our experiment. To drive the tube, I used

---

[12]91 Prestige Park Circle, East Hartford, CT 06108. Phone: (860)289-5428.

32

operational amplifiers (op-amps). Since the supply voltages for op-amps are usually ±15 V, the maximum displacement was estimated to be 1425 Å. This limit could be circumvented by using high voltage op-amps or other circuits, but the signal seemed to be large enough with this magnet motion amplitude. Therefore, I decided to use regular op-amps to drive the piezo.

One of the problems of using a piezo tube is that it has its own resonances. It is clearly not good if it coincides with the resonance frequency of the oscillator. So, I measured piezo motion. I tested it as follows. I used one quadrant to drive the tube. Then, I measured the voltage on the opposite quadrant with a lock-in amplifier (Stanford Research SR530). I could do this because a strain in piezo will cause a field in the material and vice versa. I.e., if an electric field is applied to the piezo, then it either expands or contracts. The resonance peaks of the piezo tube mounted in the probe at 77 K are shown in Fig. 2.6. Fortunately, the peaks were very broad compared to those of the oscillators. Thus, within the narrow frequency range, the response of the piezo could safely be assumed constant.
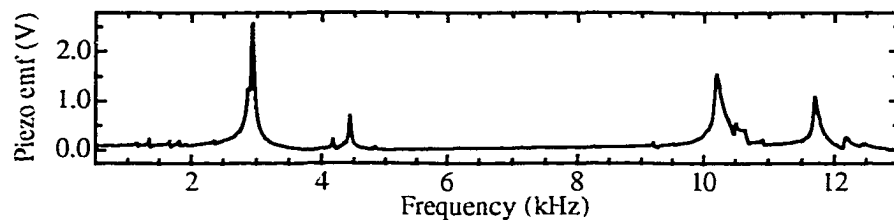
Fig. 2.6.   Voltage measured on the opposite quadrant of the piezo tube at 77 K
            when a quadrant was driven with a 15 V_{pp} sinusoidal signal.

33

2.4.2. Vibration Reduction

One of the major obstacles was oscillator vibration caused by piezo motion. Even when the electromagnet was not on, i.e., when there should be no force exerted on the oscillator, piezo motion mechanically coupled to the oscillator. First I screwed down the piezo tube onto the copper plate on which the oscillator clamp was mounted. When I drove the piezo at the oscillator's resonant frequency I immediately realized that the oscillator was driven at a very large amplitude. So, I tried several materials to isolate the piezo tube. First, I tried vibration-damping material. It was a blue rubber-like material. The material worked wonderfully at room temperature. However when I tested at liquid nitrogen temperature, large coupling came back. I concluded that the damping material got hard at liquid-nitrogen temperature; thus my attention was given to finding something soft at even low temperature. But the material had to be reasonably firm also so that I could position the magnet with respect to a YBCO crystal that was glued on to the oscillator head. Being unable to find such material, I tried ball bearings. I glued four ball bearings sandwiched between the copper base and the Macor base of the piezo tube. The idea was that reducing the area in contact might help isolating the oscillator from the piezo. It turned out, however, to be a failed attempt. Ball bearings did not reduce coupling at all. Next I tried soft springs. First I glued them with superglue, but after a couple of thermal cycles superglue often failed. Thus, I instead used Stycast 2850FT to attach springs under the piezo tube. This was fairly successful, but it was not enough. Thus, next I tried to mount the piezo on a separate copper base. At the

34

same time, the oscillator was mounted on some springs for further vibration-coupling reduction. To connect the two bases, I used three threaded brass rods. One end of the rods was screwed into the probe flange. The order of the plates turned out to be important. When the copper plate with the piezo tube on it was placed closer to the probe, coupling was larger than the case where the plate with the oscillator was placed closer to the probe (Fig. 2.7). This latter arrangement was adopted.
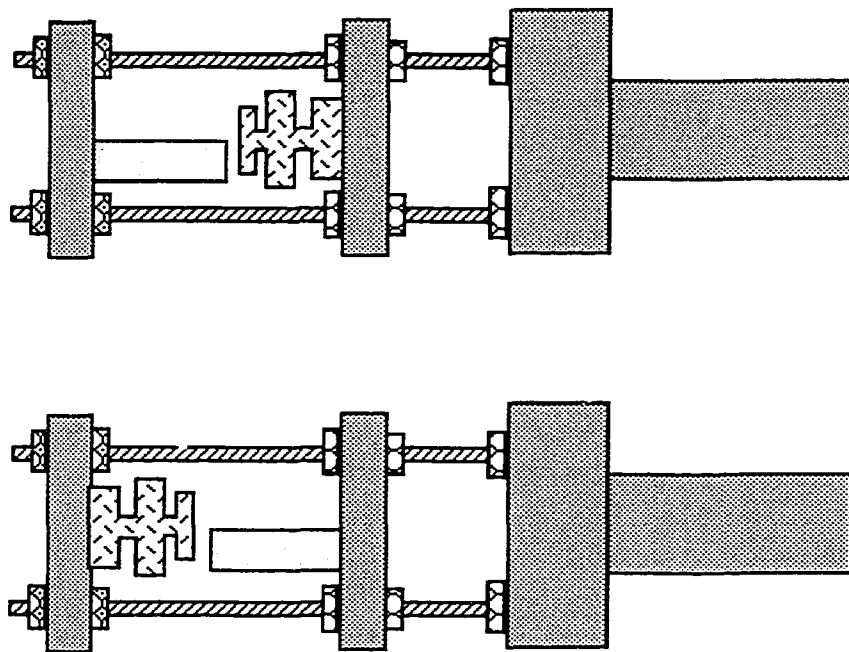
Fig. 2.7.   Schematic of the bottom of the "Magnus force probe." Top figure is the successful configuration, where the piezo is mounted on the end of the probe. In the bottom configuration, the positions of the piezo and the oscillator was switched. This configuration caused a larger mechanical coupling between the piezo and the oscillator.

35

After this modification, the mechanical coupling diminished. However as I describe elsewhere in this dissertation, springs under the piezo tube caused undesirable side effects. First, the oscillation amplitude got very small. Second, the direction of the piezo motion was not what it should have been. For example, when only one pair of two opposing quadrants was driven, the piezo moved normal to the quadrants. For these reasons, we decided to clamp the piezo tube down to the base so that we could estimate the motion of the oscillator better. This caused a larger mechanical coupling between the piezo and the oscillator, but it was a manageable size.

2.4.3. Piezo Tube Motion

The piezo tube that moved the magnet did not seem to be moving as it should have been. I noticed the problem when I was measuring oscillator motion when I moved the piezo parallel and perpendicular to the oscillator. As I derive in the appendix, the amplitude of the oscillator motion is

$$\varphi_0 = \frac{ld_0 k_p / I}{(\omega_0^2 - \omega^2) - i\omega\eta / I}$$

for magnet motion perpendicular to the oscillator. Here, d_0 is the amplitude of magnet motion, k is the spring constant for pinning, I is the moment of inertia of a simple torsional oscillator, η is the dissipation, ω is the applied frequency while ω_0 is the resonance frequency of the oscillator. The important conclusion is that the oscillator motion amplitude is proportional to the distance between a pinned flux and the axis of the oscillator, which is denoted by l. For magnet motion parallel to the oscillator, the amplitude is

36

$$\varphi_0 = \frac{-hd_0k_p/I}{(\omega_0^2 - \omega^2) - i\omega\eta/I} \, .$$

Here, the oscillation amplitude is proportional to h, which is the misalignment (distance) between the oscillator plane and the magnet. Thus, this simple calculation is telling us that we should always get larger signals when the magnet moves perpendicular to the oscillator since l » h; l was about 5 mm while h was at most 0.1 mm. However, I had done many measurements that had larger signals when moved in the parallel direction than in the perpendicular direction. In fact, I sometimes didn't see any signal in the perpendicular direction while I saw a clear signal in the parallel direction.

Recently, we made a nice probe with an interferometer to investigate small motions of oscillators. I borrowed the probe to measure the motion of the piezo tube in real time. Detailed discussions of interferometry and the probe can be found in Graf's thesis.[13] I briefly explain the basics of interferometry followed by the results of the measurements.

A laser emits light through the cleaved end of an optical fiber. The light can be reflected off a flat surface near the fiber end. The reflected light will go back into the fiber. Light reflected at the cleaved end and that reflected at the surface of a nearby object, which in my case was a piezo tube, will interfere. Depending on the phase difference between the two paths, interference might be constructive, destructive, or somewhere between the two. Between neighboring destructive and constructive fringes represent the optical path difference of $\lambda/2$. But because the light has to travel a round-trip outside the fiber, the motion of the

---

[13]Tobias Graf, Thesis, 1998.

37

piezo is actually λ/4 between adjacent maximum and minimum of fringes. The wavelength of the laser was 675 nm, hence change from a minimum to its adjacent maximum in the interference fringes corresponds piezo motion of 169 nm.
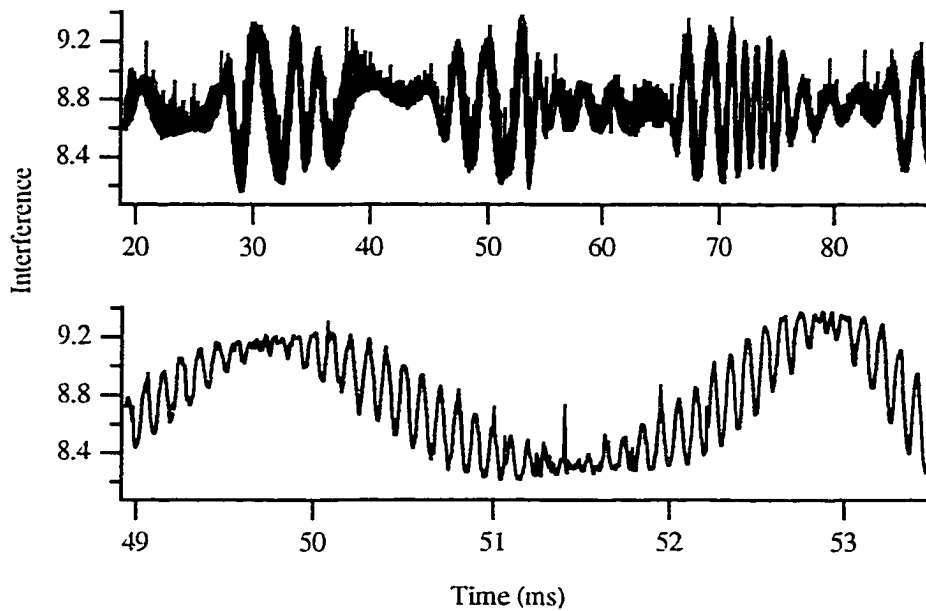
Fig. 2.8.   Interference fringes when the piezo tube was driven using two
             quadrants of the piezo tube that were facing each other in parallel to
             the oscillator plane. Laser was reflected off the piezo tube parallel to
             the oscillator. The top plot shows a slow oscillation due to vibration
             from outside the system. The bottom plot shows peaks in resonance
             fringes caused by the piezo driven at 10 kHz.

The top plot of Fig. 2.8 shows the interference amplitude when the piezo was driven "parallel" (i.e., two quadrants were driven such that the piezo tube should move parallel to the interferometer fiber axis). However, there is no

38

guarantee that the tube actually moves as desired. The lines in the plot seem broad because of the piezo motion, which was 10 kHz. To see that fast signal, the bottom plot of the same figure is a blow-up of a small region of the top one. As you can see in the figure, the interferometer could measure the position of the piezo in real time. The 10 kHz signal seems to have about half of the interference fringe size, so the estimated amplitude of the piezo was about 80 nm.
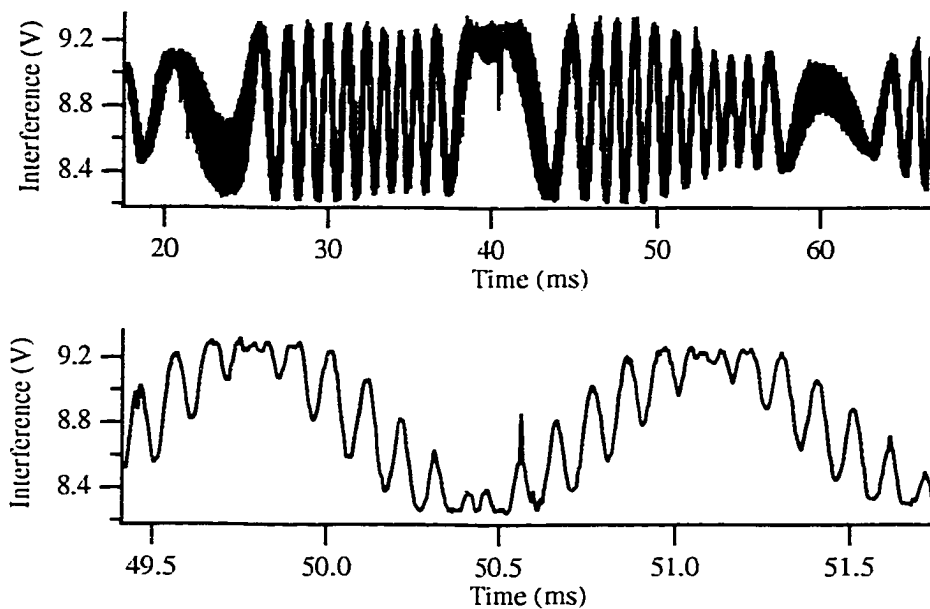
Fig. 2.9.   Interferometry data. Laser was reflected off the piezo tube parallel to the oscillator plane. The piezo tube was driven perpendicular to the oscillator. The second plot from the top is a blow-up of a section of the top plot. It shows 10 kHz oscillation. There should be no detectable motion if the piezo were moving as it was supposed to be.

39

When the piezo was driven in the perpendicular direction, it actually moved in the parallel direction, too. Also, you might notice a slow yet large oscillation in these interference fringes.

The large, periodic motion was not excited by piezo driving. Rather, it came from the environment. The figure below shows the same motion when the piezo was not driven. This time, the oscillation crossed about 30 fringe peaks. It is an amplitude of about 5 μm. The frequency of the oscillation was about 25 Hz.
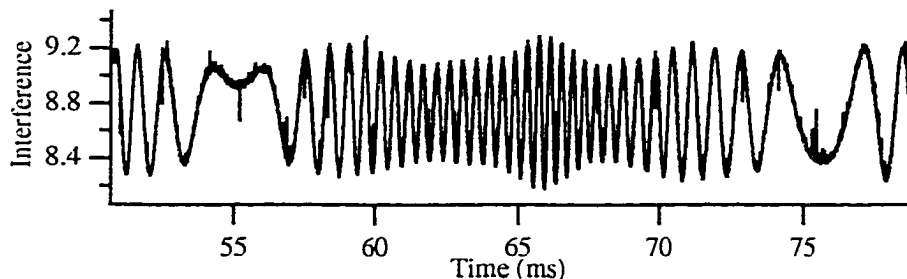
Fig. 2.10.   Interferometry data when the piezo was not driven. A large, slow oscillation of the piezo is still visible. Thus, this shows that the vibration comes from an external source.

Thus, interferometry proved to be a very useful tool to measure small motions in real time. The slow period of Fig. 2.10 suggested that the reason that the piezo tube was not moving as it was supposed to might be related to the springs used for vibration isolation. The piezo tube was wobbling around because of the springs underneath.

40

Therefore, for the following experiments I screwed down the piezo tube to the copper base inside the probe. Although this increased the vibrational coupling of the piezo to the oscillator, it provided for reliable piezo motion.

2.5. FORCE CALIBRATION

Next, we performed force calibration. The measurements were done at liquid-nitrogen temperature. First, I had to cancel the oscillator motion due to the mechanical coupling between the oscillator and the piezo. Because the piezo tube was screwed down, I had to apply a relatively large driving voltage to the oscillator to cancel that vibrational pickup signal. For example, when I applied 15 V_{pp}, 180° out-of-phase signals to two opposite quadrants of the outer electrodes of the piezo tube such that it would move parallel to the oscillator plane, I had to apply 2.4 V_{pp} capacitive driving signal to the oscillator driving electrode. Nevertheless, I managed to cancel the oscillator motion due to mechanical coupling. The flat lines in Fig. 2.11 were taken without a magnetic field. Thus, cancellation proved to be very good as can be seen from the flatness of the lines. Between the without-field measurements, I turned on the electromagnet and measured the capacitive pick-up signal. The dots in the figure were experimental data points. These peaks were fit to theoretical curves, which are solid lines. However, the fit was so good that the experimental data points almost perfectly lie on the theoretical lines. Thus, they don't show well in the plots. The theoretical fit was done as follows. The amplitude of oscillation of a forced harmonic oscillator is

41

$$x_0 = \frac{F_0}{2m\omega} \frac{1}{(\omega_0-\omega) - i\,\gamma/(2m)}.$$

Thus, considering the phase difference between the driving signal and the detected signal, the outputs from the lock-in amplifier could be expressed as

$$V_{ch1} = Re(x_0)\cos\theta - Im(x_0)\sin\theta$$

$$V_{ch2} = Re(x_0)\sin\theta - Im(x_0)\cos\theta$$

where

$$Re(x0) = \frac{F_0}{2m\omega} \frac{\omega_0-\omega}{(\omega_0-\omega)^2 + (\frac{\gamma}{2m})^2} \text{ and}$$

$$Im(x0) = \frac{F_0}{2m\omega} \frac{\frac{\gamma}{2m}}{(\omega_0-\omega)^2 + (\frac{\gamma}{2m})^2}.$$

The actual data had some offset, so I had to add a constant to fit the curve. To calibrate the data, we need to convert measured voltage to an actual force. To do this, I used capacitive excitation data. The oscillator was driven capacitively with a 1 V_{pp} signal. The bias voltage was 200 V. The curve fit to the same formula as mentioned above gave a value $F_0/2m = 0.001709$ Vs^{-2}. On the other hand, the exerted force can be estimated from the driving signal. The force due to capacitive excitation is

$$F = \frac{C_0 V_0 V_1}{x_0}$$

where C_0 is the gap capacitance, V_0 is the bias voltage, V_1 is the driving voltage and x_0 is the gap. Their values were 7.0×10^{-13} F, 200 V, 1.0 V and 0.5 mm, respectively. Hence, the driving force was estimated to be 3×10^{-7} N. However, one must notice that a much smaller force is required to excite the same amplitude

42

of oscillation if a force were applied on the head. Since force exerted on the head is $I_2/I_1 \approx 30$ times more effective than that exerted on the wing, a pinning force that causes the same amplitude of oscillation is about 1×10^{-8} N. The driving voltage was varied from 2.5 V_{pp} to 15 V_{pp}. Although the applied voltage was much lower than the maximum voltage for the piezo tube (300 V), the response was not linear. It is difficult to believe that the piezo was already in its non-linear regime. It might be the case that the size of the crystal had something to do with the non-linear behavior. The crystal used in the calibration experiment was small, almost the same size as the magnet core, which had a diameter of about 0.5 mm. So, flux did not necessarily penetrate only through the superconductor at large amplitudes. However, the parallel data indicate that the measured force is linear up to about $1-2\times10^{-8}$ N in this test experiment. Thus, a reliable check of the pinning force could be made even in this non-ideal geometry. These results are presented in later chapters.

43
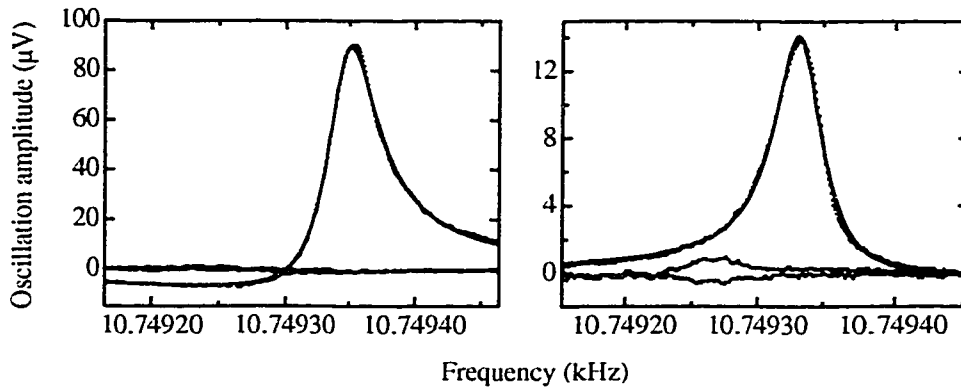
Fig. 2.11.   Oscillator motion caused by the pinning force. The left plot was of "perpendicular" drive. Two opposing quadrants were driven with 10 V_{pp} sinusoidal signal. The right plot was of "parallel" drive. The driving signal was 15 V_{pp}. The two relatively flat lines in each plot were the picked-up signal without magnetic field. I measured before and after with-magnetic field measurements. One line with a large peak in each plot was the picked-up signal with magnetic field. The experimental data were dotted lines, but the curve fits (solid lines) were so good that they coincide.
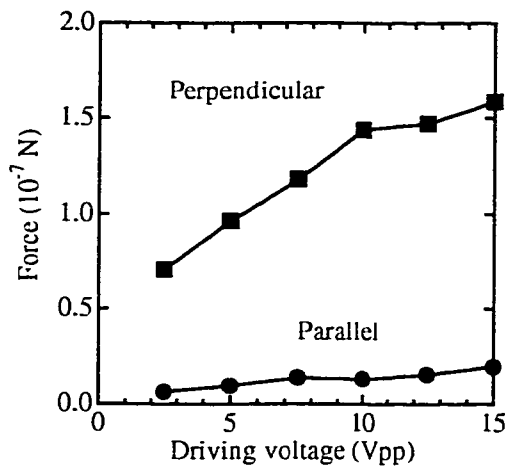
Fig. 2.12.   Pinning force as a function of piezo driving voltage. The force was calculated using the curve fit. Squares are of perpendicular drive while circles are of parallel drive.

44

Chapter 3: Growth and Characterization of Superconducting Crystals

3.1. GROWTH AND CHARACTERIZATION OF $YBa_2Cu_3O_{7-\delta}$ CRYSTALS

3.1.1. Crystal Growth

The YBCO crystals were grown using the self-flux method. The starting materials were 99.999% pure Y_2O_3, 99.997% pure $BaCO_3$ and 99.99% pure CuO. When making a polycrystal, we dry the starting materials first. The materials were weighed straight out of jars, because as long as the mixing ratio is consistent, the result should be the same. To be safe, occasionally the starting materials were dried in ovens. 12-hr drying didn't cause even half a per cent change in weight. Thus, I concluded that the materials were dry enough in their jars. The ratio of Y:Ba:Cu in the melt was 1:4:10 in moles, respectively. Alex Barr, who is a former student, used to use 1-6-30 ratio, but I found that 1-4-10 ratio yielded more and larger crystals. In one batch, I mixed 0.3990 g of Y_2O_3, 2.7895 g of $BaCO_3$, and 2.8111 g of CuO. The last decimal is not so important; I didn't spend so much time to get it right. After mixing them in a mortar for twenty minutes, I placed the crucible in a 906°C oven. After repeating this process two more times, I put powders in two crucibles and packed them well by tapping the crucibles against a table. Then I placed them in a 906°C oven. Then, one of the pellets was placed on an yttria-stabilized zirconia (YSZ) tray in an oven for crystal growth. The profile was the following: ramp up to 900°C in 10 hrs and stay there for 1 hr. Then ramp up to 1000 °C in 4 hrs and stay there for 3 min.

45

Then ramp down to 900°C in 23 hrs and stay there for 1 hr. Then ramp down to 500°C in 13 hrs and stay there for 1 hr. Then the oven was turned off. YSZ is said to be vulnerable to thermal shock, so I waited for the temperature to come down to about 60°C to remove the tray from the oven.
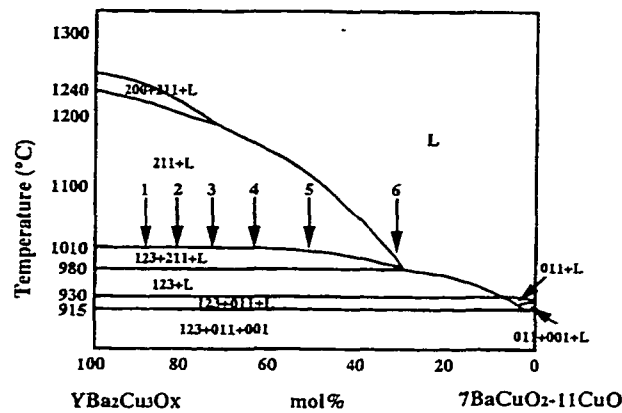
Fig. 3.1.   A pseudo-binary phase diagram along the join $YBa_2Cu_3O_x$ to $7BaCuO_2\cdot11CuO$. The phases are labeled as follows: 123, $YBa_2Cu_3O_x$; 011, $BaCuO_2$; 001, CuO: 211, Y_2BaCuO_5; 200, Y_2O_3. (From H. Asaoka et al.[1])

Crystals usually grew along the edges of the tray crucible. Unfortunately, edges of crystals were attached to flux; they were inevitably broken into smaller pieces when removed from flux. But once in a while I managed to harvest large crystals, which were up to a few millimeters in a and b directions while the c axis was much thinner. It is difficult to measure the thickness directly. Instead, I estimated the thickness from the surface area of a crystal and its mass. The

---

[1]H. Asaoka et al., Jpn. J. Appl. Phys. 32, 1091 (1993).

46

theoretical x-ray density of YBCO is 6.3 g/cm^3, but the experimental value is 6.0 g/cm^3. Thus, I used the latter to calculate the thickness of crystals. The c-axis thickness was estimated to be about 30 μm, but variation was pretty wide. Due to slow cooling in the oven, our as-grown YBCO crystals were already twinned.
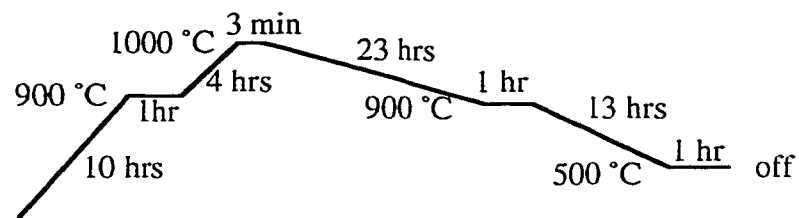
Fig. 3.2.   Furnace profile for YBCO single crystal growth
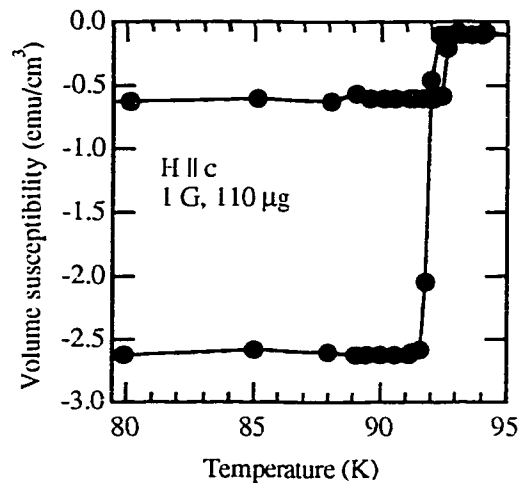
Fig. 3.3.   Field-cooling, zero-field-cooling measurement of an YBCO single crystal after oxygen anneal. Applied field was 1 Oe in the c-axis direction.

47

As-grown crystals were not optimally superconducting due to oxygen deficiency. However, because they were cooled relatively slowly below the tetrahedral-orthorhombic transition temperature (about 650°C), crystals had twin boundaries. To oxygenate them, I placed them in a tube oven on gold foils in an alumina boat. Under steady flow of oxygen the crystals were annealed at 375°C (display temperature) for six weeks then slowly (0.02°C/min) cooled down to room temperature. The oxygenated YBCO crystals were characterized with a SQUID magnetometer and were found to have $T_c = 92$ K. The transition width was less than 1/2 K.

I have tried shorter annealing times. For example, I kept YBCO crystals at 400°C for a week followed by 0.1°C/min cooling to the room temperature. But this one-week annealing in O_2 at 400°C proved to be not enough; the superconducting transition width was more than 1 K. This might show that it takes more than a week for oxygen to diffuse uniformly in the crystal. After an additional one-week annealing, the identical crystal showed a sharp enough transition (i.e., the transition width was less than 1/2 K).

3.1.2. Post Annealing

One problem I faced was that YBCO crystals we have grown had too many defects for flux lines to move at a reasonably low temperature where the order parameter is still large enough for experiments. So, I tried to anneal the crystals under no stress to get rid of defects. As Ginsberg et al. noted, YBCO single crystals may be under stress during growth because they are attached to

48

flux from which the 123 crystals are grown. In fact, the change in twin boundary directions might be due to the stress the crystals are under when they are grown.

The first attempts of post-annealing were done as follows. After YBCO single crystals were separated and O_2 annealed as described above, I placed the single crystals on a platinum sheet, which was placed on an alumina tray. Then the tray was placed in a box furnace in air and heated up to a temperature ranging from 750 to 950°C in air. It was expected to be easier to remove defects at higher temperature, but I didn't want to melt the crystals. After the sample was kept at the high temperature for one to ten hours, the temperature was gradually lowered to 800°C to avoid quenching atoms at nonequilibrium positions. The heater was turned off while the sample was kept in the oven until the temperature reached room temperature. For the sample that was heated to less than 800°C, the oven was turned off immediately after the soak time. After the anneal, twin boundaries disappeared except for the one that was heated up only to 750°C. However, the surfaces of the crystals were not as shiny as before. The reason for this might be that flux which had been on the crystals melted.[2]

Then, the crystals were oxygenated in the tube oven. They were kept at 400°C (display temperature; the actual temperature might have been higher) for one week followed by a slow cool (0.02°C/min.) down to 200°C. Below that temperature, the cooling rate was increased initially to 0.04°C/min. and finally 0.1°C/min.

Next, I tried the high-temperature anneal for the YBCO crystals in an O_2 flow using a tube oven instead of air, above. This way, the crystals will not lose

---

[2]For details, please see Koki's lab book 8:73–77.

49

oxygen; thus I could expedite the annealing procedure by eliminating the low-temperature O_2 annealing. This was the reasoning, in any case. Four large fully oxygenated crystals were placed on a platinum sheet. The sheet was placed in an alumina boat and inserted into a tube furnace. The furnace was kept at 770°C for two days under oxygen flow. Then the temperature was lowered to 400°C rather quickly. The reason for the rapid cooling was to avoid twin-boundary formation by quickly getting into the orthorhombic phase from the tetragonal phase. Below 400°C the furnace temperature was lowered at a rate of 0.5°C/min to absorb oxygen.
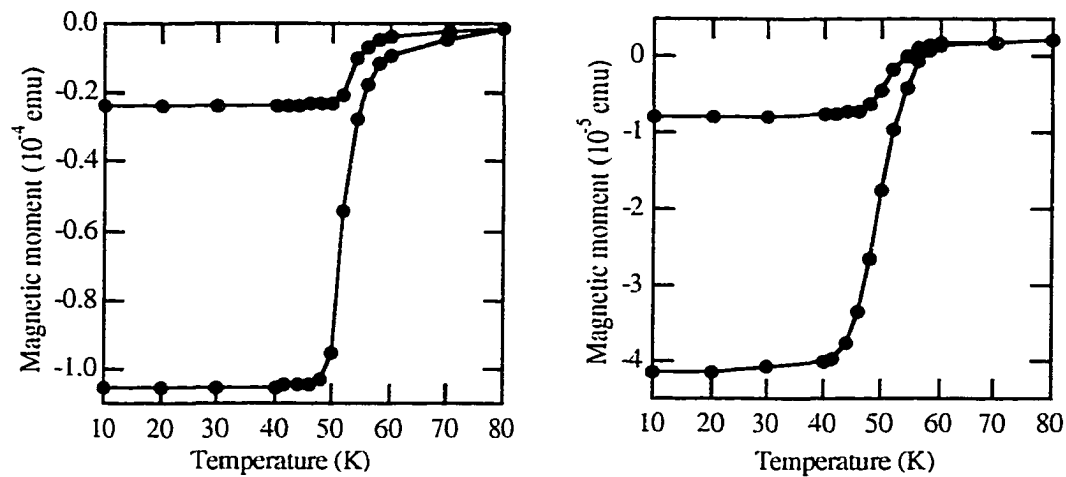
Fig. 3.4.   Magnetic moments of YBCO crystals after high-temperature anneal but before a long oxygen anneal at a lower temperature. T_c decreased as oxygen escaped from the crystals. Superconducting transition seems sharper than low oxygen pressure anneal at a lower temperature.

50

The result of this high-temperature annealing in O_2 flow was not what I had expected, but interesting (Fig. 3.4.). After this annealing procedure, the T_c dropped to about 60 K. This superconducting transition temperature corresponds to oxygen content of x = 6.6 in $YBa_2Cu_3O_x$ (Fig. 3.5). The transition itself was rather sharp. It had been difficult for us to make superconducting YBCO crystals with $T_c \approx 50$ K and having sharp transition at the same time. Crystals with varying T_c's are desirable for various systematic studies. So, this might be a good way to make such crystals. However, for the purpose of my experiment, I needed a high T_c. So, I put the crystals back to the tube furnace and further annealed into oxygen flow at 400°C for 4 weeks.
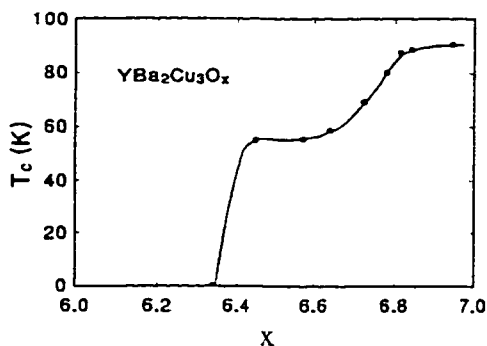
Fig. 3.5.   Dependence of T_c on oxygen content x in $YBa_2Cu_3O_x$. (from Schilling and Klotz[3])

3.1.3. Detwinning

The most popular and successful way to detwin YBCO crystals is the thermomechanical method.[4,5] Usually, crystals are uniaxially compressed either in the a- or b-axis direction. The pressure is typically from 5×10^7 to 1×10^8

[3]J.S. Schilling and S. Klotz, in Physical Properties of High Temperature Superconductors III, D.M. Ginsberg ed. World Scientific, Singapore, 1992, p.92.
[4]H. Asaoka et al., Phsica C 268, 14 (1996).
[5]J. Giapintzakis et al., J. Low. Temp. Phys. 77, 155 (1989).

51

N/m^2.[6] The temperature is typically 300 to 450°C and sometimes as high as 600°C. Usually, the detwinning process is performed in oxygen to keep the oxygen content as high as possible. Our detwinning apparatus uses a spring at room temperature to provide the force, applied via a quartz rod to the crystal, mounted between quartz or stainless-steel plates. Typically, forces of ~1 N were applied to crystals with cross-sectional area ~10^{-2} mm^2.

The detwinning procedure was successful. Though we could not accurately determine the value of the pressure applied to the superconductor, twin boundaries disappeared within an hour when the temperature was raised to 450°C. Detwinning did not occur in some samples no matter how I changed the conditions of detwinning. Another problem of the method was that, while it worked fine with smaller, rectangular samples, it was not easy to detwin larger crystals because they often popped off or were crushed. Further improvement of the detwinning tool is needed to detwin crystals more effectively.

3.1.4. BaZrO3 Crucibles

We have been growing YBCO crystals in yttria-stabilized zirconia (YSZ) crucibles. For almost everything other than crystal growth, we use alumina crucibles. However, they cannot be used for YBCO crystal growth because Al^{3+} gets into the YBCO lattice and thus degrades the properties of the crystals, such as T_c. In contrast, Zr^{4+} in YSZ crucibles has little solubility in both the Y_2O_3-BaO-CuO melt and the YBCO lattice. In fact, by using YSZ crucibles, we have

---

[6]V.I. Voronkova and Th. Wolf, Physica C **218**, 175 (1993).

52

consistently grown YBCO crystals with $T_c = 92$ K and the transition width of less than 1/2 K. Moreover, they are commercially available.[7] YBCO crystal growth in YSZ crucibles has been considered the state-of-the-art until this year. However, YSZ crucibles are not perfect. First, they are not completely inert from the melt. It is evident that the Y_2O_3-BaO-CuO flux attacks the crucibles by the fact that the crucibles always have circular depression at their centers after repeated crystal growth, the size of which matches that of the pellets from which we grow crystals. After a while, the crucibles get weak that they break easily by a small shock. The chemical reaction of this corrosion is $BaO + ZrO_2 = BaZrO_3$. The product of the reaction is an insoluble solid. Second, commercial YSZ crucibles are only 99% pure. These imperfections had never caused any real problem until the transverse force experiment. I needed high quality, impurity-free YBCO crystals to observe the transverse force. The crystals grown in YSZ crucibles seemed to have too many pinning centers to observe the force. Thus, I had to try different crucibles to grow as pure crystals as possible.

$BaZrO_3$ crucibles seem to be a better material to grow YBCO crystals.[8] However, it is very difficult to make such crucibles. Thus, some groups attempted to cover ready-made crucibles with a layer of $BaZrO_3$.

N. Alford *et al.* showed the feasibility of coating YSZ with a layer of $BaZrO_3$.[9] They first made YSZ discs. Then they prepared thick films of $BaCO_3$ by mixing a thick-film vehicle with $BaCO_3$ powder. This thick ink was spread on

---

[7]We buy them from Vesuvius McDanel Co., (724)843-8300. Part # ZCT4828. 5 ml,
40×30×6 mm rectangular tray crucible.
[8]Ruixing Liang, D.A. Bonn, and W.N. Hardy, Physica C **304**, 105 (1998).
[9]N. Alford, A. Templeton and S. Penn, Supercond. Sci. Technol. 11, 703 (1998).

53

the YSZ discs and sintered at about 1500°C. They showed that $BaZrO_3$ was formed by x-ray diffractometry. They didn't seem to try growing crystals using the crucibles.

Another group successfully coated alumina crucibles with $BaZrO_3$.[10] They used synthetic barium zirconium isopropoxide $(BaZr(OC_3H_7)_6)$ mixed with water to make paste. They have found that $BaZrO_3$ does not stick to YSZ crucibles well. This is why they used alumina crucibles. After painting a thin layer of the paste on the crucibles, they sintered them. The EDX measurement did not find any alumina contamination in the $YBa_2Cu_3O_{7-\delta}$ crystals grown in the $BaZrO_3$-coated crucibles. The crystals, however, did not have a high T_c or a sharp transition.

R. Liang et al. has successfully fabricated $BaZrO_3$ crucibles.[11] They first tried coating YSZ crucibles with a 1 μm-thick $BaZrO_3$ film. But the impurity level in the YBCO crystals was reduced by only a factor of two. Therefore, they decided to fabricate $BaZrO_3$ crucibles. They have found that secondary phase in $BaZrO_3$, such as BaO, ZrO_2 and glass phases, causes percolation of the Y_2O_3-BaO-CuO melt. Thus, the starting materials, $BaCO_3$ and ZrO_2, had to be mixed in a precisely one-to-one ratio. Furthermore, particle size had to be very small for the sintered crucibles to be melt-tight. They used a ball mill to make the particle size less than 0.5 μm. YBCO crystals grown in their $BaZrO_3$ crucibles were spectacular; the x-ray rocking curve measurement width 0.007° showed that their YBCO crystals were even more perfect than 99.999% pure $SrTiO_3$ crystals grown

---

[10]Jing Shi, J. E. Berer and X. S. Ling, to be published.
[11]Ruixing Liang, D.A. Bonn, and W.N. Hardy, Physica C 304, 105 (1998).

54

by the Czochralski method, which has rocking curve width 0.013°. The maximum T_c was 93.7 K and $\Delta Tc = 0.2$ K. In their laboratory they grow YBCO crystals of $T_c = 93.7$ K when oxygen content is 6.92 per formula unit. The most interesting property of their YBCO crystals grown in a $BaZrO_3$ is their low-temperature irreversibility line. They claimed that the irreversibility line lies about 20 K below that of the best crystal grown in a YSZ crucible. Such low flux pinning at high temperatures would be desirable for our experiments.
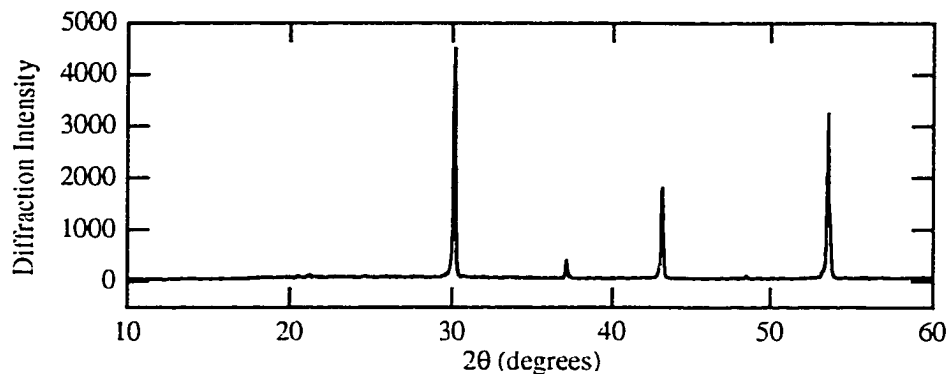
Fig. 3.6.   X-ray diffraction of $BaZrO_3$ polycrystal as a function of 2θ.

I tried to make $BaZrO_3$ crucibles for myself. First, I mixed dry $BaCO_3$ and ZrO_2 in precisely a one-to-one ratio. Then, after sintering three times at 1300°C and regrinding in a mortar with a pestle, I took x-ray diffraction measurements. It showed the powder had become $BaZrO_3$ completely (Fig. 3.6). I pressed the powder using a press mold into a tray shape. However, even after high-pressure press, the $BaZrO_3$ was still crumbly. Thus, I mixed in small amount of starch solution to keep the powder together. After being kept at 400°C for a few hours to get rid of organic materials, the crucible was sintered at 1700°C

55

for 36 hours. Although it got harder, it broke into two pieces. The reason seemed to be too-large particle sizes. Hence, ball-milling seems to be necessary to make $BaZrO_3$ crucibles successfully. This is an on-going project in our laboratory.

3.1.5. SQUID Measurements

The theory of SQUID's can be found in numerous references. For example, Tinkham's book[12] has a section on SQUID's. For a simple yet useful introduction to magnetic measurements, read the booklet published by Quantum Design.[13] Here I'll limit myself to explain what to expect when we do magnetic moment measurements on YBCO single crystals. Ideally the volume magnetic susceptibility (i.e., magnetic moment per unit field per unit volume) is $\frac{M}{H} = -\frac{1}{4\pi}$ because in the Meissner state

$$B = H + 4\pi M = 0.$$

When an external magnetic field is applied parallel to the copper-oxide plane (ab plane), the demagnetizing factor is almost zero because the crystals are thin in the c-axis directions, so the measured value was fairly close to the ideal one.

Figure 3.7 shows the volume magnetic susceptibility vs. temperature. The applied field was 10 G. The mass of the sample YBCO single crystal was 110 μg. Using the density of YBCO (6.0 g/cm^3)[14], I got $|M/H| = 0.095$ emu/cm^3, which is fairly close to $1/4\pi$ ($= 0.08$). The difference is accounted for by the fact that the

---

[12]Michael Tinkham, Introduction to Superconductivity, 2nd Ed., McGraw-Hill, New York, 1996.
[13]Mike McElfresh, Fundamentals of Magnetism and Magnetic Measurements, Quantum Design, 1994.
[14]This is a measured value. The theoretical value is 6.3 g/cm^3.

56

ab plane of the crystal was not exactly vertical, but was tilted with respect to the applied field.
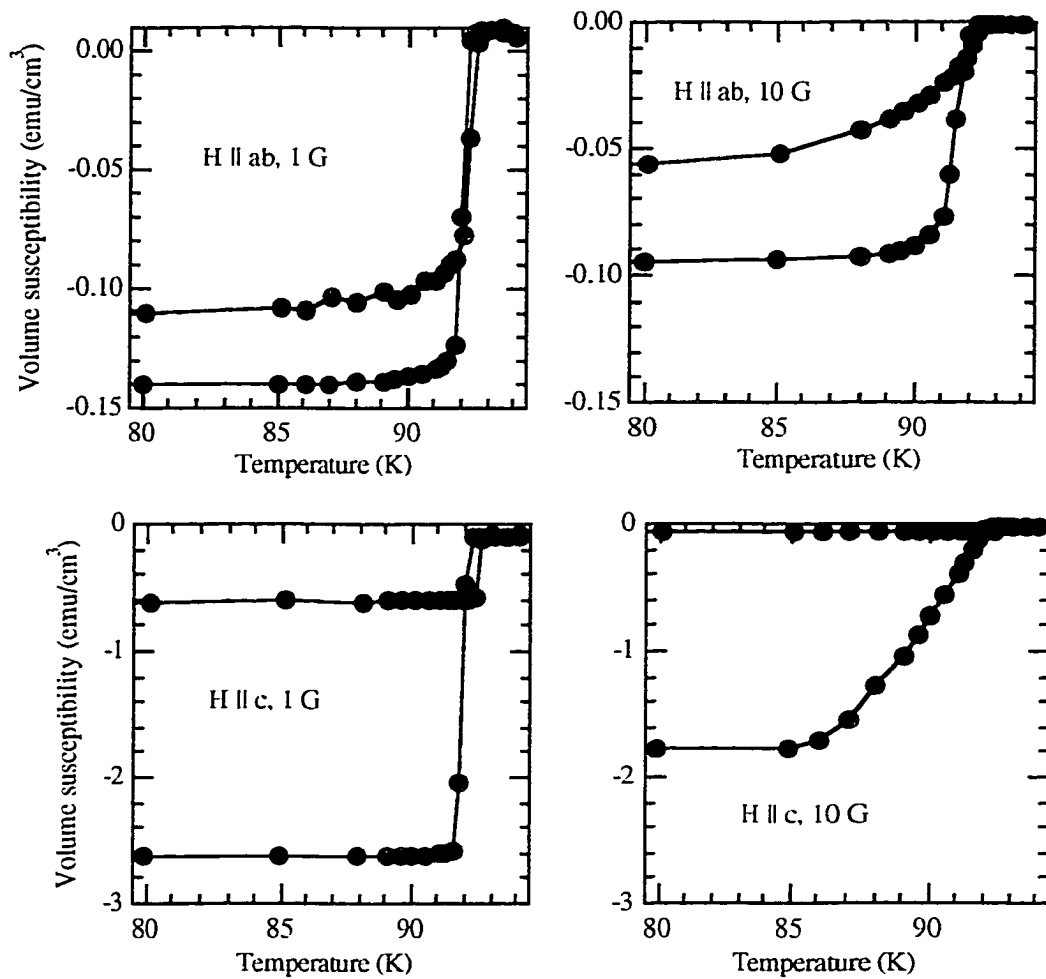
Fig. 3.7.   Volume Susceptibility of YBCO. Data on the top were taken with an applied field parallel to the copper-oxide planes. The data on the bottom were with an applied field parallel to c-axis of YBCO crystals. In each direction, I applied either 1 Oe or 10 Oe.

57

The same YBCO crystal was also measured in the direction where the applied field was parallel to the c axis (Fig. 3.7). In this configuration, due to a large demagnetizing factor (a and b axes were up to a few millimeters while c axis was about 20 micrometers), the measured volume susceptibility was about twenty times larger than the H ∥ ab cases. The figure shows that the onset of superconductivity was 92 K and the transition width was less than a 1/2 K.

Although 1 Oe applied field gives a very sharp transition (because the superconductor is in the Meissner phase), I am more interested in how the YBCO crystals behave when I apply a much higher field. In my transverse experiment, I applied about 0.15 T. So, to find out the irreversibility of the crystals in a realistic setting, I applied 7000 Oe parallel to the c axis. But one point I emphasize is the importance of the field charging mode. If the oscillation mode is chosen, the magnetic field goes over and under the target field until it finally settles to the target field. Since the field is so high that the fluxes penetrate into the superconductor, this oscillating field amplitude makes a complicated magnetic inductance pattern inside the superconductor. This can be understood by the Bean critical-state model and is due to hysteresis in the superconducting state.[15] On the other hand, if the no-overshoot mode is chosen, the magnetic inductance inside the superconductor monotonically decreases without complication. Figure 3.8 is a comparison of the two modes. The data were taken using the same sample. 7000 Oe was applied parallel to the c axis after the sample was cooled down to the lowest temperature in zero field. After the magnetic field was turned on at the

---

[15]M. Tinkham, Introduction to Superconductivity, 2nd Ed., McGraw-Hill, New York, p. 176–179, 1996.

58

lowest temperature, magnetic moments were measured on raising the temperature.
This is called "zero-field cooling (ZFC)." Once the temperature reaches the
highest temperature, it is lowered under the presence of the same magnetic field as
used to measure the magnetic moment. This is called "field-cooling (FC)." The
plot on the left is of the oscillation mode while the one on the right is of the no-
overshoot mode. Thus, to take magnetic moment vs. temperature data in the
mixed phase, it is important to use the no-overshoot mode. From the data on the
right-hand side of Fig. 3.8, it can be seen that the irreversibility temperature (the
temperature where the flux moves freely, so the magnetization is independent of
history) is approximately 86 K for this crystal.
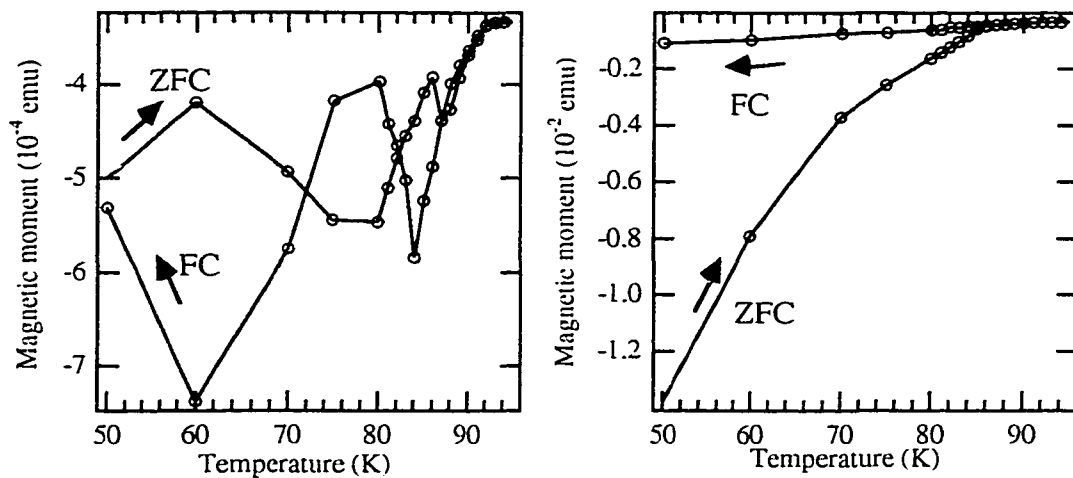
Fig. 3.8.   Magnetic moment measurements of an identical YBCO crystal with
7000 Oe applied field. The data on the left was taken when the field
was charged using 'oscillate' mode while the right data was taken in
'no-overshoot' mode. First, zero-field cooling (ZFC) data was taken
followed by field cooling (FC) data.

59
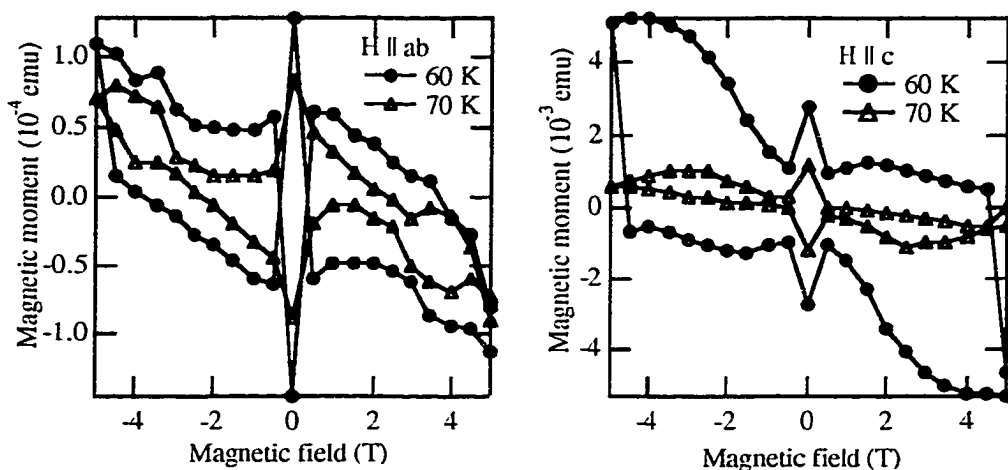
Fig. 3.9. Magnetic moment as a function of applied field. The sample was a YBCO single crystal. The irreversibility line is where hysteresis begins. Both plots were on the same crystal with different applied field directions.

Another way to characterize the YBCO single crystals is to measure the magnetic moment vs. magnetic field. When the temperature is low, the fluxes in the superconductor are trapped; thus the M vs. H plot will show hysteresis. This can be explained quite easily by Bean's model. Figure 3.9 shows the MH hysteresis curves taken with the same sample used to measure temperature sweep. The mass was 110 μg. At 60 K, the flux is pinned, so the hysteresis was large compared to the plot taken at 70 K. The peak near zero field is due to the Meissner phase. The plots are tilted because the epoxy sample holder was diamagnetic. By using such data as shown in Figs. 3.8 and 3.9, crystals could be chosen that permitted reversible flux motion over as wide a temperature and field range as possible, as is desirable for the flux motion experiments.

60

3.2. CHARACTERIZATION OF $Bi_2Sr_2CaCu_2O_{8+\delta}$ CRYSTALS

Although each of the $YBa_2Cu_3O_{7-\delta}$ singles crystal that we grew and used for the experiment had a very sharp transition and a high T_c, they still seemed to pin vortices even at temperatures close to T_c. One problem of the YBCO crystals was that they had twin boundaries, which would cause strong pinning of vortices. Thus, we tried to detwin some crystals. The details of the process were described in the previous chapter. Although we managed to detwin smaller, rectangular crystals, it was difficult to detwin large crystals that could be used for the experiment. In addition, larger crystals tended to have non-rectangular shapes, which made detwinning even more difficult. However, even twin-free crystals have appreciable pinning due to the YSZ-crucible induced defects discussed previously. Therefore, we began to look for an alternate superconductor that had less pinning than YBCO. $Bi_2Sr_2CaCu_2O_{8+\delta}$ (BSCCO hereafter) seemed to be a good candidate. Unlike YBCO, BSCCO does not have twin boundaries.[16] Moreover, BSCCO is electronically much more anisotropic than YBCO, which reduces the vortex pinning energy immensely. Thus, we expected that vortices would move more freely in BSCCO crystals. Also, it has been determined that the melting temperature of the flux line lattice is below liquid nitrogen temperature.

---

[16]S. E. Stupp and D. M. Ginsberg, in Physical Properties of High Temperature Superconductors III, D. M. Ginsberg Ed., World Scientific, p. 20, 1992.

61

For our experiment, we received a BSCCO crystal from a Japanese group.[17] Because the crystal was too large for our experiment, we tried to cleave it in half. But it ended up in four pieces because BSCCO cleaves easily in the c-axis direction. The piece we used for the experiment had a size of 2.3 mm × 2.7 mm. The mass of the crystal was 2.305 mg.
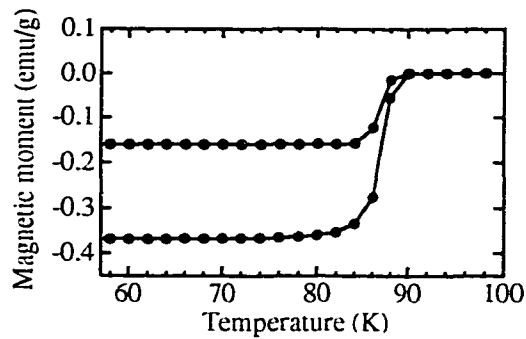
Fig. 3.10.   Superconducting transition of a BSCCO single crystal. The upper branch is taken field-cooling while the lower branch is after zero-field cooling. The applied magnetic field was one gauss in the c-axis direction.

First we characterize its superconducting transition using our Quantum Design SQUID. The sample was zero-field-cooled to 20 K; then a magnetic field of 1 gauss was applied to the c-axis. After warming to 100 K, the sample was field-cooled to 20 K. Figure 3.10 is the result of the measurement. The onset of superconductivity was at about 90 K. Although the transition was rather wide, it should not have posed any problem because the experiments were to be performed at liquid-nitrogen temperature, which is 77 K. Besides, according to

---

[17]Y. Ando at CRIEPI, Tokyo, Japan.

62

Ginsberg et al., the superconducting properties of the as-grown crystals are generally not improved by post annealing in oxygen.[18] Hence we proceeded without any attempt to improve the crystal.

Next, the BSCCO crystal was glued to one end of the head of an oscillator perpendicular to its surface. Because the crystal was very large, there should not have been any effect from edges of the crystal such as pinning at the edges. After the probe was pumped down and helium gas was put in as an exchange gas, the probe was cooled down to liquid-nitrogen temperature. First, capacitive excitation of the oscillator was performed to study dissipation and resonant frequency enhancement. Figure 3.11 shows the resonance peaks of the lower- and upper torsional modes. The phase of the signal shown corresponds to the absorptive response of the oscillator. The phase was the same as that for the YBCO measurements. In each plot, there are three lines. During the first frequency sweep, the magnetic field was off. Then the magnetic field was turned on in either of two directions. In the figure, only two lines are visible because the field direction did not make a difference and thus these two lines are on top of each other. The left plot is of the lower-torsional mode. For this mode, the oscillator was capacitively excited with a 0.2 V_{pp} driving signal and a 70 V bias. In this mode, the effect of the interaction between the magnetic flux and the superconductor was very small. The amplitude of oscillator motion was slightly smaller when the magnetic filed was applied than without an applied field. The quality factor of this mode was about 5,000, and thus the excess dissipation when

[18]S. E. Stupp and D. M. Ginsberg, in Physical Properties of High Temperature Superconductors III, D. M. Ginsberg Ed., World Scientific, p. 21, 1992.

the field is on is difficult to see. The right plot is of the upper-torsional mode. For this mode, we applied a 2 V_{pp} driving signal to the capacitive-excitation electrode while the oscillator was biased at 250 V. This mode clearly showed that the vortices were moving at 77 K in the BSCCO crystal. When the magnetic field was on, the oscillation was damped due to a viscous force in the superconductor. The quality factor of the higher resonance peak was 29,000 while that of the lower resonance peak was only 19,000. The change in dissipation $\propto$ $1/Q_H - 1/Q_o =$ 1.8×10^{-5} is much larger than any we got with YBCO crystals. Thus, we proceeded with further experiments with confidence that vortices were moving at 77 K.
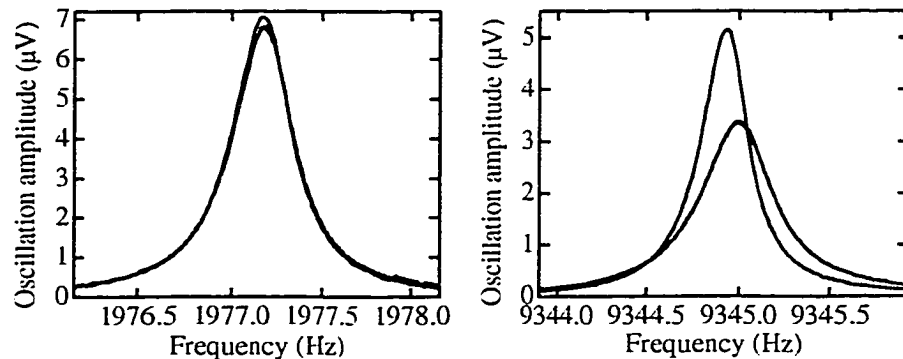
Fig. 3.11. Resonance peaks of an oscillator with a BSCCO crystal. The oscillator was capacitively excited. The left plot is of the lower torsional mode while the plot on the right is of the upper torsional mode. The effect of flux motion in the superconductor is prominent for the upper torsional mode. Q decreased from 29,000 to 19,000 due to the dissipation through flux motion.

64

The next step in the experiment was to measure the viscous force by moving the magnetic flux, which penetrated the superconductor in the c-axis direction, perpendicular to the oscillator. In this configuration, forces along the motion of the flux could be measured by the oscillator motion. Figure 3.12 compares the results for YBCO and BSCCO. For both cases, the temperature was 77 K. (At this temperature, we had confirmed that magnetic fluxes would not move in YBCO by comparing the capacitively-excited oscillation amplitude with and without a magnetic field. At 77 K, the two peaks had the same height, which indicates no measurable dissipation. The resonance frequency was shifted by the pinning force, however.) To move the electromagnet, two opposite quadrants of the piezo tube were driven with 15 V_{pp} signals such that the piezo would move perpendicular to the oscillator surface. The only different condition was that the bias voltage in the case of YBCO was 200 V while 250 V was used as a bias during the measurements on BSCCO. Thus, to compare the results, oscillation amplitude for YBCO should be multiplied by 1.25. The difference in the resonance frequencies was due to the difference in mass of the two superconducting crystals. The BSCCO crystal was 2.3 mg, which was nearly ten times more massive than the YBCO crystal. As can be seen in the figure, there is a 180° phase shift between the force on YBCO and that on BSCCO.

65
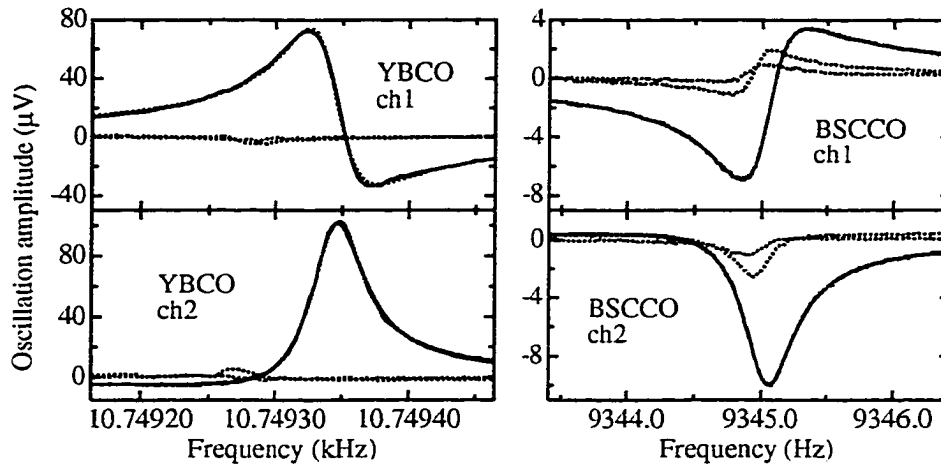
Fig. 3.12.   Effect of pinning/viscous forces in YBCO and BSCCO. Left plots
are of YBCO while right ones are of BSCCO. Top plots are from
channel 1 of the lock-in amplifier (SR530). Bottom plots are from
channel 2 of the lock-in. Dotted lines are when no magnetic field
was applied. No-field measurements were performed before and
after with-field measurements to ensure against baseline drift. The
with-field oscillation data were represented with dots. However, the
theoretical fit was so good that the dots barely show. The solid lines
are theoretical fits.

Curve-fit to the theoretical curves produced interesting results. Intuitively,
the force on YBCO seems much larger than that on BSCCO because the former
has about ten times higher peaks. But this was not the case. Table. 2.1. shows the
comparison of the forces on YBCO and BSCCO crystals. In the table, force and
dissipation are in arbitrary units. Forces are actually almost the same on YBCO
and BSCCO. The difference is dissipation; BSCCO has ten times larger
dissipation, thus it had a lower peak than YBCO (Recall that at resonance, the
amplitude $A = (F_0/k)Q$). The dissipation of the bare oscillator (the YBCO crystal
was attached, but no magnetic field was applied) in the same units is 0.021. Thus

66

the flux lines in YBCO crystals are essentially completely pinned, while for the BSCCO, they are unpinned. The phase difference at first appeared curious, being greater than the 90° shift expected between pinning and viscous forces (the pinning force is proportional to the displacement, the viscous force to the velocity). As it turned out, there was a resonance of the piezo tube between the frequencies used for YBCO and BSCCO. Thus, the phase of the excitation was affected by it. However, the mobile nature of the vortices in BSCCO in our experiment had been established. Also, it is clear from these initial characterizations that a thorough understanding of the oscillators, piezo, and magnet are necessary.

Table 3.1.   Comparison of forces on YBCO and BSCCO when the magnet was moved nearly perpendicular to the oscillator. The upper-torsional mode was used for this measurements. Data for a bare oscillator (YBCO crystal was attached, but no magnetic field was applied. Capacitive excitation (1.0 V_{pp}, 200 V bias)) is also listed for comparison.

	force (a.u.)	dissipation (a.u.)	f_0 (Hz)	phase
YBCO	0.027	0.024	10749.3	21°
BSCCO	0.023	0.24	9345.0	−160°
bare osc	0.0017	0.021	10749	-3.5°

67

Chapter 4: Experiments

4.1. FORCE MEASUREMENTS

A superconducting sample was glued on the top sidewall of the head of an oscillator. To avoid any torque, it was mounted such that its center is in the plane of the oscillator. Then the small electromagnet was carefully set to a position such that the superconductor was located right in the middle of the two magnet poles and the poles were in the plane of the oscillator (Fig. 4.1).
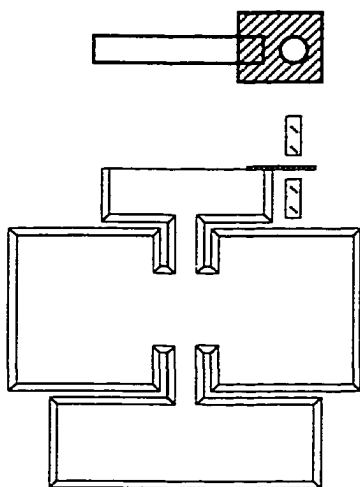
Fig. 4.1.   Top view and side view of an oscillator with a superconducting crystal mounted and a magnet set up for experiments.

We chose proper samples for each experiment. For the viscous and transverse force study, we selected a superconducting crystal whose irreversibility lines lay at lower temperature than average. We also set a temperature at which vortices would move freely. BSCCO crystals were chosen for the transverse force study because flux lines in BSCCO move even at 77 K. For the pinning force

68

study, on the other hand, we chose a crystal that had many pinning centers. YBCO crystals were chosen for this purpose. We also set as low a temperature as possible for this experiment.
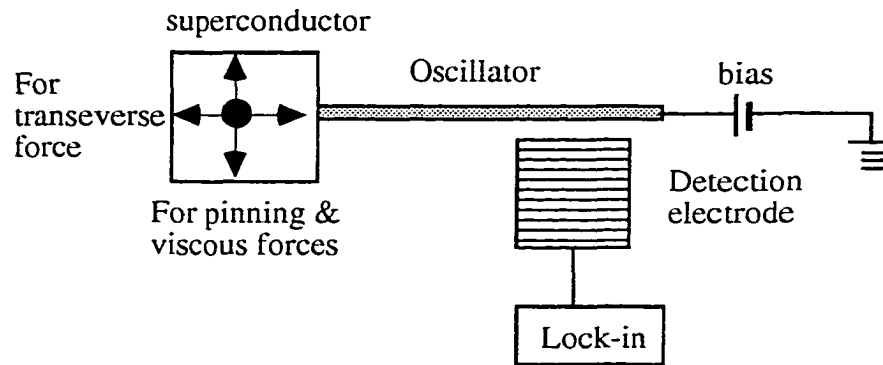
Fig. 4.2.   Top view of the excitation and detection system. Detection is done capacitively. To measure the transverse force, the magnet is driven parallel to the oscillator plane. It is driven perpendicular to the oscillator plane for the longitudinal force measurements.

We attached the single crystal to the head of the mechanical oscillator. We applied magnetic flux locally to the center of the single crystal. Care was taken to avoid edge-pinning effects. For the transverse force study, we drove the magnet parallel to the oscillator plane, making vortices follow the magnet. As a result, the oscillator would be excited only by forces that are transverse to the direction of vortex motion. For the pinning and viscous force study, the magnet was driven perpendicular to the oscillator plane. In this configuration, only forces along the motion of vortices excite the oscillator (Fig. 4.2). In reality, the

69

measurements were difficult due mainly to vibrations caused by mechanical coupling. The details of the solutions can be found in Chapter 3.

4.2. EXPERIMENTAL DETAILS

4.2.1. Experiment Preparation

This procedure is common to all the experiments done with the "Magnus force probe." The experiments were done in the NMR dewar. Unfortunately, the dewar has a leak between the sample space and the vacuum jacket as of November, 1998. Thus, the vacuum jacket must be pumped on with a diffusion pump while the dewar is cold until the dewar is fixed. However, vacuum pumps had to be turned off during actual data taking to avoid noise. Other than that, follow the standard procedure for dewar handling. Care was taken not to pump on the sample space or the helium jacket when the vacuum jacket is not evacuated. The wall between the helium jacket and the vacuum jacket is especially vulnerable because it is thin and the diameter is large; it might collapse.

Once the previous step was done, I closed the probe then pumped on it for at least a couple hours, preferably over night. Then I introduced exchange gas to control the temperature inside the probe. Since we change the temperature down to liquid-nitrogen temperature, the exchange gas has to be helium. I found that I had to use ~1000 mTorr of helium gas to make the response quick enough. To have that pressure at the low temperature, I had to put in ~4 Torr at room temperature, which was an apparent pressure of about 1 atm of helium when read

70

with a thermocouple gauge. This was kept consistent from one experiment to another.

After the exchange gas was put in, I inserted the probe into the dewar. During this step, I have broken many oscillators, not to mention more crystals. Since I added restraints to avoid collision between an oscillator and a crystal, I haven't broken any oscillators; but still, transferring the probe into the dewar should be done as gently as possible. This was also the reason why the final set-up inside the probe was done right next to the pumping station so that I didn't have to carry the probe or turn it upside down only to find out that the oscillator was broken.

To make sure that the oscillator and the crystal are safe, I compared the resonant frequencies before and after transferring the probe into the dewar. Another clue was the size of an offset. Remember the normal offset when everything is working. For example, the offset was about 10 μV for channel 1 and a fraction of μV for channel 2 when the excitation voltage was 10 V_{pp}. Whenever the offset was more than that, say 50 μV, either the oscillator was broken or the bias wasn't connected to the oscillator.

The temperature control was done with a LTC-20 temperature controller. I had to use the 50 W range possible because of the leak in the dewar. The power limit was maintained at or below 60%. The temperature controller assumes that the resistance of the heater is 50 Ω. In reality, the actual heater in the dewar is 25 Ω. So the display of the temperature controller is twice the actual power. I've found that if more than "40% of 50 W" power is required to maintain the set temperature, the needle valve is open too much; there's an accumulation of liquid

71

nitrogen in the sample space. Thus, I tried to maintain less than "35% of 50 W" power to control the temperature.

4.2.2. Measurements

Frequency sweep experiments were done with a HP 3325B function generator and a SR530 lock-in amplifier. They were controlled by a computer via GPIB with LabVIEW virtual instruments. Typically, I used a virtual instrument named "freq sweep lock-in X & Y."

Capacitive Excitation

Capacitive excitation was performed at each temperature as a reference. Because we could calculate the amplitude of a force by capacitive excitation, we used that to estimate the force exerted by moving magnetic fluxes. Moreover, when I needed to find the resonant frequency, I drove the oscillator capacitively since it was easy to find when capacitive excitation was used. Typically I applied 250 V bias to the oscillator. The excitation voltage at low temperatures was about 1 V_{pp} or less depending on the quality factor. Under this condition, the detected signal was a few tens of μV. At room temperature under atmosphere, the excitation voltage had to be 10 V_{pp} to see a detected signal of a few μV. The frequency step had to be small enough that the detected signal looked symmetric. If the step was too large, then the detected signal had a hump or, in some cases, oscillations after the peak in detected signal. But remember, the quality factor

72

was so high for the oscillators that $\Delta f \sim 0.001$ Hz was too large a step for some oscillators.

Excitation by Magnet

Once I found the resonant frequency, I drove the magnet. Piezo tube (.375 × .020 × 1.0, EBL #2) was purchased from Staveley Sensors, Inc.[1] The tube can take 300 V between OD and ID (OD positive), but I used regular op-amps, so I used ±15 V. The op-amp box I made has two 5× op-amps and one variable output with which I can change the phase and the amplitude. The power supply to the box should be about ±18 V because the output of the op-amps cannot swing to the supply voltage.

4.2.3. Active Vibration Cancellation

Despite the vibration reduction mechanism described earlier, there was still mechanical coupling between the piezo and the oscillator, which gave a larger detection signal than actual data. Therefore, we had to come up with some scheme that would cancel the vibration completely. To cancel the vibration of the oscillator caused by the piezo tube, we could capacitively excite the oscillator so that the net force on it would be zero. This plan worked well. We managed to stop the oscillator vibration. The details are given in Appendix.

The detected signal was noisier when piezo was driven. It seemed that the noise was not at all due to fluctuations of the oscillator; even when the bias was

---

[1] Phone 203-289-5428. Also see Koki's lab book 4:119.

73

off (i.e., motion cannot be detected capacitively) the lock-in signal fluctuated even a few 10 ths of a μV. Although I could not determine where the fluctuation came from, using longer time constants, say 1 sec, in the lock-in amplifier helped to reduce the fluctuation.

4.2.4. Pinning Force and Viscous Force

To measure the forces proportional to the vortex velocity, we have to use a superconducting crystal that has as few pinning centers as possible. Since the Magnus force could be measured only when the vortices are moving, we first have to make sure that the vortices are moving. There should be a 90° phase shift between the capacitively detected signal when vortices are pinned and when they are free to move. The reason is the following. If a vortex is pinned, then the force is proportional to the displacement of the magnet due to the stretched flux line. On the other hand, if the vortex moves, then the friction force becomes dominant, which is proportional to the velocity of the vortex. Assuming that the vortex follows the magnet motion, there is a 90° phase shift in the force exerted on the superconductor. This phase shift cannot be detected if the capacitive excitation is used because the oscillator motion is determined by the voltage on the excitation electrode. To measure this phase shift, therefore, we had to move the magnet. But cancellation of pick-up signal is essential. Here, what I mean by "pick-up signal" is the oscillator motion caused by mechanical coupling between the piezo and the oscillator. By capacitively exciting the oscillator with a phase-shifted

74

sinusoidal wave, it is possible to keep the oscillator still while the piezo is oscillating.

75

Chapter 5: Theories

5.1. DOUBLE-TORSIONAL OSCILLATOR

The double-torsional oscillator was designed so that it has a much smaller energy loss than simple torsional oscillators or reeds. The small energy loss makes the quality factor of the oscillator as high as 500,000 at the temperature of our experiments. This enables us to measure a small force, which was impossible to be measured by conventional mechanical reeds. The behavior of the oscillator can be understood quite easily by writing down its equations of motion. It has four basic modes: two torsional modes and two cantilever modes. Torsional modes involve twisting motion about the axis of the oscillator. In contrast, cantilever modes are flexing of the oscillator axis. Here, I derive the normal modes and show actual measurements on each normal mode.

5.1.1. Torsional Modes

Resonance Frequencies of Torsional Modes

The simplest model for the oscillator in a torsional mode is to approximate it with two rigid bars connected with a wire (Fig. 5.1). These two bars are also connected to an infinitely massive base via a wire. In the figures, I_1 and I_2 are the moments of inertia for the top bar (= head) and the bottom bar (= wing), respectively. The torque between the bars is τ_1. The torque between the wing and the base is τ_2. Let us denote the angles of rotations with respect to the base for the head and the wing θ_1 and θ_2, respectively (Fig. 5.2).

76
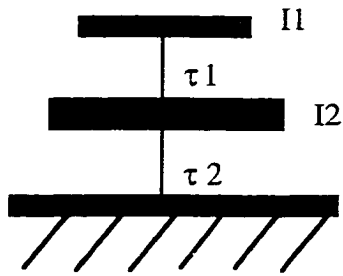
Fig. 5.1. A simple model of a double-torsional oscillator in a torsional mode. Subscripts 1 and 2 indicate the head and the wings, respectively. For example, moment of inertia of the head is denoted I_1 while that of the wings is denoted I_2. Likewise, τ_1 and τ_2 are torque on the axis of the oscillator between the head and the wings and between the wings and the base, respectively.
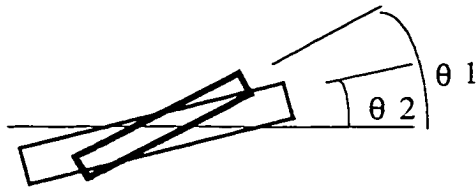
Fig. 5.2. Top view of an oscillator. Angle θ_1 is between the head and the base. Angle θ_2 is between the wings and the base.

Then the equations of motion are:

$$\tau_1 = -\kappa(\theta_1 - \theta_2) = I_1 \frac{d^2\theta_1}{dt^2}$$

$$\tau_2 = -\kappa\theta_2$$

$$\tau_2 - \tau_1 = I_2\frac{d^2\theta_2}{dt^2}$$

Assuming the solutions with sinusoidal time dependence; namely

$$\theta_1 = A_1 e^{-i\omega t}$$

$$\theta_2 = A_2 e^{-i\omega t},$$

the equations of motion become

$$-\theta_1 + \theta_2 = -\omega^2 \frac{I_1}{\kappa}\theta_1$$

77

$$\theta_1 - 2\theta_2 = -\omega^2 \frac{I_2}{\kappa}\theta_2.$$

By rearranging the terms, they can be written as

$$\begin{pmatrix} \omega^2\dfrac{I_1}{\kappa}-1 & 1 \\ 1 & \omega^2\dfrac{I_2}{\kappa}-2 \end{pmatrix}\begin{pmatrix} \theta_1 \\ \theta_2 \end{pmatrix} = 0.$$

To have nontrivial solutions the determinant of the matrix has to vanish. Therefore, the frequencies of the normal modes are

$$\omega^2 = \frac{\kappa}{2I_1I_2}[\,2I_1 + I_2 \pm \sqrt{4I_1{}^2 + I_2{}^2}\,].$$

Using the fact that $I_1 \ll I_2$, the resonance frequencies of the torsional modes can be approximated as

$$\omega_+{}^2 \approx \frac{\kappa}{I_2}(1 + \frac{I_2}{I_1} + \frac{I_1}{I_2}) \approx \frac{\kappa}{I_1} \qquad \text{for positive root,}$$

$$\omega_-{}^2 \approx \frac{\kappa}{I_2}(1 - \frac{I_1}{I_2}) \approx \frac{\kappa}{I_2} \qquad \text{for negative root.} \qquad (5.1)$$

The ratio of the angles of the head θ_1 and the wings θ_2 can be derived from this solution.

$$\theta_2 \sim -[\frac{I_1}{I_2} + (\frac{I_1}{I_2})^2]\,\theta_1 \sim -\frac{I_1}{I_2}\theta_1 \qquad \text{for positive root}$$

$$\theta_2 \sim [1 - \frac{I_1}{I_2}]\,\theta_1 \sim \theta_1 \qquad \text{for negative root.}$$

The normal mode with the negative root is where the wings and the head rotate in the same direction with almost the same angle. Thus we call this mode the 'symmetric' mode. The normal mode with the positive root, in contrast, is a mode where the wings and the head rotate in the opposite directions. The rotation angle of the head is much larger than that of the wing due to the small moment of inertia for the head. We call this mode the 'antisymmetric' mode.

78

The energy is localized. In the symmetric mode most of the energy is stored in the wing. Because of energy conservation, we can simply compare the maximum kinetic energy (or maximum potential energy) to find the total energies in the wing and the head. The ratio of the energies in the head to that in the wing is, using the approximation $\theta_1 = \theta_2$,

$$\frac{E_1}{E_2} = \frac{1/2 \; I_1 \omega^2 \theta_1^2}{1/2 \; I_2 \omega^2 \theta_2^2} = \frac{I_1}{I_2}.$$

Therefore, almost all the energy is stored in the wing ($E_2 \gg E_1$). On the other hand in the antisymmetric mode, using the approximation $\theta_2 = -\frac{I_1}{I_2}\theta_1$,

$$\frac{E_1}{E_2} = \frac{1/2 \; I_1 \omega^2 \theta_1^2}{1/2 \; I_2 \omega^2 \theta_2^2} = \frac{I_2}{I_1}.$$

Hence, the energy is stored mainly in the head ($E_1 \gg E_2$).

Real oscillators have loss mechanisms. The dominant mechanisms are dislocation motion and coupling to the base. The former one can be avoided by use of near-perfect single crystals as a material for the oscillators. Silicon wafers are especially good single crystals. Since they are used so much in the semiconductor industry, they are very inexpensive, considering their quality. To avoid the coupling to the base, we can use the antisymmetric mode. In this mode, it is the head that oscillates in a large angle. Compared to that, the wing does not move much, thus has little energy. For example, the energy of the wing of our oscillator is only 1/29 that of the head. Since the wing does not have so much energy to begin with, there will be little energy transfer into the base.

79

Oscillation Amplitude of the Torsional Modes

The motion of a double-torsional oscillator is analogous to that of two-mass-and-two-springs system (Fig. 5.3).
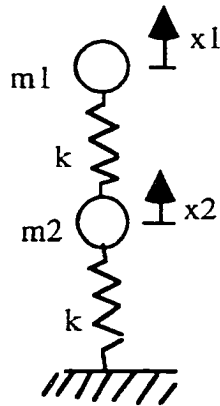
Fig. 5.3. A spring-and-mass model for the torsional modes of a double-torsional oscillator. This system and the torsional system are analogous.

The equations of motion for the system are

$$\begin{cases} m_1\ddot{x}_1 + \gamma\dot{x}_1 + k(x_1 - x_2) = F_1\, e^{-i\omega t} \\ m_2\ddot{x}_2 + \gamma\dot{x}_2 + kx_2 - k(x_1 - x_2) = F_2\, e^{-i\omega t} \end{cases}$$

We are looking for solutions that have sinusoidal time-dependence:

$$x_1 = A_1 e^{-i\omega t}$$

$$x_2 = A_2 e^{-i\omega t}$$

where A_1 and A_2 could be complex. So the equations of motion are now simplified as

$$\begin{cases} -m_1\omega^2 A_1 - i\gamma\omega A_1 + kA_1 - kA_2 = F_1 \\ -m_2\omega^2 A_2 - i\gamma\omega A_2 + 2kA_2 - kA_1 = F_2 \end{cases}$$

By simply eliminating either A_1 or A_2, we get

$$A_1 = \frac{1}{D}[kF_2 + F_1(2k - m_2\omega^2 - i\gamma\omega)]$$

$$A_2 = \frac{1}{D}[kF_1 + F_2(k - m_1\omega^2 - i\gamma\omega)]$$

80

where

$$D = m_1m_2\omega^4 - (k(2m_1 + m_2) + \gamma^2) \omega^2 + k^2 + i\{\gamma(m_1 + m_2)\omega^3 - 3k\gamma\omega\}$$

So, if we apply a force on the head (i.e., $F_1 = F$, $F_2 = 0$), the amplitude of the wing oscillation is

$$A_2 = \frac{kF}{D}.$$

To contrast, if we drive the wing with the same force (i.e., $F_1 = 0$, $F_2 = F$), then

$$A_2 = \frac{F(k - m_1\omega^2 - i\gamma\omega)}{D}.$$

To estimate the amplitude, calculate the natural frequency for the ideal system with no dissipation. The equations of motion are

$$\begin{cases} -m_1\omega^2 A_1 + kA_1 - kA_2 = 0 \\ -m_2\omega^2 A_2 + 2kA_2 - kA_1 = 0 \end{cases}$$

In order for non-trivial solutions to exist, the determinant must be zero:

$$\begin{vmatrix} -m_1\omega^2 + k & -k \\ -k & -m_2\omega^2 + 2kA_2 \end{vmatrix} = 0.$$

Thus, the natural frequency is

$$\omega_0^2 = \frac{k}{2m_1m_2}\{2m_1 + m_2 \pm \sqrt{4m_1^2 + m_2^2}.$$

The antisymmetric mode, which we use for our experiment, is the $+$ root. Since $\omega \approx \omega_0$ and $\sqrt{4m_1^2 + m_2^2} \approx m_2 + \frac{2m_1^2}{m_2}$,

$$m_1\omega^2 \approx \frac{k}{2m_2}[2m_1 + m_2 + m_2 + \frac{2m_1^2}{m_2} + ...]$$

$$\approx k(1 + \frac{m_1}{m_2} + \frac{m_1^2}{m_2^2} + ...).$$

But $m_1 \ll m_2$. Thus, when the wing is driven, then

$$A_2 = -\frac{kF}{D}\left(\frac{m_1}{m_2} + i\gamma\omega\right).$$

To summarize,

81

$$A_2 = \frac{kF}{D} \quad \text{if the head is driven by force F;}$$

$$= -\frac{kF}{D}\left(\frac{m_1}{m_2} - i\gamma\omega\right) \quad \text{if the wing is driven by force F.}$$

Therefore, wing-drive causes $\frac{m_1}{m_2}$ (= 1/30 in the case of the big oscillator)

oscillation amplitude of that of head-drive.[1]

Moments of Inertia
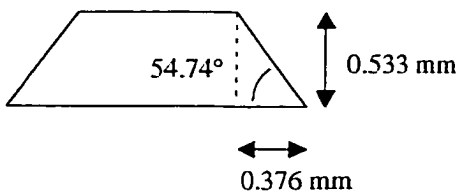
Fig. 5.4. A cross section of an oscillator made from a 4"-(100) silicon wafer. Bevels are (111) surfaces. Bevels significantly alter the size of oscillators on the top and bottom surfaces.
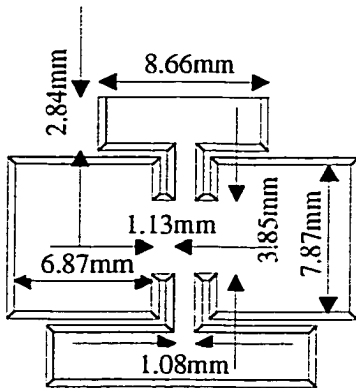
Fig. 5.5. Dimension of a double-torsional oscillator. The top edge of oscillators were usually cut flat so that we could glue a superconducting crystal on the sidewall perpendicular to the oscillator surface. The figure is two and half times the actual size except for the height of the base.

I originally used 3-inch silicon wafers to fabricate oscillators. But later I switched to 4-inch ones. 4-inch wafers are thicker than 3-inch ones, so I recalculated the moments of inertia of the head and the wing. The thickness of the wafers I purchased were 0.021 inches (0.533 mm) thick. (100) wafers have

---

[1]For details, see Koki's lab note 8:48–53.

82

54.74° bevels. Thus, the larger side is larger by 0.376 mm per bevel (see Fig. 5.4). This left only 0.36 mm space around wings. So, with the current design we cannot use any thicker wafers.

Figure 5.5 shows the measured dimensions of a real oscillator. This figure is drawn to scale except for the height of the base. To make calculations easy, I took the average of the dimensions of the two sides of the oscillator and assumed the edges to be vertical. The head is thus an approximately 8.28 mm × 2.65 mm rectangle. The top part of the head had been cut off with a diamond saw in order to mount a superconducting crystal on it. Each wing is like a rectangular paddle of 7.24 mm × 8.24 mm that is attached to a handle of 4.22 mm in width. The paddle is 1.46 mm to 8.70 mm from the axis. I calculated moments of inertia of the head and the wing assuming they rotate about the center of the neck. In other words, I ignored the finite width of the neck and thus their effect on the moments of inertia. Using the density of silicon 2.33 g/cm^3, I found that

$$I_1 = 1.56 \times 10^{-3} \text{ g-cm}^2$$

$$I_2 = 4.49 \times 10^{-2} \text{ g-cm}^2.$$

As usual, subscripts 1 and 2 represent the head and the wings, respectively. So, it turned out that the ratio of moment of inertia of the wings to that of the head is about 29, instead of 32 as calculated from the mask dimensions.

5.1.2. Cantilever Modes

Resonance Frequencies of Cantilever Modes

Cantilever modes resemble flexing of a cantilever. Since the bottom of the oscillator is clamped, the angle of the end is zero with respect to the plane of the oscillator. The wing and the head of the oscillator were assumed to be point masses; the wing is m_2 and the head is m_1. We assume that the torque required to flex the beams is proportional to the angular difference between the ends of the beams. Specifically, the bottom beam makes θ_2 with the equilibrium direction, so the torque is proportional to θ_2. The top beam has θ_1 at its top and θ_2 at its bottom, so the torque is proportional to $(\theta_2-\theta_1)$. First, we have to find the position of the masses m_1 and m_2. Let us denote their coordinations by (x_1,y_1) and (x_2,y_2). We further assume that each beam has the same length, l. This is a good assumption because the actual oscillators have the same length as well. Let's begin with the lower beam. At a distance r from the origin, the beam makes an angle $r\theta_2/l$. Thus,

$$dx = dr\ sin(r\theta_2/l) \approx dr\ r\theta_2/l \text{ and}$$
$$dy = dr\ cos(r\theta_2/l) \approx dr\ (1-\frac{(r\theta_2/l)^2}{2}).$$

By integrating these we get the position of the point mass m_2:

$$x_2 = \int_0^l dr\frac{r\theta_2}{l} = \frac{\theta_2}{2}$$
$$y_2 = \int_0^l dr(1-\frac{q_2^2 r^2}{2l^2}) = l(1-\frac{q_2^2}{6}).$$

84

We did a similar calculation for the upper beam. Letting r be a distance from the point mass m_2, one can write $\theta(r) = \theta_2 + \frac{\theta_1-\theta_2}{l}r$. Hence, the coordinates of the point mass m_1, which is the head of the oscillator, can be written as

$$x_1 = x_2 + \int_0^l dr(\theta_2 + \frac{\theta_1-\theta_2}{l}r = (\frac{\theta_1}{2} + \theta_2)l$$

$$y_1 = y_2 + \int_0^l dr(1 - \frac{(\theta_2 + \frac{\theta_1-\theta_2}{l})^2}{2}) = (2 - \frac{\theta_2^2}{3} - \frac{\theta_1\theta_2}{6} - \frac{\theta_1^2}{6})\,l.$$

Now, for simplicity we used the fact that $\theta_1, \theta_2 \ll 1$. Thus, we kept terms up to linear in θ's. Finally we get

$$x_1 = (\frac{\theta_1}{2} + \theta_2)l, \qquad\qquad y_1 = 2l\ ,$$

$$x_2 = \frac{\theta_2}{2}, \qquad\qquad y_2 = l\ .$$

The next step is to write down the equations of motion. Since the y coordinates are constants, we can think of the system in terms of force, not torque. The equation of motions for m_1 and m_2 are

$$m_1\ddot{x}_1 + k(\theta_1-\theta_2)l + \eta\dot{x}_1 = F_1 e^{i\omega t}$$

$$m_2\ddot{x}_2 + k(2\theta_2 - \theta_1)l + \eta\dot{x}_2 = F_2 e^{i\omega t}$$

Since we want to find steady-state solutions, we assume the same time-dependence as external force. Thus, $\theta_1 = \theta_{10}e^{i\omega t}$ and $\theta_2 = \theta_{20}e^{i\omega t}$. But for simplicity, we drop naught from subscripts hereafter. In a matrix form, the equations are

$$\begin{pmatrix} -\frac{m_1\omega^2}{2} + k + \frac{i\omega\eta}{2} & -m_1\omega^2 - k + i\omega\eta \\ -k & 2k - \frac{m_2\omega^2}{2} + \frac{i\omega\eta}{2} \end{pmatrix}\begin{pmatrix} \theta_1 \\ \theta_2 \end{pmatrix} = \begin{pmatrix} \frac{F_1}{l} \\ \frac{F_2}{l} \end{pmatrix}.$$

85

If there is no external force or dissipation, the determinant must vanish. Hence, the resonance frequency is

$$\omega^2 = \frac{k}{m_1}\left(1 + 4\frac{m_1}{m_2} \pm \sqrt{1 + 8\frac{m_1}{m_2} + 16\left(\frac{m_1}{m_2}\right)^2}\right).$$

Let us estimate m_1/m_2. The area of the head is 22 mm^2, while that of the wings is 132 mm^2. Thus, $m_1/m_2 = 1/6$. Unfortunately, this is too large to use the usual approximation of $\sqrt{1+x} = 1 + x/2$. Hence, we use the numerical value to proceed with the calculation. The resonance frequency was

$$\omega^2 = \frac{k}{m_1}(1.667 \pm 1.453) = \frac{k}{m_1} \times \begin{cases} 3.12 & \text{double cantilever mode} \\ 0.214 & \text{lower cantilever mode} \end{cases}.$$

Next, we calculated the motions of the head and the wing. By plugging in the resonance frequency into one of the equations of motion, we get

$$\frac{\theta_1}{\theta_2} = 2 - \frac{m_2\omega^2}{2k} = \begin{cases} -7.36 & \text{upper cantilever mode} \\ 1.36 & \text{lower cantilever mode} \end{cases}$$

Ratio of the amplitude of the oscillation of the head and the wing is therefore

$$\frac{x_1}{x_2} = \frac{\theta_1}{\theta_2} + 2 = \begin{cases} -5.36 & \text{upper cantilever mode} \\ 3.36 & \text{lower cantilever mode} \end{cases}$$

This tells that the head actually moves much more than the wing both in the upper and the lower cantilever mode. In the upper cantilever mode, the head moves in the opposite direction to the wing.

Effects of Driving Forces

Forces with the same amplitude excite different magnitudes of motion depending on whether they are exerted on the wing or the head of the oscillator. Let us assume a driving force on the head $F_1 e^{i\omega t}$ and a driving force on the wing $F_2 e^{i\omega t}$. Then, the equation of motion becomes

86

$$-m_1\omega^2\left(\frac{\theta_1}{2} + \theta_2\right) + k(\theta_1 - \theta_2)l + i\eta\omega\left(\frac{\theta_1}{2} + \theta_2\right) = \frac{F_1}{l}$$

$$-m_2\omega^2\frac{\theta_2}{2} + k(2\theta_2 - \theta_1)l + i\eta\omega\frac{\theta_2}{2} = \frac{F_2}{l}$$

Case 1) Driving force on the head

In this case $F_2 = 0$. From the two equations, we can derive that

$$\theta_2 = \frac{F_1}{l}\left[\frac{m_1m_2}{4k}\omega^4 - \frac{i\omega^3\eta}{4k}(m_1+m_2) - \left(2m_1 + \frac{m_2}{2} + \frac{\eta^2}{4k}\right)\omega^2 + \frac{5}{2}i\omega\eta + k\right]^{-1}.$$

Case 2) Driving force on the wing

In this case $F_1 = 0$. We get

$$\theta_2 = \frac{F_2}{l}\left(1 - \frac{m_1\omega^2}{2k} + \frac{i\omega\eta}{2k}\right)\times$$

$$\left[\frac{m_1m_2}{4k}\omega^4 - \frac{i\omega^3\eta}{4k}(m_1+m_2) - \left(2m_1 + \frac{m_2}{2} + \frac{\eta^2}{4k}\right)\omega^2 + \frac{5}{2}i\omega\eta + k\right]^{-1}.$$

Since $\frac{m_1\omega^2}{2k}$ is 1.56 for the upper cantilever mode and 0.107 for the lower

cantilever mode, we conclude that

$$\frac{\theta_2(\text{wing drive})}{\theta_2(\text{head drive})} = \begin{cases} -0.56 & \text{upper cantilever mode} \\ 0.107 & \text{lower cantilever mode} \end{cases}$$

5.2. FORCE MEASUREMENT USING MECHANICAL OSCILLATORS

5.2.1. Vibrating Superconductors

The idea of using mechanical oscillators to study superconductivity is well established. While torsional oscillators, especially double-torsional oscillators, are not so common, the vibrating reed technique proved to be a powerful tool in the study of static and dynamic properties of the flux-line lattice.[2] Review articles

---

[2]M. Ziese, P. Esquinazi and H. F. Braun, Supercond. Sci. Technol. 7, 869–890 (1994).

87

by Ziese et al.[3] and Esquinazi[4] are especially helpful. Brandt has written many theoretical papers[5], which are very useful when we deal with vibrating superconductors. For our experiment, however, we derived all necessary formulas from very general models so that it is straightforward to interpret all aspects of the experiments. In this chapter, I describe the relationship between forces and experimental conditions and data.

5.2.2. Capacitive Excitation

Excitation Signal and its Driving Force

One way to excite an oscillator is to drive it capacitively. We placed two electrodes close to the oscillator. Each of them form a capacitor with the oscillator. By changing the voltage between the electrode and the oscillator, we can vary the force on the oscillator. Thus, it is easy to see that applying an ac-signal of the resonance frequency of the oscillator to the electrode will excite oscillation. To calculate the relationship between the amplitude of a driving ac-signal and the force exerted on the oscillator, we have to go back to freshman physics. The force between the plates of a parallel-plate capacitor is

$$F = \frac{CV^2}{2x}$$

where C is the capacitance, V is the voltage and x is the distance between the plates. The force can be derived in two ways.

Method 1) Force is a derivative of energy about distance:

<hr>

[3]M. Ziese, P. Esquinazi and H. F. Braun, Supercond. Sci. Technol. **7**, 869–890 (1994).
[4]P. Esquinazi, J. Low temp. Phys. **85**, 139 (1991).
[5]For example, E.H. Brandt, P. Esquinazi, H. Neckel, J. Low Temp. Phys. **63**, 187 (1986).

88

$$F = -\frac{du}{dx} = -\frac{d}{dx}\left(\frac{1}{2}CV^2\right) = -\frac{1}{2}\frac{\partial C}{\partial x}V^2 = \frac{CV^2}{2x}.$$

Method 2) The electric field due to one of the plates is $\frac{V}{2x}$. Thus,

$$F = QE = CV\frac{V}{2x} = \frac{CV^2}{2x}.$$

We are looking for solutions that have the forms

$$V = V_0 + V_1 e^{-i\omega t}$$

$$x = x_0 - x_1 e^{-i\omega t}$$

$$F = F_0 + F_1 e^{-i\omega t}.$$

where   V is the voltage between the oscillator and the detection electrode,

V_0 is the bias voltage

V_1 is the detected signal by the lock-in,

x is the distance between the oscillator and the detection electrode,

x_0 is the average gap, and

x_1 is the oscillation amplitude.

Hence,

$$F = \frac{CV^2}{2x} = \frac{\varepsilon_0 A V^2}{2x^2} = \frac{\varepsilon_0 A}{2x^2}(V_0 + V_1 e^{-i\omega t})^2 \approx \frac{\varepsilon_0 A}{2x^2}(V_0^2 + 2V_0 V_1 e^{-i\omega t}).$$

The term at 2ω is down in amplitude by V_0/V_1 and generally does not excite a mechanical resonance.

Since we can use the approximation

$$\frac{1}{x^2} = \frac{1}{(x_0 - x_1 e^{-i\omega t})^2} \approx \frac{1}{x_0^2}\left(1 + \frac{2x_1}{x_0}e^{-i\omega t}\right),$$

the force exerted on the oscillator is

$$F = \frac{\varepsilon_0 A}{2x_0^2}\left(1 + \frac{2x_1}{x_0}e^{-i\omega t}\right)(V_0^2 + 2V_0 V_1 e^{-i\omega t})$$

89

$$\approx \frac{\varepsilon_0 A}{2x_0{}^2}\left[V_0{}^2 + \left(2V_0V_1 + \frac{2x_1}{x_0} V_0{}^2\right)e^{-i\omega t}\right].$$

Typical values for V_0, V_1, x_0 and x_1 are 250 V, 1 V, 330 μm, and 2 nm, respectively.[6] The terms in the formula for the force are, therefore,

$$V_0{}^2 \approx 6 \cdot 10^4 \; V^2,$$

$$2V_0V_1 \approx 5 \cdot 10^2 \; V^2,$$

$$2\frac{x_1}{x_0} V_0{}^2 \approx 8 \cdot 10^{-1} \; V^2.$$

The third term is much smaller than the first two terms. Therefore, the force can be approximated by ignoring the third term

$$F \approx \frac{C_0V_0{}^2}{2x_0} + \frac{C_0V_0V_1}{x_0} e^{-i\omega t}.$$

The first term is a time-independent force. As soon as the bias voltage is applied to the oscillator, a large attractive force will be exerted on the oscillator. The second term has the same time dependence as the driving signal. Its typical value is

$$F_1 = \frac{1.06 \cdot 10^{-12} \; F \cdot 250 \; V \cdot 1.0 \; V}{330 \cdot 10^{-6} \; m} = 8 \cdot 10^{-7} \; N.$$

This is the force that drives the oscillator.

Driving Force and Oscillation Amplitude

The task is to find the oscillation amplitude from the driving force. The equation of motion for the system is

$$\frac{C_0V_0V_1}{x_0} e^{-i\omega t} - \gamma(x_1e^{-i\omega t})' - kx_1e^{-i\omega t} = m \, (x_1e^{-i\omega t})''.$$

Hence, the complex oscillation amplitude is

---

[6] See Koki's lab note 8:26.

90

$$x_1 = \frac{F}{m} \frac{[(\omega_0{}^2 - \omega^2) - i\frac{\gamma}{m}\omega]}{(\omega_0{}^2 - \omega^2)^2 + (\frac{\gamma}{m}\omega)^2} .$$

Denote the full-width-half-maximum of the imaginary (absorptive) part of x_1, which is usually written as x_{ab}, by $\Delta\omega$. Then, it is easy to see

$$\frac{\gamma}{m} = \Delta\omega.$$

At the resonance frequency of the ideal (i.e., no dissipation, no driving force) harmonic oscillator, this forced harmonic oscillator with dissipation has an imaginary part

$$x_{ab} = \frac{FQ}{m\omega_0{}^2} = \frac{FQ}{k}.$$

Alternatively, the spring constant k can be calculated from x_{ab}, Q and F. Indeed, the spring constant k is the hardest to estimate. x_{ab} could be estimated from the capacitively detected signal as shown below. One minor point is that the peak of x_{ab} is not exactly at the natural frequency ω_0, but is slightly off.[7]

5.2.3. Capacitive Detection

The amplitude of the oscillator motion can be calculated from the amplitude of the detected signal, the capacitance of the gap, the total capacitance of the detection circuit, the gap size, and the bias amplitude. The formula is

$$x_1 = \frac{CV_1x}{C_{gap}V} \approx \frac{V_1}{V_0} \frac{C_{parasitic}}{C_{gap}} x_0.$$

where V = overall voltage between the detection electrode and the oscillator, V_1 = the detected signal amplitude, V_0 = bias voltage, C = overall capacitance, C_{gap} =

[7]For details, see Koki's lab note 8:64, 71.

91

capacitance of the gap, $C_{parasitic}$ = capacitance other than the gap, e.g., coaxial cables. The derivation is the following. The total capacitance of the detection system is the sum of that between the oscillator and the detection electrode (C_{gap}) and that of coaxial cable and others ($C_{parasitic}$). The only time-dependent component is C_{gap}, which is ($\varepsilon_0 A/x$). We look for solutions that have sinusoidal time-dependence:

$$V = V_0 + V_1 e^{-i\omega t} \ ,$$

$$x = x_0 + x_1 e^{-i\omega t} \ .$$

Since the detection system is connected only to the lock-in, which has a very high input impedance (100 MΩ, 25 pF), the charge in the system is constant ($Q = CV$ = const). Taking the derivative, we can write

$$0 = \frac{dC}{dt} V + C \frac{dV}{dt}$$

$$= -\frac{C_{gap}}{x} (-i\omega x_1 e^{-i\omega t})V + C(-i\omega V_1 e^{-i\omega t}).$$

Thus, using the fact that $C_{parasitic} \gg C_{gap}$ and $V_1 \ll V_0$,

$$x_1 = \frac{CV_1 x}{C_{gap} V} \approx \frac{V_1}{V_0} \frac{C_{parasitic}}{C_{gap}} x_0.$$

Please note that V_1 is the peak voltage while the lock-in uses rms voltage. Incidentally, both the lock-in and the function generator use the term "peak-to-peak" when they actually mean "zero-to-peak." The function generator's 'rms' is quite strange, too.[8]

---

[8]See Koki's lab note 8:65 for details.

5.2.4. Pinning Force

Resonance frequency Shift due to Pinning Force

We investigate the phenomena of resonance frequency shift by pinned flux when the oscillator is driven capacitively. In the simplest picture the pinned flux lines are represented by a spring. Since one end of the flux line is fixed on the stationary magnet pole while the other end is fixed at the pinning center in the superconductor, the flux line should act like a spring of an effective spring constant of k. The force exerted by the 'spring' is proportional to the displacement of the superconductor relative to the magnet. Thus, the equations of motion for the double-torsional oscillator are

$$t_1 = -k(q_1 - q_2)$$
$$t_1 - kr^2 q_1 = I_1 \frac{d^2 q_1}{dt^2}$$

$$t_2 = -kq_2$$
$$t_2 - t_1 = I_2 \frac{dq_2}{dt^2}$$

where subscript 1 denotes either the head or the top neck between the head and the wing, subscript 2 denotes either the wing or the bottom neck between the wing and the base. The angles θ_1 and θ_2 are relative to the base. As usual we are looking for the steady state solution with sinusoidal time-dependence. So,

$$\theta_1 = A_1 e^{-i\omega t}, \theta_2 = A_2 e^{-i\omega t}.$$

So the equations of motion become very simple:

$$-\kappa(\theta_1 - \theta_2) - kr^2\theta_1 = -I_1\omega^2\theta_1$$

$$-\kappa\theta_2 + \kappa\theta_1 - \kappa\theta_2 = -I_2\omega^2\theta_2.$$

These equations can be rewritten in a matrix form:

93

$$
\begin{pmatrix} \dfrac{I_1\omega^2}{\kappa} - 1 - \dfrac{kr^2}{\kappa} & 1 \\ 1 & \dfrac{I_2\omega^2}{\kappa} - 2 \end{pmatrix} \begin{pmatrix} \theta_1 \\ \theta_2 \end{pmatrix} = 0
$$

To have non-trivial solutions, the determinant of the matrix must vanish:

$$
\left(\dfrac{I_1\omega^2}{\kappa} - 1 - \dfrac{kr^2}{\kappa} \right)\left(\dfrac{I_2\omega^2}{\kappa} - 2 \right) - 1 = 0.
$$

By solving the equation one can derive the resonance frequency of the oscillator with the pinning force. Denote the resonance frequency with and without the pinning force by ω' and ω, respectively. Realizing that the pinning force is so small that one has to keep terms only up to $O(krI_2/\kappa)$, the frequency shift change due to the pinning force on the head is

$$
\omega'^2 - \omega^2 = \left(1 + \dfrac{I_2 - 2I_1}{\sqrt{4I_1{}^2 + I_2{}^2}} \right)\dfrac{kr^2}{2I_1}.
$$

This result tells us that the pinning force exerted on the head makes the resonance frequency higher. What would happen if the pinning force is exerted on the wing instead? By similar calculation one can find that

$$
\omega'^2 - \omega^2 = \left(1 - \dfrac{I_2 - 2I_1}{\sqrt{4I_1{}^2 + I_2{}^2}} \right)\dfrac{kr^2}{2I_2}.
$$

Since $I_2 \gg I_1$ for our double-torsional oscillators, the resonance frequency is actually lower when the pinning force is applied on the wing. In addition, in the latter case the difference is much smaller than that in the former case because of the larger denominator. Therefore, the pinning force is more easily observable when the crystal is attached to the head of an oscillator.

94

Force due to Flux Line Stretch

The pinning force on the superconductor is at its largest when fluxes are completely pinned. When the magnet moves from its equilibrium position, the flux line is stretched. This stretched flux line causes an energy increase, thus it exerts a force to pull in the superconductor. I show there are two ways to compute the force. They give the same result.

1) Method 1

The energy density of the magnetic field is, in SI units,

$$u_m = \frac{B^2}{2\mu_0}.$$

The magnetic energy between one magnet pole and the superconductor is therefore

$$U_1 = \frac{B^2}{2\mu_0} A \frac{g}{2}$$

where A is the cross-sectional area of the magnet, g is the gap between the magnet poles. Now let's assume that the magnet moves to the side by a distance d. Then the magnetic field density increases:

$$B' = B \frac{((g/2)^2 + d^2)^{1/2}}{g/2}.$$

So in this case the energy is

$$U_2 = \frac{B^2}{2\mu_0} \left(1 + \frac{d^2}{(g/2)^2} \right) A(g/2).$$

Hence the energy difference is

$$\Delta U' = \frac{B^2}{2\mu_0} A \frac{g}{2} \frac{d^2}{(g/2)^2}.$$

However, we have to account for forces on both sides of the superconductor, so the total energy difference is

$$\Delta U = \frac{2B^2}{\mu_0} \frac{Ad^2}{g}.$$

95

As we know that the force is the derivative of the energy with respect to displacement:

$$F = \frac{\partial \Delta U}{\partial d} = \frac{2B^2 A d}{\mu_0 g}.$$

2) Method 2
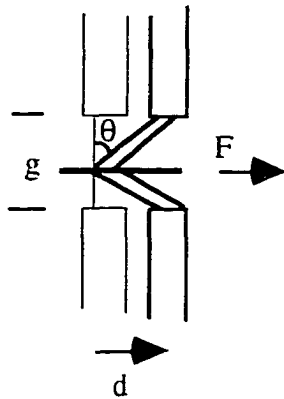
Fig. 5.6. Force on a superconductor by flux line stretch. When the magnet is moved from its equilibrium, a restoring force is exerted on the superconductor in the direction of the magnet motion.

The magnetic energy in the gap is

$$U = \frac{B^2}{2\mu_0} gA$$

where g is the gap, A is the cross-sectional area of the magnet, B is the magnetic field. Thus, the two poles of the magnet attract each other with a force of

$$F = \frac{B^2}{2\mu_0}A.$$

If the fluxes are pinned in the middle of the gap in a superconductor, then the same force will pull the superconductor toward the poles. Only when there is some displacement of the magnet from equilibrium will a net force be exerted on the superconductor in the direction of the displacement. This force is

$$F_{||} = F\sin\theta = F\tan\theta = F\frac{d}{g/2} = \frac{2Fd}{g}.$$

96

But we have to account for the force by each pole, so the force on the superconductor is

$$F_{||} = \frac{2B^2 A d}{\mu_0 g}.$$ (5.2)

Let us estimate the force exerted on the superconductor by driving the magnet. Using B = 0.15 T, diameter of the magnet core = 0.5 mm, d = 19 nm and g = 0.5 mm, we find that the force due to flux stretching is

$$F = 3 \times 10^{-7} \text{ N}.$$

5.3. CONCLUSION

In this chapter, we have derived the relation between forces on oscillators, the resulting oscillator motion, and the voltage eventually sensed by our detection scheme. Now we can quantitatively examine the behavior of vortices in superconductors.

Chapter 6: Results

6.1. NORMAL MODES

Figure 6.1 shows the normal modes of a real oscillator at T=77 K. The resonance peaks at ~1482 Hz and 1982 Hz were measured with 0.1 Vpp excitation and 100 V bias. Those at ~3921 Hz and 4193 Hz were with 10 V_{pp} excitation and 250 V bias.   Those at around 6327 Hz and 10.402 kHz were with 0.5 V_{pp} excitation and 250 V bias. The broken lines and the solid lines are data from channel 1 and channel 2 of the lock-in amplifier, respectively. Channel 1 detects the component in phase with the reference drive signal while channel 2 detects the 90°-out-of-phase component. The resonance at ~10.402 kHz is the antisymmetric torsional mode with the highest Q. Excitation and detection were done at the wings. Since the motion of the wings relative to the electrodes is the same in both torsional modes, the lock-in data should have the same phase characteristic, but opposite to the cantilever mode. That, and the predicted frequency estimates, leads us to conclude that the resonance at around 1982 Hz is the symmetric torsional mode.

Similarly, the resonance peaks at around 1482 Hz and 6327 Hz are cantilever modes. For a cantilever mode, the oscillator does not twist about its axis. Instead, it flexes at its axis. If the head and wings flex together, and most of the bend occurs between the base and the wing, it is called the symmetric or lower-cantilever mode. The head and the wing move approximately as one entity. The resonance at around 1482 Hz is the mode for this case. If bending occurs at

98

two positions, namely between the wings and the base and, in the opposite directions, between the wings and the head, the mode is antisymmetric and is called the upper-cantilever mode. The resonance at around 6327 Hz is due to this normal mode. The origin of the remaining two weak resonance peaks at around 3921 Hz and 4190 Hz is not immediately apparent, but may be "harmonics" of the lower neck in torsional motion (3921 Hz) or cantilever motion (4190 Hz).

It is interesting to compare the quality factors for the modes. The quality factor Q is defined as $\dfrac{2\pi \text{ energy stored}}{\text{energy loss per cycle}}$. More practically, one can divide the resonance frequency by the full-width-half-maximum of the absorptive peak of the detected signal. The antisymmetric torsional mode has by far the highest Q of 430,000. This Q is 50 times better than the next best Q. This confirms the superiority of using the antisymmetric torsional mode for small force detection.

6.1.1. Comparison with Models

We derived in Chapter 5 that the resonance frequencies of the cantilever modes are

$$\omega^2 = \frac{k}{m_1}(1.667 \pm 1.453) = \frac{k}{m_1} \times \begin{cases} 3.12 & \text{double cantilever mode} \\ 0.214 & \text{lower cantilever mode} \end{cases}$$

This simple theory predicts that the ratio of the resonance frequencies for the upper- and lower-cantilever modes is 3.8. As shown, the experimental values for the resonance frequencies of the cantilever modes were 6327 Hz and 1482 Hz for the upper- and lower-cantilever modes, respectively. The ratio of the experimental values is 4.3. Thus, the simple model presented here is approximately valid (~10% error).

99

We have also found that the theoretical resonance frequencies of the torsional modes based on the simple model presented in Chapter 5 are

$$\omega_+{}^2 = \frac{\kappa}{I_1} \qquad \text{for upper torsional mode,}$$

$$\omega_-{}^2 = \frac{\kappa}{I_2} \qquad \text{for lower torsional mode.}$$

Since the ratio of the moments of inertia is $I_1/I_2 = 29$, this model predicts the ratio of the resonance frequencies of the torsional modes to be

$$\frac{\omega_+}{\omega_-} = \sqrt{\frac{I_2}{I_1}} = 5.4$$

Experimentally, the resonance frequencies for the torsional modes are 10402 Hz and 1982 Hz. Thus, the ratio is 5.2. Thus, the model disagrees with the experimental results by 4%.

These comparisons prove that the simple models of the double-torsional oscillator are reasonably valid.

100
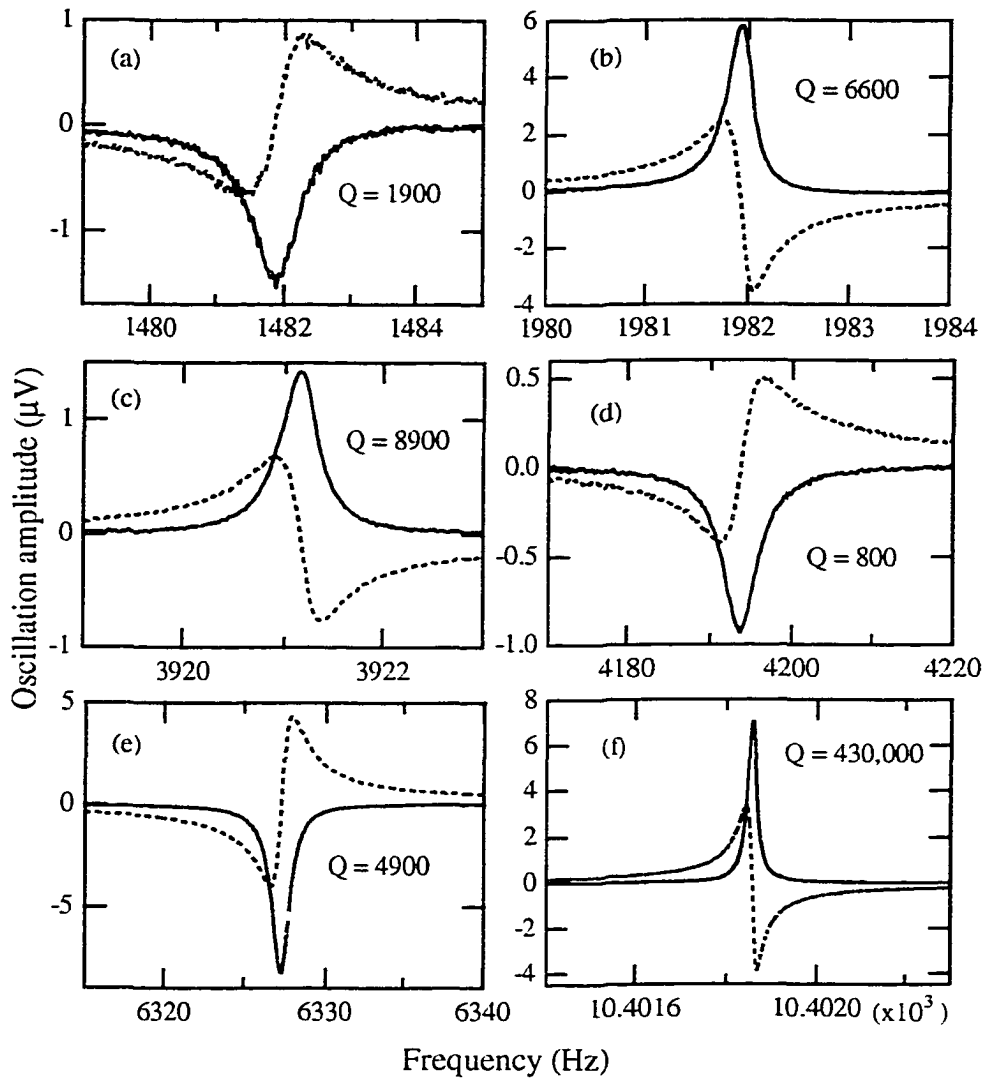
Fig. 6.1.   Normal modes of a double-torsional oscillator. Solid and dotted
lines are from channel 2 and channel 1 of a lock-in amplifier,
respectively. (a) and (e) are cantilever modes while (b) and (f) are
torsional modes. (c) and (d) are unknown modes. To excite, I
applied 0.1Vpp, 100V bias for (a) and (b); 10Vpp 250V bias for (c)
and (d); 0.5Vpp and 250 V bias for (e) and (f).

101

6.2. PINNING FORCE

6.2.1. Pinning Force

We measured the vibrational amplitude of the piezoelectric tube using interferometry. At room temperature, we determined that the tube moves 90 nm with 15 V_{pp} driving signal at 10 kHz. Since the oscillation amplitude is from zero to the maximum displacement, it is 45 nm. At room temperature, d_{31} of the piezoelectric tube is -1.73 Å/V. d_{31} is proportional to the sideways displacement of one end of the piezo tube Δx and they are related by the equation $\Delta x = 0.9VL^2/(d_m t)$, where L, d_m, and t are the length, the average diameter ((OD+ID)/2), and the wall thickness of the tube respectively, when equal and opposite voltages V are applied to opposite quadrants. d_{31} decreases to -0.75 Å/V at liquid-nitrogen temperature. Hence, we estimated that the amplitude of the magnet motion was 19 nm.

First, we use a fully pinned signal in YBCO to check our force measurements. The force due to flux line stretch was estimated to be, from Eq. 5.2,

$$F = \frac{2B^2 Ad}{\mu_0 g}$$

$$= \frac{2\,(0.15\ T)^2\ 2.0\times10^{-7}\ m^2\ 19\times10^{-9}\ m}{4\pi 10^{-7}\ Wb/A\text{-}m\ 5.0\times10^{-4}\ m}$$

$$= 2.7\times10^{-7}\ N. \tag{6.1}$$
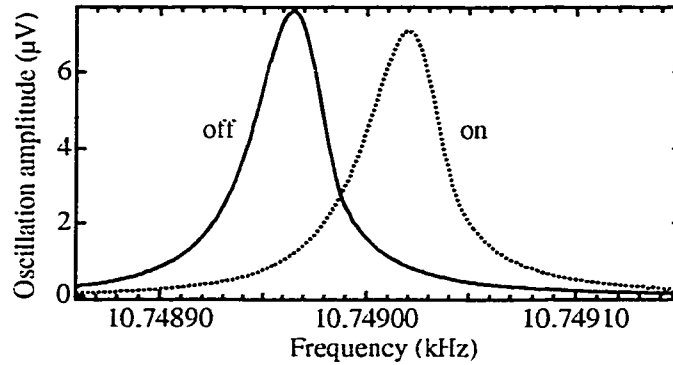
Fig. 6.2.   Frequency shift caused by the pinning force at 77 K. The oscillator
             is driven capacitively. The slight decrease in the peak height is
             caused by dissipation.

Meanwhile, we can estimate the force experienced by the oscillator from

the amplitude of the detected signal. At 77 K, when the oscillator was excited

capacitively in the upper-torsional mode with 1.0 V_{pp} driving and 200 V bias, the

curve fit of the detected signal showed that the driving force in experimental units

was 0.0017 Vs^{-2} (the magnet-off plot in Fig. 6.2). The units are 'Vs^{-2}' because

the model described in Appendix F was used to fit the detected signal in volts,

instead of using the oscillation amplitude in meters. Also, the fitted force is

actually $F_0/2m$ in Appendix F. These experimental units are converted to actual

force in N later in this chapter. The 1.0 Vpp, 200 V-bias capacitive excitation

exerts a force of

$$F = \frac{C_0 V_0 V_1}{x_0}$$

$$= \frac{1.06 \times 10^{-12} \, F \; 200V \; 1.0 \, V}{0.33 \times 10^{-3} \, m}$$

$$= 6.4 \times 10^{-7} \, N.$$

103

Recall that it is 29 times easier to drive the oscillator in its upper-torsional mode if the force is exerted on the head than on the wings. The capacitive excitation drives the oscillator on the wings. In contrast, the force caused by the magnet motion drives the oscillator on the head. Thus, to have the same oscillation amplitude as the capacitive excitation mentioned above, a force of 2.2×10^{-8} N is necessary.
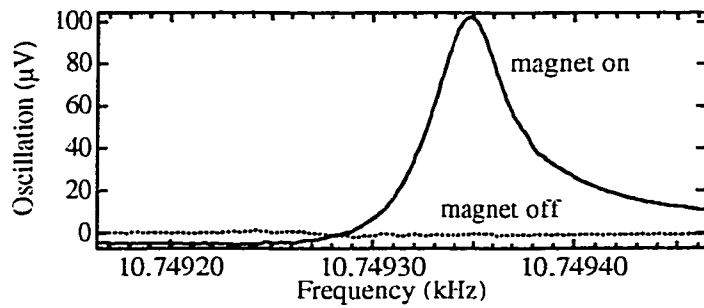
Fig. 6.3.   Detected signal when the magnet was driven perpendicular to the plane of the oscillator at 77 K. The driving voltage was ± 15 V_{pp} and the bias was 200 V. A YBCO crystal was attached to the oscillator. Phase delay was 21°.

When the piezo tube was driven with 15 V_{pp} driving, the curve fit of the detected signal due to the driving force was 0.027 Vs^{-2} (Fig. 6.3). This is the same as

$$\frac{2.2 \times 10^{-8} \text{ N}}{0.0017 \text{ Vs}^{-2}} 0.027 \text{ Vs}^{-2} = 3.5 \times 10^{-7} \text{ N}. \tag{6.2}$$

The reasonable agreement between Eqs. 6.1 and 6.2 shows the validity of the model of the flux-line stretch and that the force calibration in our experiment is reasonable. We determined that the pinning force per vortex due to the 19 nm magnet displacement is

104

2×10^{-14} N/vortex,

where I use the number of vortices = 1.45×10^7, the pinning force = 3×10^{-7} N.

6.2.2. Resonance Frequency Shift

The pinning force causes a resonance frequency shift as shown in Chapter 5. For the upper torsional mode, the shift is

$$\omega'^2 - \omega^2 = \left(1 + \frac{I_2 - 2I_1}{\sqrt{4I_1^2 + I_2^2}}\right)\frac{kr^2}{2I_1} \qquad (6.3)$$

where ω' and ω are the resonance frequency $(2\pi f)$ with and without a magnetic field, respectively, I_1 and I_2 are the moment of inertia for the head and the wings, respectively. k is the spring constant of the stretched magnetic flux, r is the distance between the axis of the oscillator and the pinned flux.

Figure 6.2 shows the resonance frequency shift at 77 K. The dotted line is when the field was on, while the solid line is when the field was off. The resonance frequency was $f_o' = 10749.019$ Hz and $f_o = 10748.965$ Hz with and without field, respectively. r was 5.0 mm. Also, $I_1 = 1.56\times10^{-3}$ g-cm^2 and $I_2 = 4.49\times10^{-2}$ g-cm^2. Substituting these into Eq. 6.3, the spring constant for the pinning force is determined as

k = 3.0×10^1 kg/s^2.

With the estimate for the magnet displacement of 19 nm, the force due pinning is

$$F = 19 \text{ nm} \cdot 3.0\times10^1 \text{ kg/s}^2 = 6\times10^{-7} \text{ N.} \qquad (6.4)$$

This force calculated from the frequency shift is about twice the size of that from the force fit of Eqs. 6.2 and 6.3. However, the difference can be easily accounted for by uncertainties in many of the values used for the calculations and the

105

simplicity of the models. So the pinning force per vortex by a 19 nm magnet displacement as determined by the resonance frequency shift was

$$4\times10^{-14} \text{ N/vortex.} \tag{6.5}$$

6.3. VISCOUS FORCE

Here, we compare the theoretical dissipation coefficient and the dissipation coefficient extracted from the experimental data. Following the Bardeen-Stephen results, Tinkham[1] obtained

$$\eta = \frac{\Phi_o H_{c2}}{\rho_n c^2} . \tag{6.6}$$

For the upper critical field at 77 K, we estimate value based on a paper by Palstra et al.[2]. We estimate $H_{c2}(77 \text{ K}) = 7.5$ T because the BSCCO crystal used for the experiment has the mid-point of the superconducting transition at about 87 K. According to Palstra et al., $-\frac{dH_{c2}}{dT} = 0.75$ T/K for H ∥ c. For the normal resistivity, we use the data by Martin et al.[3] The averaged ab-plane resistivity is about $\rho_n(77 \text{ K}) = 20 \ \mu\Omega$-cm (Fig. 6.4). Bear in mind that Eq. 6.6 is in the gaussian unit system. To compare with the experimental results, we used the following conversions: 1 gauss = 1 erg/cm^3 and $1 \ \Omega = \frac{1}{9} \times 10^{-11} \frac{s}{cm}$. The theoretical dissipation coefficient is therefore

$$\eta = 8\times10^{-7} \frac{g}{cm\text{-}s} . \tag{6.7}$$

---

[1]M. Tinkham, Introduction to Superconductivity, 2nd ed. McGraw-Hill, New York, 1996, p.169.
[2]T.T.M. Palstra et al., Phys. Rev. B 38, 5102 (1988).
[3]S. Martin et al., Appl. Phys. Lett. 54, 72 (1989).

106
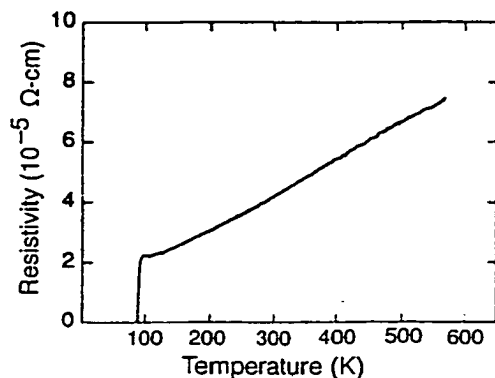
Fig. 6.4.   Averaged ab-plane
resistivity of a
$Bi_2Sr_2CaCu_2O_8$
single crystal. (from
Martin et al., 1989)
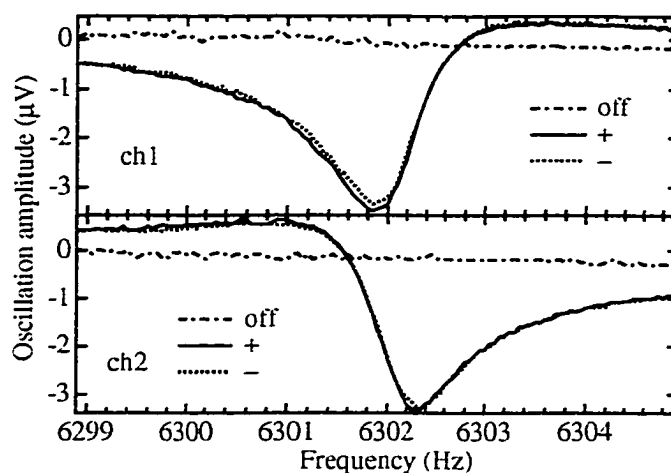
Fig. 6.5.   Upper cantilever mode oscillation when the magnet was moved
perpendicular to the plane of the oscillator with 15 V_{pp}. The bias
was 200 V. The oscillator was capacitively excited to
counterbalance the effect of vibration coupling. 'off' is data with
field off, '+' and '−' are data with field in positive and negative
directions, respectively. The upper and lower plots are signals from
Channel 1 and 2 of a lock-in amplifier, respectively. Phase delay
was 54°.

107

The experimental dissipation coefficient can be extracted from the curve fit of the magnet-driving data. Figure 6.5 is an example of such data. The oscillator was capacitively excited to counterbalance the vibration of the oscillator when the magnetic field was off. In the figure, the flat lines are those with no field. The magnet was driven perpendicular to the oscillator plane with 15 V_{pp}. The oscillator was biased at 200 V. Oscillator excitation with each direction of the magnetic field was measured. However, the oscillation amplitude was almost identical with either magnetic field direction as expected. The curve fit of these data reveal that

$$F_o/2m = 0.014 \ Vs^{-2}. \tag{6.8}$$

To convert this unit to a more natural one, we used a capacitive excitation data (Fig. 6.6). When the oscillator is excited capacitively with 0.5 V_{pp} driving signal and 200 V bias, the oscillator experiences

$$F_o = \frac{C_o V_o V_1}{X_o} = \frac{1.06 \times 10^{-12} \ F \ 200 \ V \ 0.5 \ V}{0.33 \times 10^{-3} \ m} = 3.2 \times 10^{-7} \ N \ .$$

The curve fit of these data showed that $F_o/2m = 0.0356 \ Vs^{-2}$. However, to excite the same amplitude of the upper cantilever mode, 0.56 F_0 is necessary if the head experiences the force rather than the wings as shown in Chapter 5. Thus, this shows that the conversion is

$$\frac{1.8 \times 10^{-7} \ N}{0.0356 \ Vs^{-2}} \ . \tag{6.9}$$

From Eqs. 6.8 and 6.9, the force experienced by the oscillator was

$$F_o = 7.1 \times 10^{-8} \ N. \tag{6.10}$$

The maximum velocity of the vortices is, from the magnet motion and the frequency,

108

$$v_v = 19 \text{ nm } 2\pi \ 6300 \text{ Hz} = 7.5 \times 10^{-4} \text{ m/s}. \tag{6.11}$$

Since $\mathbf{F} = \eta v_v$, the dissipation coefficient per vortex per unit length is

$$\eta = \frac{F}{v_v} \frac{1}{(\# \text{ of vortices})(\text{thickness of the crystal})}$$

$$= \frac{7.1 \times 10^{-8} \text{ N}}{7.5 \times 10^{-4} \text{ m/s}} \frac{1}{1.45 \times 10^7 \ 6.1 \times 10^{-3} \text{ cm}}$$

$$= 1 \times 10^{-6} \frac{\text{g}}{\text{cm-s}} \tag{6.12}$$

The difference between Eqs. 6.7 and 6.12 can be accounted for by uncertainties. For example, H_{c2} may not be 7.5 T for our sample. Similarly, large variations have been observed in ρ_n. To conclude, we have shown that the theory and the experiment agree reasonably well.
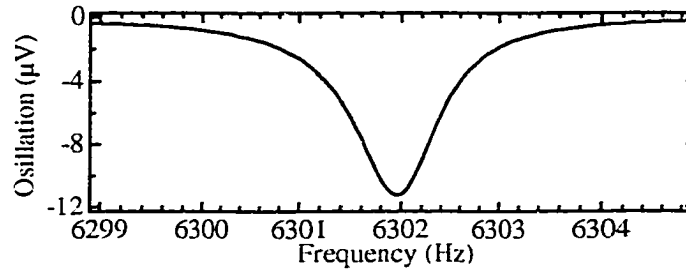
Fig. 6.6.   Capacitive excitation of the upper cantilever mode. A BSCCO crystal was attached to the oscillator. 0.5 V_{pp}, 200 V bias.

6.4. TRANSVERSE FORCE

Next we want to estimate the amplitude of the transverse force. Recall the form of the transverse force has been predicted to be

$$F = \alpha \frac{h}{2} n_s v \times \hat{z}.$$

109

To obtain the velocity is straightforward. Vortices in the superconductor tend to follow the magnet. So, at most, the velocity of the vortices is that of the magnet in the unpinned case. The maximum velocity of magnet motion can be calculated. When the driving frequency is 6.3 kHz and the oscillation amplitude is 19 nm, the maximum velocity is

$$v_{max} = 2\pi \, (6.3 \times 10^3 \text{ /s})(19 \text{ nm})$$

$$= 7.5 \times 10^{-4} \text{ m/s.}$$

The superconducting carrier density n_s at 77 K was estimated as follows. The penetration depth and the superconducting carrier density is related by[4]

$$\frac{1}{\lambda^2(T)} = \mu_0 \frac{e^2}{m^*} n_s(T)$$

where m^* is the effective mass of a superconducting pair. The temperature dependence of the penetration depth of BSCCO single crystals has been measured using a microwave technique.[5] Figure 6.7 shows that $\dfrac{\lambda_0^2}{\lambda(T)^2} = 0.25$ at T=77 K.

The effective mass for BSCCO is $m^* = 3m_e$.[6] Thus, if we use $m^* = 3m_e$, $n_s = 6.9 \times 10^{20} \text{ cm}^{-3}$. If we use the free electron mass, i.e., $m^* = 2m_e$, $n_s = 4.6 \times 10^{20} \text{ cm}^{-3}$. To be conservative, we chose $n_s = 5 \times 10^{20} \text{ cm}^{-3}$ for the following estimates.

---

[4]D.A. Bonn and W.N. Hardy, in Physical Properties of High Temperature Superconductors V, D.M. Ginsberg ed. World Scientific, Singapore, 1996.
[5]D.A. Bonn and W.N. Hardy, in Physical Properties of High Temperature Superconductors V, D.M. Ginsberg Ed., World Scientific, Singapore, 1996.
[6]P. Mandal et al., Phys. Rev. B **43**, 13102 (1991).

110
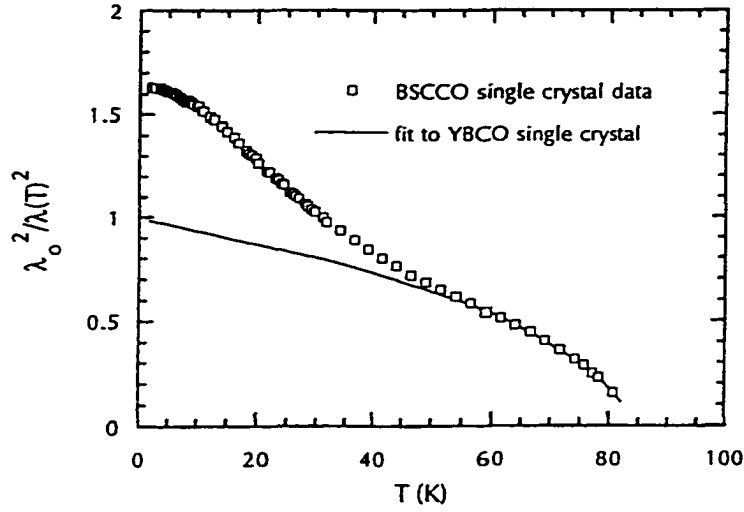
Fig. 6.7.   Penetration depth of BSCCO single crystal measured with a
microwave technique. $\lambda_0 = 1700$ to 1800 Å. (Taken from Bonn,
1996)

As just mentioned, the theories of the transverse force can be simplified as
$F = \alpha \frac{h}{2} n_s v \times \hat{z}$.

For example, Thouless et al.[7] predicts $\alpha = 1$, while Feigel'man predicts $\alpha \ll 1$.

Geller et al.[8] predicts $\alpha > 1$. If we use the values $n_s = 5 \times 10^{20} \, cm^{-3}$ and

$v = 7.5 \times 10^{-4}$ m/s, the force per vortex per unit length is

$$F_{theory} = \alpha \left| \frac{h}{2} n_s v \times \hat{z} \right| = \alpha \, 1.2 \times 10^{-10} \, N/m. \qquad (6.13)$$

A typical transverse force measurement is shown in Fig. 6.8. Here, the

piezo tube was driven parallel to the oscillator plane with 15 V_{pp} driving signal.

To make the piezo move exactly parallel to the oscillator plane and to

---

[7]D.J. Thouless, P. Ao and Q. Niu, Phys. Rev. Lett. **76**, 3758 (1996).
[8]M.R. Geller, C. Wexler and D.J .Thouless, Phys. Rev. B **57**, R8119 (1998).

111

counterbalance the vibration of the oscillator caused by the piezo motion, the oscillator and the remaining pair of the outer electrode of the piezo were also driven. The differences between the data with positive and negative magnetic fields are shown in Fig. 6.9. The small signal observed is due to residual misalignment (i.e., slight viscous, longitudinal component). However, only the difference between the positive and negative field directions is important, since only the transverse force is odd in a magnetic field.
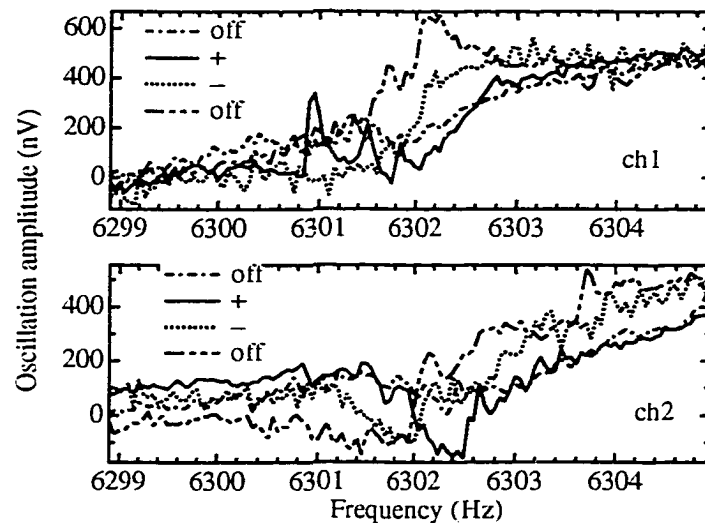
Fig. 6.8.   Upper cantilever mode when the magnet is moved parallel to the oscillator plane. Before and after the measurements with field on, the oscillator motion was monitored with field off to ensure good cancellation. The piezo was driven with 15 V_{pp}. The bias was 200 V.

Our measurements show that the difference in the transverse force between the positive and negative magnetic field directions is at most 0.2 μV (Fig. 6.9). These measurements were done using the upper-cantilever mode.

112

When the oscillator was capacitively excited in the upper-cantilever mode with 0.5 Vpp, 200 V bias driving, the peak height was 11.2 μV (Fig. 6.6). The driving force is, in this case, F = 3.2×10⁻⁷ N.
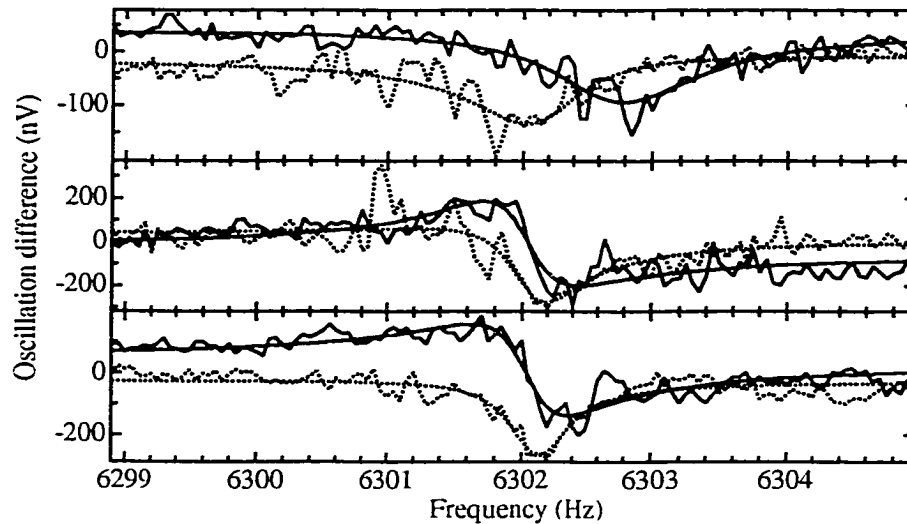
Fig. 6.9.   Difference in the detected signals with opposite magnetic field directions. The dotted lines and the solid lines are of channel 1 and channel 2, respectively. Each measurement is curve-fitted as shown.

If the head of the oscillator experiences a driving force, 0.56 times the driving force is necessary to drive the oscillator in the same amplitude, as has been shown earlier in this dissertation. Thus, the driving force to the head necessary to drive the oscillator is

$$\frac{1.8 \times 10^{-7} \, \text{N}}{11.2 \, \mu\text{V}}.$$

Since we see at most 0.2 μV difference between the detected signal for the two magnetic field directions, the upper limit of the transverse force is

113

$$F = 0.2 \ \mu V \ \frac{1.8 \times 10^{-7} \ N}{11.2 \ \mu V} = 3.2 \times 10^{-9} \ N. \qquad (6.14)$$

The amplitude of the transverse force extracted from the data in Fig. 6.9 is in the range of

$$\frac{F}{2m} = 0.0004 \ \text{to} \ 0.0009 \ Vs^{-2}.$$

Earlier in this chapter, we have established that for the upper torsional mode,

$$1.8 \times 10^{-7} \ N = 0.0356 \ Vs^{-2}.$$

Therefore, the transverse force experienced by the superconductor is

$$F = 2 \times 10^{-9} \ \text{to} \ 4 \times 10^{-9} \ N. \qquad (6.15)$$

Since the difference between the transverse forces with opposite field directions is twice the transverse force. Thus, from Eqs. 6.14 and 6.15, we conclude that the transverse force is

$$F \leq 2 \times 10^{-9} \ N.$$

We have measured that the magnetic flux in the magnet gap is 3.0 G-cm^2. Since the flux quanta is $\Phi_0 = 2.07$ G-cm^2, there are $\sim 1.45 \times 10^7$ vortices. Thus, the transverse force per vortex is at most

$$\frac{2 \times 10^{-9} \ N}{1.45 \times 10^7} = 1.4 \times 10^{-16} \ N.$$

The size of the BSCCO crystal was 2.3 mm$\times$2.7 mm and it weighed 2.305 mg. Using the experimental mass density of BSCCO[9], 6.2 g/cm^3, the thickness of the crystal was estimated to be 6.1×10^{-5} m. Thus, the experimental value of the transverse force per vortex per unit length is

$$F_{exp} = 2.3 \times 10^{-12} \ N/m. \qquad (6.14)$$

---

[9]F. Chang et al., Supercond. Sci. Technol. 6, 484 (1993).

114

Comparing the experimental value (Eq. 6.14) and the theoretical value (Eq. 6.13), the prefactor in the theory is

$$\alpha = 0.02.$$

This result supports the theories where $\alpha \ll 1$ is predicted.

We would like to go back to the theory by Kopnin and Salomaa.[10] Their theory is supported by other theory papers.[11,12] In these theories, the transverse force is

$$F = \frac{h}{2} n_0 \frac{(\omega_0 \tau)^2}{1 + (\omega_0 \tau)^2} \mathbf{v} \times \hat{\mathbf{z}}$$

where ω_0 is the core level spacing and τ is the relaxation time. The carrier density in their formula is not the superconducting carrier density, but the total carrier density. The density can be calculated from the Hall coefficient (Fig. 6.10) with the relationship $n_H = 1/eR_H$. Figure 6.12 is the doping dependence of the carrier concentration.[13] However, the total density is temperature dependent (Fig. 6.11). From these experimental data, we choose $n_0 = 3 \times 10^{27}$ m^3. Using theory, our data indicates $(\omega_0 \tau)^2 \leq 0.005$. This is somewhat smaller than the $\alpha = 0.02$ quoted above, since in this theory, n_0 ($> n_s$) is the relevant carrier density.

6.5. CONCLUSION

We have shown that the mechanical oscillator is a powerful tool to study small forces in superconductors. In particular, the capability to measure forces

---

[10]N.B. Kopnin and M.M. Salomaa, Phys. Rev. B **44**, 9667 (1991).
[11]A.V. Otterlo et al., Phys. Rev. Lett. **75**, 3736 (1995).
[12]M.V. Feigel'man et al., JETP Lett. **62**, 834 (1995).
[13]T. Tamegai et al., Jpn. J. Appl. Phys. **28**, L112 (1989).

115

directly is a unique, valuable feature of this technique. Our measurements reveal that the transverse force is actually much smaller than the classical hydrodynamic Magnus force. Given that recent theories based on very general arguments have asserted that the Magnus force has the classical form, our results renew the controversy once again. We have constrained the experimental transverse force to less than 1/50 of its classical value. It is hoped that in the future, these measurements can be extended in sensitivity, temperature range, field values, and materials studied. For example, future transverse force measurements could probe the temperature and field dependence of n_s directly.
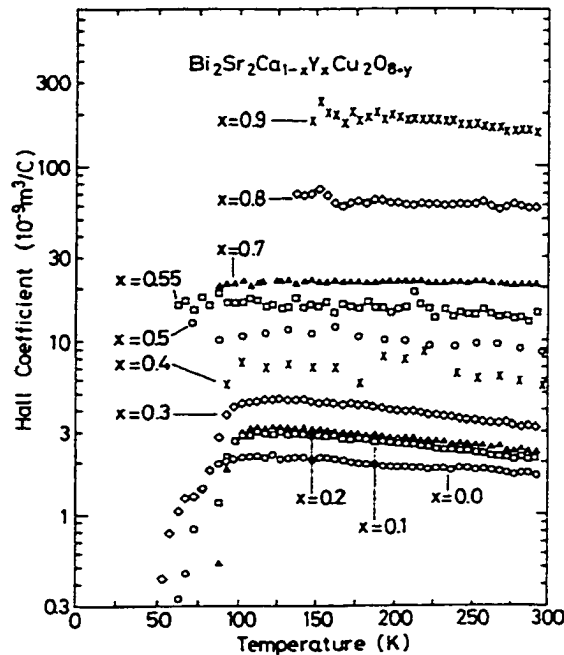
Fig. 6.10.   Temperature dependence of the Hall coefficients for the $Bi_2Sr_2Ca_{1-x}Y_xCu_2O_{8+y}$ system measured under the field of 5 T. (Taken from Tamegai, 1989).

116
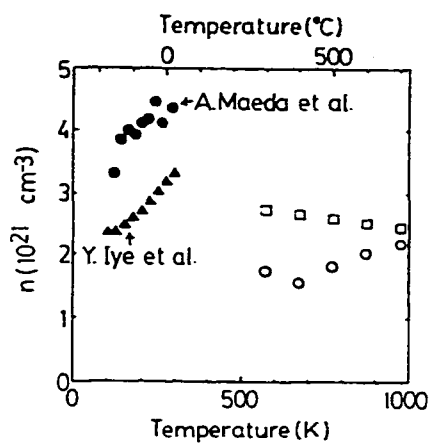
Fig. 6.11. Carrier density of BSCCO. (Taken from Idemoto et al.[14], 1991).
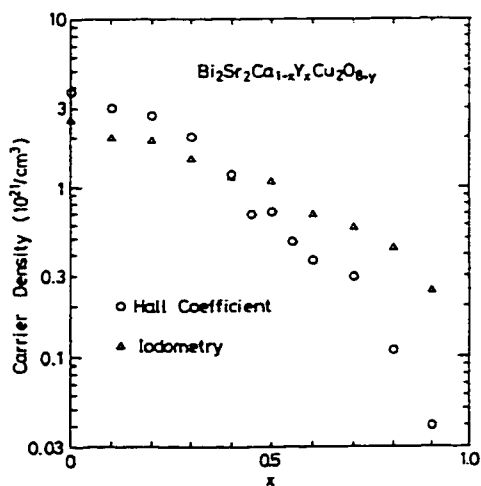
Fig. 6.12. Variation of the carrier concentration with x in $Bi_2Sr_2Ca_{1-x}Y_xCu_2O_{8+y}$ determined by the Hall coefficient and the iodometry method. (Taken from Tamegai[15], 1989).

[14]Y. Idemoto et al., Physica C 176, 325 (1991).
[15]T. Tamegai et al., Jpn. J. Appl. Phys. 28, L112 (1989).

Chapter 7: Dissipation Studies of Single Crystal YBa$_2$Cu$_3$O$_{7-\delta}$

We report the results of an investigation of vortex dissipation in the extremely low amplitude vortex motion regime. Single-crystal YBa$_2$Cu$_3$O$_{7-\delta}$ specimens were mounted on single-crystal silicon double-torsional oscillators. By utilizing such high-Q oscillators (Q $\approx$ 10^5–10^6), vortex dissipation and stiffness were investigated as a function of magnetic field H and temperature T for very low amplitude vortex motion. The usually smooth, single-peaked dissipation behavior gives way to multiple dissipation maxima at very low oscillation amplitude.

7.1. INTRODUCTION

The double-torsional oscillator technique that we applied to this study has evolved from the vibrating-reed techniques. The latter has been used widely to study flux lattice properties[1]. The double-torsional oscillators have a definite edge over the vibrating reeds; with Q's in excess of 10^5 at room temperature, they allow very small tilt angles of the samples and correspondingly extremely small ac fields. This technique has revealed that the dissipation behavior of YBa$_2$Cu$_3$O$_{7-\delta}$ crystals in a magnetic field has richer structures than those measured by vibrating reeds[2,3,4]. In this chapter, we show the results of some new

[1]M. Ziese, P. Esquinazi and H.F. Braun, Supercond. Sci. Technol. 7, 869 (1994).
[2]A.L. Barr and J.T. Markert, Phys. Rev. Lett. 77, 731 (1996).
[3]A.L. Barr and J.T. Markert, J. Superconductivity 8, 667 (1995).
[4]A.L. Barr, K. Mochizuki and J.T. Markert, Czech. J. Phys. 46, 1631 (1996).

118

measurements. We confirm the results of a previous study[5] by showing that truly linear behavior occurs only for very low-amplitude motion (angular amplitude less than $\sim 10^{-6}$ radians) and demonstrate that finer structures absent in the high-amplitude dissipation, particularly a very sharp feature near T_c, can be resolved in the low-amplitude limit.

7.2. EXPERIMENT

The double torsional oscillators were etched from silicon wafers as described in Chapter 2. Its Q is 2×10^5 at room temperature. The $YBa_2Cu_3O_{7-\delta}$ single crystals were grown in zirconia crucibles by a flux technique and then oxidized as described previously[6]. The sample used in this study has 10 %–90 % magnetic transition width of less than 1 K as determined by SQUID magnetometry. The onset of the transition is 92 K. The mass of the sample used here was 82 μg and its size was approximately 1 mm by 1 mm. To reduce the chance of flux pinning by the twin boundaries, a particular sample that has twin boundaries only in one direction was selected for the study. Then the sample was glued on the face of the oscillator in such a way that the applied field is perpendicular to both the crystallographic c-axis of the sample and the twin boundaries. The angle between the oscillator axis and the magnetic field was set to 2° in order to induce tilt oscillations.[7] Measurements were performed from

[5] A.L. Barr and J.T. Markert, J. Superconductivity 8, 667 (1995).
[6] R.B. Phelps et al., Phys. Rev. B 50, 6526 (1994).
[7] A.L. Barr, Ph.D. Thesis. (1996).

119

higher temperature to reduce the risk of trapped flux from the previous measurement.

7.3. RESULTS AND DISCUSSION

Fig. 7.1.   Dissipation data as a function of temperature for two values of tilt oscillation amplitude for single crystal $YBa_2Cu_3O_{7-\delta}$. The applied magnetic field was 6 T with $H \perp c$.

In Fig. 7.1 are shown the dissipation curves as a function of temperature for two driving amplitudes in a magnetic field of 6 T. When the tilt oscillation amplitude was small ($\sim 10^{-7}$ radians, the lower plot), there was a sharp peak at about 90.1 K in addition to a broad peak centered around 89.4 K. But when the

120

amplitude was increased to 6×10^{-6} radians, the sharp peak was washed away; thus we observed only the broad peak. These dissipation peaks probably reflect the effects of thermally activated flux diffusion[8]. The presence of two peaks may indicate the presence of two flux diffusion modes, a geometrical effect as discussed by Brandt[9], although we have been unable to fit our data using such analysis. The sharp and broad peaks may instead reflect transitions in vortex behavior, such as the vortex liquid to "smectic crystal" transition[10,11].

Figure 7.2 shows the driving-amplitude dependence of the sharp peak in more detail. The sharp peak was evident at tilt oscillation amplitudes less than 2×10^{-6} radians while it became just a lump on the slope of the broad peak at 3×10^{-6} radian. At tilt oscillation amplitudes larger than 3×10^{-6} rad, the sharp peak completely disappeared. Notice that the dissipation at the broad peak does not change at tilt oscillation amplitudes less than 2×10^{-6} radians. Above that driving amplitude, the dissipation begins to increase. Thus we identify $\sim1\times10^{-6}$ radians, corresponding to an effective ac magnetic field of ~0.05 Oe, as the limiting criterion for the observation of linear, low-amplitude behavior. It is obvious from Fig. 7.2 that the onset of nonlinear behavior and the smearing of fine dissipation feature occur suddenly as a function of tilt oscillation amplitude.

---

[8]M. Ziese, P. Esquinazi and H.F. Braun, Supercond. Sci. Technol. 7, 869 (1994).
[9]E.H. Brandt, Phys. Rev. Lett. 68, 3769 (1992).
[10]L. Balents and D.R. Nelson, Phys. Rev. Lett. 73, 2618 (1994).
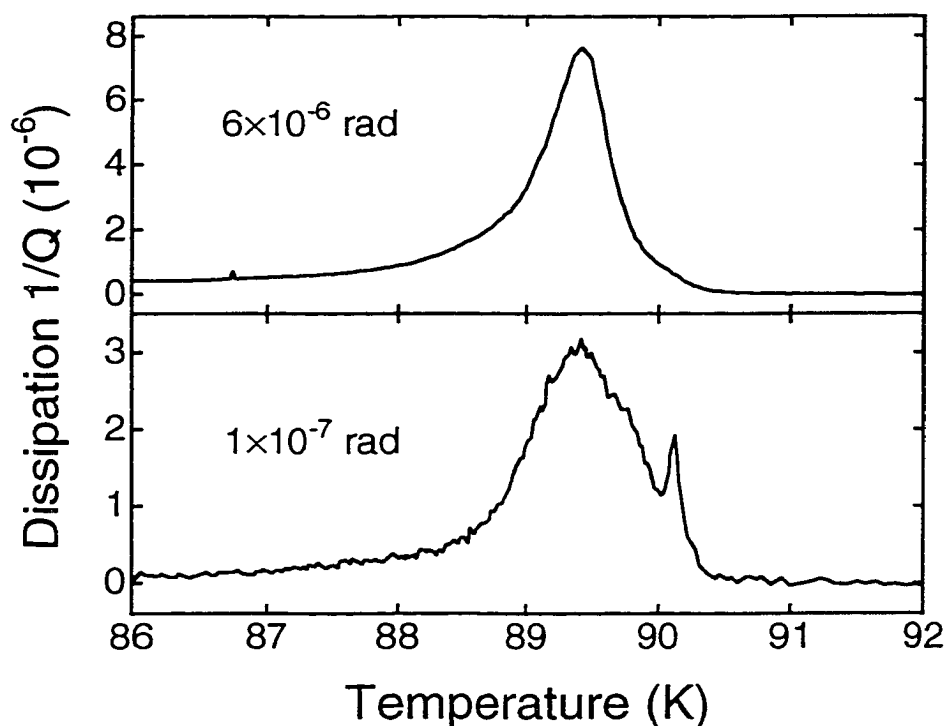[11]W. Jiang et al., Czech. J. Phys. 46, 1659 (1996).

121
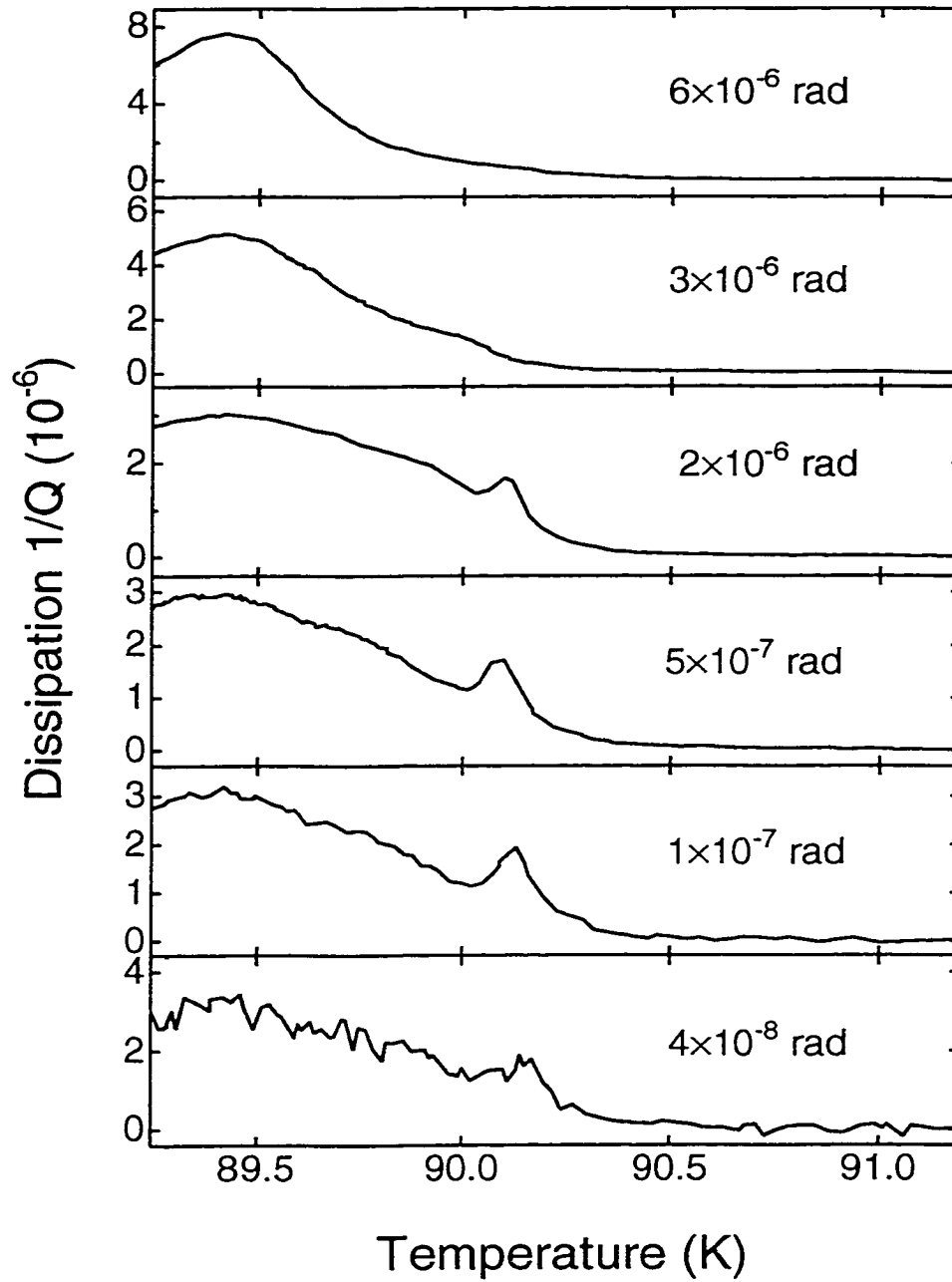
Fig. 7.2. Dissipation data as a function of temperature for various values of tilt oscillation amplitude for single crystal $YBa_2Cu_3O_{7-\delta}$. The applied magnetic field was 6 T with $H \perp c$.

122
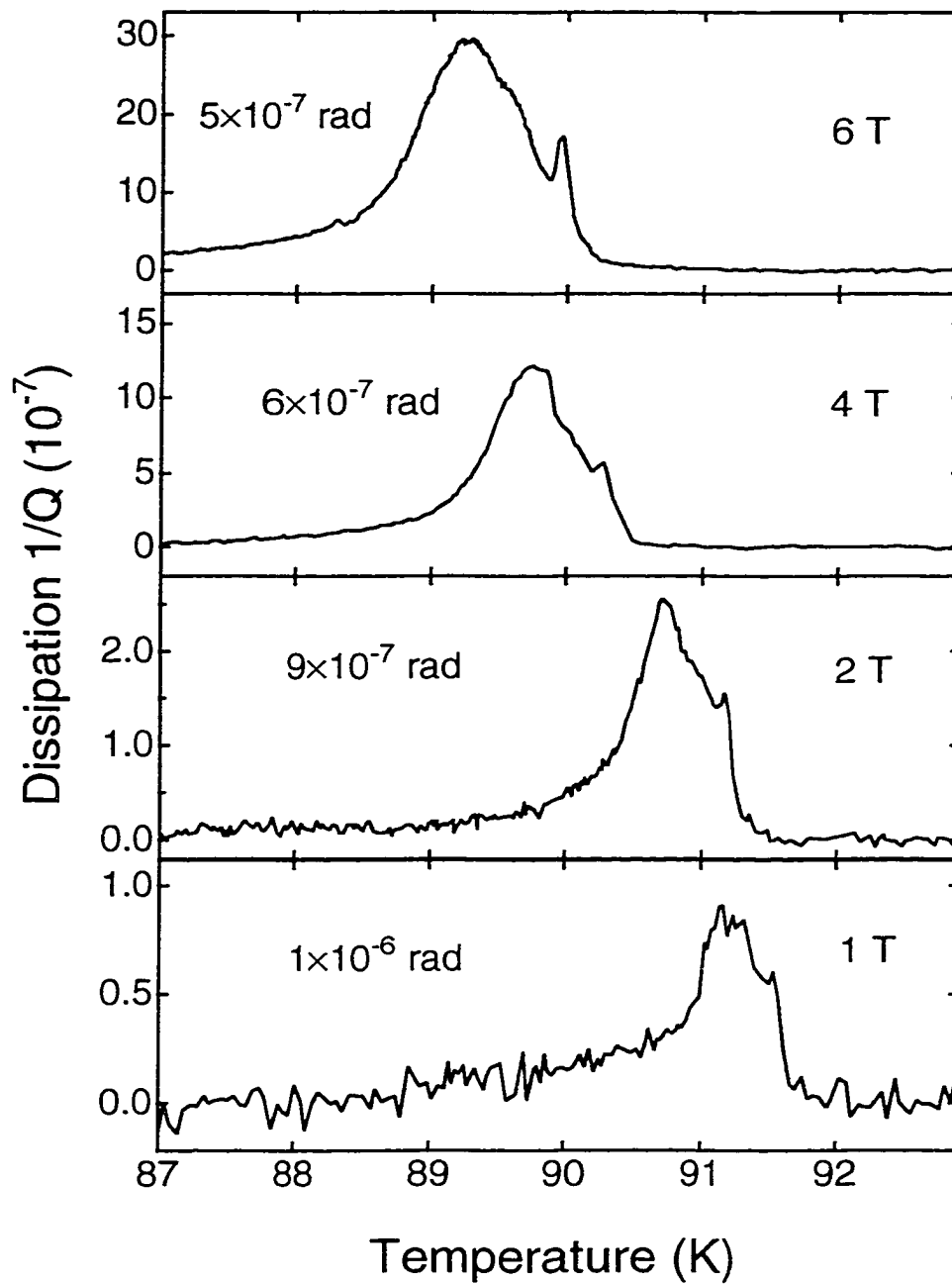
Fig. 7.3.   Dissipation data as a function of temperature for various magnetic fields for single crystal $YBa_2Cu_3O_{7-\delta}$ with $H \perp c$.

123

In Fig. 7.3 we show the dissipation curves as a function of temperature for various fields. The tilt oscillation amplitudes at the dissipation peak were between 5×10^{-7} rad to 1×10^{-6} rad. Both dissipation peaks shifted down in temperature as the applied field increases. Such a shift is expected for most vortex phenomena (melting lines and irreversibility lines generally exhibit a temperature dependence similar to that of the dissipation peaks observed here).

7.4. CONCLUSION

We have shown that the double-torsional oscillator is a powerful tool to study flux-line lattice phenomena. Unlike other mechanical techniques like vibrating reeds, the double-torsional oscillator with high Q can measure sufficiently small dissipation caused by flux diffusion that our low-amplitude data reveal fine minima and maxima in the dissipation data. In the present study the dissipation curves at low amplitude consist of two dominant regions: a sharp peak close to T_c and a broad peak at lower temperature. At higher tilt oscillation amplitudes, such structure is washed out, and only a single smooth peak can be observed. The sharp and broad peaks may be signatures of the vortex-liquid to smectic-crystal transition that has been proposed[12,13].

---

[12]L. Balents and D.R. Nelson, Phys. Rev. Lett. 73, 2618 (1994).
[13]W. Jiang et al., Czech. J. Phys. 46, 1659 (1996).

124

Appendices

A. PHOTOLITHOGRAPHY

A.1. In the Silicon Bay

Since the wafers were made of silicon and I didn't use any heavy metals, it was necessary to do the lithography in the silicon bay. It was a little difficult to get trained, but David Pierce, who is the supervisor of the cleanroom, called up superusers of the equipments and let me use the equipment.

The aligner in the silicon bay is the only aligner that the silicon people have—and expensive. So, please be careful when you use it. The main switch of the aligner, which is on the bottom box left of the aligner itself, should be on all the time. This switch turns off the mercury lamp. Thus, if it were turned off, it would take time for the lamp to stabilize. Check the table behind you. If the lens for quartz masks is there, you may proceed. Otherwise, have someone remove the lens from the aligner. If the switch on the box was set to 'CI1', change it 'CI2.' CI2 is for glass mask while CI1 is for quartz masks; we want 'CI2.' The smaller box on the main switch box is the power supply for the microscope; turn on the switch and check that the microscope is lit. Turn on the vacuum pump, which is to the right of the aligner. Turn on the power switch on the panel. Push the 'load' switch. After the message "exp time...," appears on the LCD screen push the 'align' button. Now, loosen the two knobs to remove the mask holder. Pull the holder just a fraction of an inch and wait till the microscope goes up completely in order not to hit the objective lenses with the holder. Then, remove the holder and

125

place it on a table upside down. Place a mask on the holder. Since the holder is upside-down, the metal side of the mask should be up. Then turn on the vacuum switch on the panel. The vacuum will keep the mask in place, but for additional safety, the mechanical latch should be set, too. This way, the mask would not fall even if the aligner has to be reset. Put the holder back and tighten the two knobs. Next, pull out the wafer stage. Place a wafer on the stage. There are small pins on the stage to guide; set the mask so that the flats are against the pins. Notice when the stage is pulled out completely vacuum is not working on the wafer. But as soon as the stage is pushed in, the wafers are evacuated; make sure the wafer doesn't move. Pull up the large lever on the left very gently. As soon as you feel some pressure, don't pull any further. You'll hear some clicks and the red light turns on the panel. The lever with white plastic on top is for alignment purposes; if the lever is pulled toward you, it makes a slight gap between the mask and the wafer, allowing the aligning knobs to be turned. But we use only one mask, so the aligning process is not necessary. Just make sure the lever is pushed back all the way to allow contact between the wafer and the mask. Should you want to pull out the wafer before exposure for some reason, do not push down the large lever; instead, push the 'chuck down' switch on the panel. Now we are ready for exposure. The exposure time should be 15 seconds. If not, push the 'set exp. time' switch and follow the instruction on the LCD. To expose, push the 'exposure' switch. Upon completion of exposure, the large lever is automatically pushed down. Pull the wafer stage out and repeat the cycle for the next wafer. When you finish using the aligner, remove the mask holder using the same precaution not to hit the objective lenses with the holder. Then place the holder

126

upside down. Turn off the vacuum switch on the panel and remove your mask. Then put the holder back in place. Turn off the power switch on the panel, microscope power, monitor switch, and vacuum pump. Do not forget to log in the notebook.

A.2. In the III-V Bay

Although the silicon bay has better equipment for photolithography, I was permitted to use only Neikerk's equipments in III-V bay. It turned out that the real problem was that once you start a process in the III-V bay then you have to use III-V equipment till the end. III-V people don't want silicon to be processed with their equipments. Likewise, silicon people don't allow anything to be processed with their equipments once it went in the III-V bay. So, the best way is to use only the silicon equipments from the beginning. The permission to use equipments are given on an individual basis, so you have to talk to the superuser for the equipment that you want to use. Often it is hard to have somebody train you; but don't despair. Ask David Pierce for help and be persistent.

The following is the process that I performed in the III-V bay; again, in the future lithography should be done in the silicon bay to avoid cross contamination. First I put photoresist 5214 EIR on the wafer and spun it at 4000 rpm for 40 sec. Then I placed the wafer in a 90°C oven to prebake for 30 min. Then, I used the Neikerk group's aligner to expose the wafer with UV. The exposure time ranged from 40 sec to 60 sec. It seemed that the wafer was underexposed if the exposure time was 40 sec. The developer was not AZ425, but AZ440. When I used the

127

former developer, it took more than five minutes to develop. The latter one developed in fifty seconds or so. After the exposure, the wafer was put in the post-bake oven, which was about 120°C. After the postbake, I used reactive ion etch to remove the nitride.

B. REACTIVE ION ETCH (RIE)

B.1. The Orange RIE (for silicon)

The setting used to etch 750 Å silicon nitride was:

Gas mixture: CHF_3 65 % (of 100 sccm), O_2 32 % (of 10 sccm). 50 mTorr

Power: 75 W

Duration: 2 min. (nitride thickness was about 750 Å).

The following are the details of the procedure for the RIE process using the orange RIE machine, which is also called "RIE #1" at MER.

1. Open the switch box on the wall and toggle the switches to 2A and 3A. Connect the connectors that are labeled 'PL2A' and 'PL3A'. Switch 1 and Connector 1 can be any since we don't use 'Gas 1.'

2. Go to the service corridor and make sure RF output (labeled PL42) goes to the slave chamber. Check that Connector PL16 with white tape is connected to C.M. gauge, which is located under the Main Input. There is another PL16 with red tape, but it is for the master chamber. Check if the two vacuum pumps are on.

3. Go back to the front of the machine. Check the water level of the reservoir, which is under the table. Turn the key to 'slave'. After

128

checking no light is on under 'control' on the master chamber panel, vent the slave chamber by pushing the 'vent' button twice. (if pushed once, the switch just flashes). Open the slave chamber and turn off the vent.

4. Place a wafer in the center of the chamber and close it. Then open the valve for the roughing pump. Make sure the arrow on the valve is pointing the slave chamber; if opposite, the master chamber is pumped. After pressure get below –25 in Hg, close the roughing valve and turn on 'pump' on the panel. Wait until the pressure gets down to 1 mTorr or less. Turn off 'pump' and turn on 'vent' to –5 in Hg. Pump down again.

5   Set the power to '250' on the display. This means that the power will be 25 % of the maximum power of 300 W; so we will get 75 W. Set Gas 2 to 65 %, Gas 3 to 32 %. Set the timer for the process (you can pick one from the three processes; I used Process 1) to 2.00 min. Find the small box between the master chamber and the slave chamber. Set the value of the pot to '50.0'. The switch right of it is '10V full scale'. The very right switch should be 'auto'.

6. Vent to –5 in Hg. Turn on 'Gas 2' and 'Gas 3'. Then turn on 'on' and 'auto' in this order. First open the roughing valve. After the pressure goes down below –25 in Hg, close the valve and turn on 'pump'. After a while, the etching will start automatically. It may take a couple of minutes for the process to start.

7. When the etch is done, turn off 'Gas 2' and 'Gas 3'. Then turn off 'on' and 'auto'. The 'vent' switch is blinking. Push the button twice to turn it

129

off. Turn on 'pump'. Then vent and pump once more. Then vent the chamber to atmosphere. Open the chamber and remove your wafer.

8.   After you etch all wafers, vent and pump on the chamber twice to keep it dry and under vacuum.

B.2. III-V RIE

For the wafers on which I performed photolithography in the III-V bay, I had to use III-V RIE. It turned out that III-V RIE etched the backside of wafers, too. As a result, I could not use some of the etched wafers because without the nitride film in the back, wafers would be etched from the back during the KOH etch process. So, the III-V RIE should be avoided at any cost.

Here's how RIE etch was done. The gas I used was O_2-CF_4. The RIE couldn't control the flow rate; the valve was either open or closed. By setting the "flow rate" setting to other than zero, the gas was on. The pressure inside the chamber was set to 200 mTorr; this controls the gas flow indirectly. The RF power was 120 W and the time duration was initially 7 min then increased to 7 min 50 sec. The nitride etch rate was said to be 110 Å/min. Since this machine will not be used for our purpose in the future, I'll not explain the details of the procedures. If interested in, please read my cleanroom notebook.

C. ACTIVE VIBRATION CANCELLATION

Here I explain the details of the process. First, the resonance frequency was found using capacitive excitation. I used 250 V bias most of the time. While

130

capacitive excitation with 3 Vpp (remember, 'peak-to-peak' actually means 'zero-to-peak') drive had only about 4 μV offset, piezo drive produced a much larger offset. When the opposing quadrants were driven with ±15 Vpp, typical offset of channel 1 was a little larger than 100 μV while the capacitively detected signal itself was a few 10 ths of 1 μV. Thus, in order to detect the signal with high sensitivity, I used A–B input of the lock-in amplifier so that I could use a lower voltage range. The detection electrode was connected to Input A while phase-shifted, amplitude-modified driving signal was connected to Input B. I adjusted the phase and the amplitude of Input B at 1 Hz below the resonance frequency so that offsets of channel 1 and channel 2 became about zero in the case of the upper-torsional mode. Then I changed the sensitivity to a much smaller scale. I could use 5 μV with no problem. After setting the relative offsets to zero at this frequency, I increased the frequency by 1 Hz so that the piezo was driven at the resonance frequency of the oscillator. Due to some mechanical coupling I got some pick-up. Without capacitive excitation, the detected signal due to mechanical coupling should be a few μV.[1] To counterbalance this coupling the oscillator was capacitively excited using a sinusoidal wave with the same frequency as piezo-driving wave but with adjusted phase and amplitude. To cancel the pick-up caused by piezo motion driven with ±15 Vpp wave, about one Vpp excitation drive was usually sufficient when the piezo was mounted on some springs. After I screwed down the piezo tube to its stage, then I need more like 10 Vpp. However, applying a capacitive excitation signal changed offsets. So, I had

---

[1] Should the detected signal be much larger than a few μV, some parts might be touching. There is no choice but to open the probe and readjust the positions of parts inside.

131

to frequently go back and forth between 1 Hz below and on resonance to ensure good cancellation. Another caution was that the offsets at 1 Hz above and below resonance were sometimes different. If this was the case one would want to adjust the relative offset such that they have the same amplitude but opposite sign at above and below resonance. This way one can adjust the capacitive excitation at resonance to make offsets zero. Fig. 10.5 is an example of such active cancellation. The sample was YBCO crystal. During the measurements, the magnet was driven by the piezo tube all the time. The flat lines are when the magnet was not on. When the magnet was turned on, then the periodic flux line stretch induced oscillator motion. The line with a negative peak was from channel 2 of a lock-in amplifier. The one with a positive and a negative peak was from channel 1 of the lock-in.

D. HEATING PROBLEM

One of the problems encountered was that the small electromagnet near the oscillator inside the probe heated up the oscillator and the crystal. This problem turned out to be quite difficult to overcome. Figure D.1 shows that a resonance frequency was shifted down at a temperature higher than T_c. This is a proof of heating. We concluded it was not due to the eddy current because the frequency shift did not happen immediately after the magnet was turned on. Rather, frequency shift got larger as time passed. Typically this shift was about 0.007 Hz to 0.01 Hz. Since the oscillators had very high Q, this shift was a

132

problem; the pinning force shifted up the resonance frequency by the same order of magnitude as frequency shift-down due to heating.

The balance between heating and pinning caused an apparent phase shift which resembles the expected phase shift that should happen when flux lines begin to move as I have explained elsewhere in this dissertation.
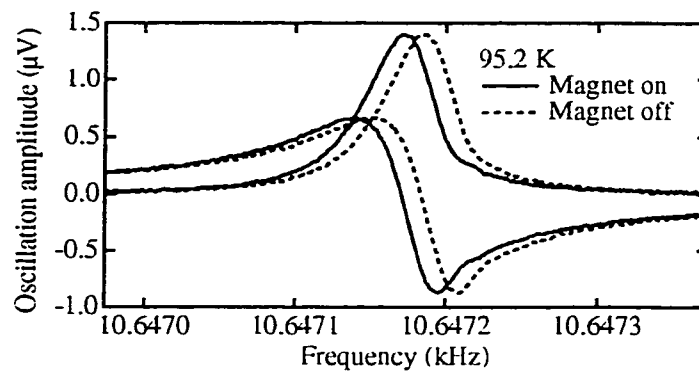

Fig. D.1.   Resonant frequency shift caused by heating. The direction of frequency shift is opposite from that due to the pinning force. This frequency shift happened even above Tc.

E. SUDDEN DEPINNING

It is plausible that vortices do not move smoothly following the magnet motion but suddenly jump from point to point. If this is the case, what would happen to the detected signals?
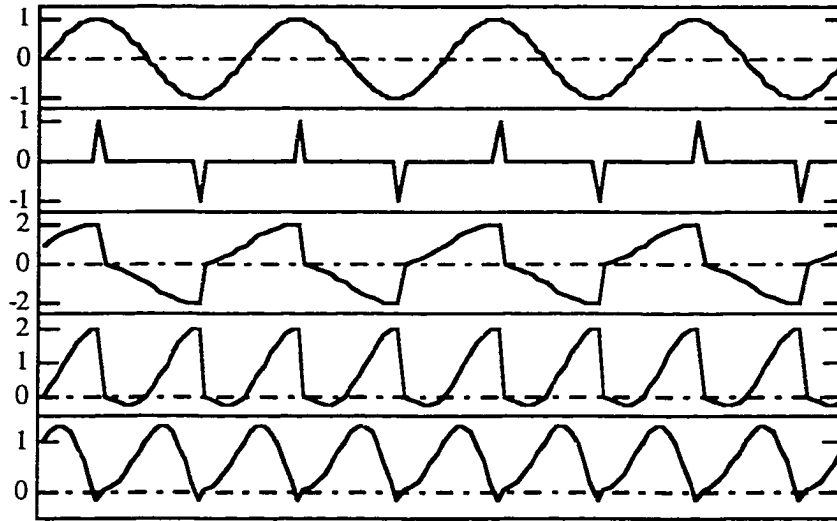
133

Fig. E.1.   Expected signals each vortex is suddenly depinned. The top is the
             displacement of the magnet. The second plot is the velocity of the
             vortex. It remains zero most of the time. Only at the maximum
             displacement, the vortex suddenly moves to relax the force. The
             third plot is the resulting force on the superconductor, thus on the
             oscillator. The fourth one is the expected signal from channel 1 of a
             lock-in. The last plot is the expected signal from channel 2.

One extreme case is that the vortices are pinned all the time expect when

the magnet displacement is maximum. Only when the flux lines are stretched the

longest, the pinned vortices move to relax the stretched lines. Figure E.1 depicts

this case. The top plot of Fig. E.1 is the motion of the magnet; so this is also the

displacement of the flux lines. The second plot of Fig. E.1 describes the velocity

of the vortices. They are pinned completely until the displacement reaches its

maximum. The third plot of Fig. E.1 is the force due to pinning. Every time

vortices move the force exerted on superconductor becomes zero because the flux

lines are not stretched at those moments. The fourth plot of Fig. E.1 is the product

of the first and the third plots. This is the in-phase component of the force on the

134

superconductor. The fifth plot of Fig. E.1 is the same as the fourth one except that the reference signal was the first plot with 90° phase shift. So, This is the 90°-out-of-phase component of the force. A lock-in amplifier measures only the DC components. The in-phase signal has 0.63 while the 90°-out-of-phase signal has 0.62.

The next example is very similar to the first example, except that the flux lines relax when the magnet displacement reaches its half-maximum (Fig. E.2). As the second plot shows, there are eight velocity spikes per cycle. If this is the case, the force due to the stretched flux lines can be expressed by the third plot of Fig. E.2. The fourth and the fifth plots of Fig. E.2 are in-phase and 90° out-of-phase components, respectively. The DC components of these signals, which the lock-in amplifier measures, are 0.15 for the in-phase one and 0.36 for the 90°-out-of-phase one.

These two cartoon models of depinning shows that phase will be shifted when fluxes are suddenly depinned. In an ideal case, where there's no pinning, the vortices follow the magnet. Thus we should see 90° phase shift because the drag force is proportional to the velocity, not the displacement. As can be seen clearly from Figs. E.1 and E.2 the same phase shift should be observed at an extreme case where vortices are moved by infinitesimal force. Even when the jump occurs at the maximum displacements as in the first set of plots, the phase shift is already about 45°.
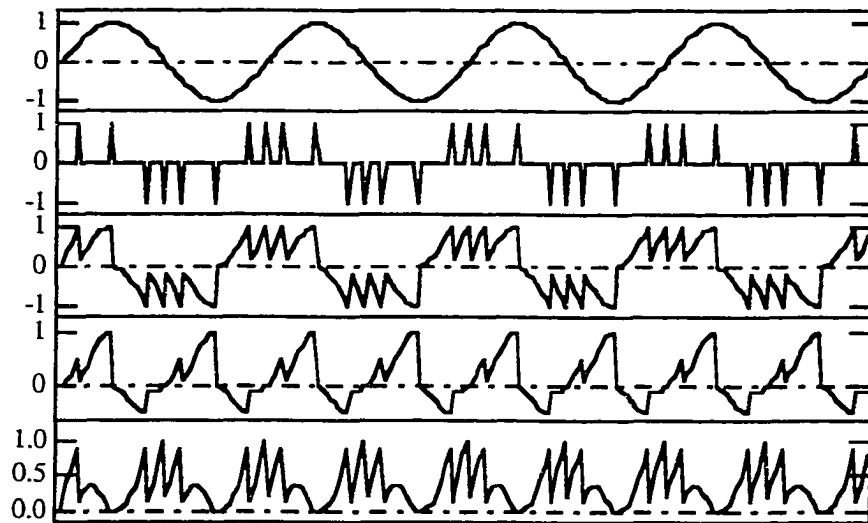
135

Fig. E.2. Expected consequences of sudden depinning when it happens at the half the maximum flux stretch. The plots are, from the top to down, the magnet displacement, the vortex velocity, the force on the vortex, the signal from channel 1 of a lock-in, and the signal from channel 2 of a lock-in.

F. RESONANCE PEAK CURVE FIT

The actual resonance peak of a double-torsional oscillator could be curve fitted perfectly using the formula for a simple, damped, forced oscillator. First I would like to derive the oscillation amplitude formula. As we have seen, the equation of motion for a simple torsional oscillator is the same as that for a simple harmonic oscillator if angle, torque, and moment of inertia will be replaced with displacement, force and mass, respectively. The equation of motion for a forced single harmonic oscillator is

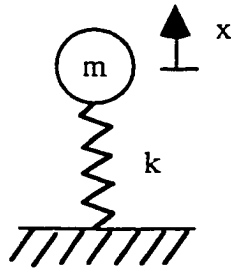$$m\ddot{x} + \gamma\dot{x} + kx = F_0 e^{-i\omega t}$$

136

Fig. F.1. A model for a simple harmonic oscillator. Each normal mode acts as a simple harmonic oscillator; hence one can use a simple harmonic oscillator formula to fit a resonance peak.

We are looking for a solution that has the same time dependence as the periodic external force; that is, $x = Ae^{i\omega t}$. By using this in the equation of motion, one gets

$$-m\omega^2 A e^{i\omega t} + i\gamma\omega A e^{i\omega t} + kAe^{i\omega t} = F_0 e^{i\omega t}.$$

From this and $k = m\omega_0^2$, the amplitude of oscillation can be found as

$$A = \frac{F_0}{m(\omega_0^2 - \omega^2) + i\gamma\omega}.$$

This can be approximated near the resonance using $\omega_0^2 - \omega^2 \approx 2\omega(\omega_0 - \omega)$,

$$A = \frac{F_0}{2m\omega}\frac{1}{(\omega_0 - \omega) + i\frac{\gamma}{2m}}$$

The real and the imaginary components of A are,

$$Re[A] = \frac{F_0}{2m\omega}\frac{\omega_0 - \omega}{(\omega_0 - \omega)^2 + \left(\frac{\gamma}{2m}\right)^2},$$

$$Im[A] = \frac{F_0}{2m\omega}\frac{-\frac{\gamma}{2m}}{(\omega_0 - \omega)^2 + \left(\frac{\gamma}{2m}\right)^2}.$$

There is always finite phase shift between the reference signal and the signals going into the lock-in. Denoting the phase shift by ϕ, the lock-in signal can be fit with

137

Channel 1 = Re[A] cosϕ – Im[A] sinϕ ,

Channel 2 = Re[A] sinϕ + Im[A] cosϕ .

When fitting data, offset has to be taken into account in addition to the equations above.

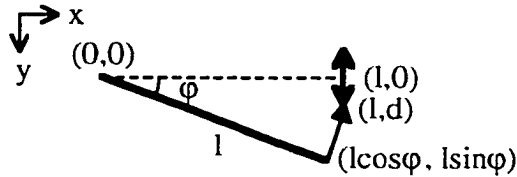## G. ENERGY TRANSFER FROM MAGNET TO OSCILLATOR

Fig. G.1.   Forces on an oscillator with an off-centered superconducting crystal when the magnet oscillates perpendicular to the oscillator plane.

Let us consider a simple torsional oscillator, although real oscillators are double-torsional ones. Assume that the magnet is moving perfectly perpendicular to the oscillator. In Fig. G.1, the position of the oscillator at rest is drawn with a dotted line. The equation of motion of this system is

$$K\phi + \eta\dot{\phi} + I\ddot{\phi} = \tau$$

where K, η, I and τ are the torsional coefficient, viscosity, the moment of inertia of the oscillator and the torque on the oscillator, respectively. The magnet oscillates between points $(l, -d_0)$ and (l, d_0) perpendicular to the oscillator. The vortex, meanwhile, is completely pinned in a superconductor, which is glued on the oscillator, at a distance l from the axis of rotation of the oscillator. Denoting the displacement of the magnet from its equilibrium by $d(t)$, the position of the magnet is therefore $(l, d(t))$ at time t. Since the vortex is completely pinned at

138

$(l\cos\varphi(t), l\sin\varphi(t))$ at time t, the magnetic flux line is stretched between the position of the magnet and that of the vortex. Assuming force due to stretched flux is proportional to the stretched amount, the force on the oscillator due to the stretched flux line is

$$\mathbf{F} = (k_p(l(1-\cos\varphi)), k_p(d-l\sin\varphi))$$

where k_p is the spring constant of the flux line stretch. In the coordinate system of the figure, the torque on the oscillator is therefore,

$$|\tau| = |\mathbf{r} \times \mathbf{F}| = |(l\cos\varphi(t), l\sin\varphi(t)) \times (k_p(l(1-\cos\varphi)), k_p(d-l\sin\varphi))|$$

$$= ld\cos\varphi - l^2\sin\varphi.$$

Now, since we are looking for a solution that has the same time dependence as the driving force, $\varphi = \varphi_0 e^{-i\omega t}$ and $d = d_0 e^{-i\omega t}$, where φ_0 and d_0 can be complex. Using approximations $\cos\varphi \approx 1$ and $\sin\varphi \approx \varphi$ for $\varphi \ll 1$, one finds that

$$\tau = ld_0 e^{-i\omega t} - l^2\varphi_0 e^{-i\omega t}.$$

Therefore, the equation of motion becomes

$$K\varphi_0 - i\omega\eta\varphi_0 - \omega^2 I\varphi_0 + k_p l^2\varphi_0 = ld_0 k_p.$$

Solving this equation one finds

$$\varphi_0 = \frac{ld_0 k_p}{K - \omega^2 I + l^2 k_p - i\omega\eta}$$

$$= \frac{ld_0 k_p / I}{(\omega_0^2 - \omega^2) - i\omega\eta/I},$$

where I have defined

$$\omega_0^2 = \frac{K + l^2 k_p}{I}.$$

Using the near-resonance approximation, i.e.,

$$\omega_0^2 - \omega^2 = (\omega_0 + \omega)(\omega_0 - \omega) \approx 2\omega(\omega_0 - \omega),$$

One finally finds that the amplitude of oscillation of the oscillator is

139

$$\phi_0 \approx \frac{\text{ld}_0\text{k}_p}{2\omega I}\left[\frac{\omega_0 - \omega + i\eta/2I}{(\omega_0 - \omega)^2 + (\eta/2I)^2}\right] .$$

This equation gives the phase difference between the magnet and the oscillator motions. If the frequency is much smaller than the resonant frequency ($\omega_0 \gg \omega$), then the oscillator motion ϕ_0 has the same sign as the magnet motion d_0. Thus, they have the phase difference of $0°$. On the other hand, if the magnet moves at much higher frequency than the resonant frequency of the oscillator, ϕ_0 and d_0 have opposite signs; thus the phase difference is $180°$. Strictly speaking, the phase difference cannot be exactly $0°$ or $180°$ due to the loss that is the imaginary part of the oscillator motion.
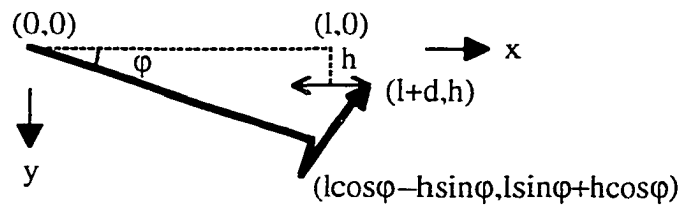

Fig. G.2.   Forces on an oscillator with an off-centered superconducting crystal when the magnet oscillates parallel to the oscillator plane.

The next case is when the magnet moves parallel to the oscillator. Of course, it would not exert any torque on the oscillator if it moves exactly on the plane of the oscillator. Therefore, I assumed that the magnet moves in parallel to the oscillator but with a finite offset h from the plane of the oscillator (see Fig. G.2). The basic idea is the same as the previous case; first we calculate the

140

torque on the oscillator due to the stretched flux lines, then we plug it in the equation of motion. The amplitude of the torque is

$$\tau = (-h^2\sin\varphi - l^2\sin\varphi - dl\sin\varphi - dh\cos\varphi)k_p.$$

Since we are looking for a solution that has the same time dependence as the driving force, we can write the oscillator angle as $\varphi(t) = \varphi_0 e^{-i\omega t}$ when the magnet displacement is $d(t) = d_0 e^{-i\omega t}$. The equation of motion is, therefore,

$$K\varphi + \eta\,\dot\varphi + I\ddot\varphi = (-h^2\sin\varphi - l^2\sin\varphi - dl\sin\varphi - dh\cos\varphi)k_p.$$

This becomes simply

$$\varphi_0[K - i\omega\eta - \omega^2 I + (h^2+l^2)] = (-l\varphi_0 d_0 e^{-i\omega t} - hd_0)k_p.$$

The time dependent term on the right hand side has an average of 0, so we can ignore this term. Then, the angle of oscillator is calculated as

$$\varphi_0 = \frac{-hd_0 k_p/I}{(\omega_0^2-\omega^2)-i\omega\eta/I} \; ,$$

where $\omega_0^2 = \dfrac{K + (h^2+l^2)k_p}{I}$. Again, using the near-resonance approximation, one gets

$$\varphi_0 \approx \frac{-hd_0 k_p}{2\omega I}\left[\frac{\omega_0 - \omega + i\eta/2I}{(\omega_0 - \omega)^2 + (\eta/2I)^2}\right] . \tag{G.2}$$

Comparison of Eqs. A.1 and A.2 is interesting. They suggest that the oscillator motion is proportional to the distance from the axis of rotation and the vortex (in the case of perpendicular magnet drive), or the distance between the plane of the oscillator and the magnet motion trajectory (in the case of parallel magnet drive). The magnitude of the oscillator motion, therefore, should be much larger with the perpendicular magnet motion than with the parallel magnet motion because $l \gg h$.

Let us now consider a physical explanation of the frequency dependence of the oscillator motion. When the magnet is moving at much smaller frequency

141

than the resonance frequency of the oscillator, the phase difference is ~0°, as we have seen above. This means that the oscillator is following the magnet. When the displacement of the magnet reached its maximum, the oscillator angle from its equilibrium also reaches its maximum. When the magnet is at its equilibrium position, the oscillator is also at its equilibrium position. While the angle is increasing from zero to its maximum, the directions of the force and of the motion of the oscillator are the same; thus, energy transfers from the magnet to the oscillator. In contrast, after the angle reached its maximum till the oscillator reaches its equilibrium position (angle = 0), the directions of the force and of the oscillator motion are opposite; thus, the oscillator actually does work on the magnet. Therefore, the time-averaged energy transfer is zero. In other words, oscillator gives back the energy that it receives.

When the magnet moves at much larger frequency than the resonant frequency, the magnet and the oscillator actually move in the opposite directions. So the phase difference is 180°. For example, the oscillator motion reaches its negative maximum when the magnet displacement reaches its positive maximum. In this case, while the magnet is moving from zero position to its maximum displacement, the force on the oscillator and the direction of the oscillator motion are opposite. Thus the oscillator is giving up energy to the magnet. While the magnet is decreasing its displacement to zero, the force on and the motion of the oscillator have the same direction, so the magnet is giving energy to the oscillator. Just as the previous case, the time-averaged net energy transfer is zero.

At resonance, the real part of the oscillator angle vanishes (Eqs. G.1 and G.2). The pure imaginary angle means that the phase difference between the

142

magnet motion and the oscillator motion is 90°. It is easier to picture in the perpendicular case; the sign of the imaginary part is positive, so the oscillator motion drags behind the magnet motion by 90°. For example, when the magnet reaches its positive maximum displacement, the oscillator is at its equilibrium position. Then, when the magnet comes back to its equilibrium, the oscillator reaches its maximum. Let us think qualitatively how energy transfer takes place in this case. Let us assume the moment when the oscillator is at its negative maximum position and the magnet is going through its equilibrium. After this moment until the magnet reaches its positive maximum displacement, the force on and the motion of the oscillator coincide. Thus, there's energy transfer from the magnet to the oscillator. After this, the displacement of the magnet begins to decrease while the displacement of the oscillator increases. But until their positions coincide, the magnet still gives energy to the oscillator. Only during the short time period until the oscillator reaches its positive maximum does the oscillator gives energy to the magnet. Therefore, the time-averaged net energy transfer is from the magnet to the oscillator. This is the qualitative explanation of why the oscillation gets larger at resonance.

H. DOPED YBCO

I tried to grow Zn-doped YBCO crystals. However, there was no way to know how much zinc would end up in crystals because we used a self-flux technique to grow crystals. We had success with Y:Ba:Cu = 1:4:10 flux to grow pure $YBa_2Cu_3O_{7-\delta}$ single crystals. Thus, we decided to grow Zn-doped YBCO

143

based on 1-4-10 flux. I set a target zinc concentration of 3 %. I thought of two cases. (1) If zinc goes into lattice sites preferably and thus if all zinc atoms end up in crystals, then Y:Ba:(Cu0.97 Zn0.03):Cu = 1:4:3:7 is enough. This is the same as Y:Ba:Zn:Cu=1:4:0.09:9.91. (2) But if zinc goes into crystals exactly the same rate as copper, then I have use a flux of Y:Ba:(Cu0.97 Zn0.03)=1:4:10. In other words, Y:Ba:Zn:Cu = 1:4:0.3:9.7. (3) But zinc might have more difficulty getting into lattice sites than copper. So I also prepared Y:Ba:(Cu0.94 Zn0.06)=1:4:10 flux. This is the same as Y:Ba:Zn:Cu = 1:4:0.6:9.4.

Extreme care was taken when mixing the chemicals. Since the amount of the dopant was so little, I first mix it with comparable amount of regular 1-4-10 mix of Y_2O_3, $BaCO_3$ and CuO. I gradually mixed in more 1-4-10. This way, little dopant could be distributed uniformly throughout the mix. After growing crystals in the same manner as pure YBCO crystals, their magnetic moments were measured as functions of temperature. The applied field was 1 Gauss parallel to c-axis. Fig. H.1 is a such SQUID measurement of a crystal grown from (1).

Table H.1   Zn contents in a flux and in lattice sites and Tc of Zn-doped YBCO

Zn/(Cu+Zn) in flux	0.9 %	3 %	6 %
Tc	86.5 K	73.5 K	64.0 K
Zn in lattice sites	0.3 %	1.7 %	2.5 %

144

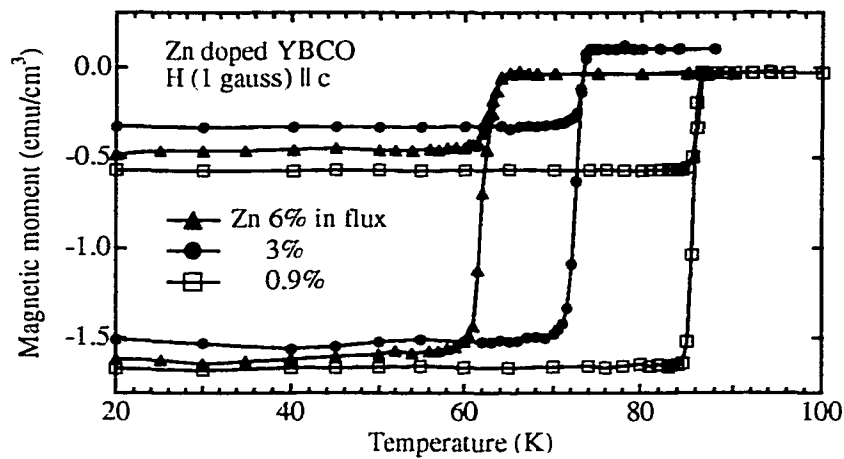Fig. H.1.   Relation between Zn contents and Tc of Zn-doped YBCO.[2]
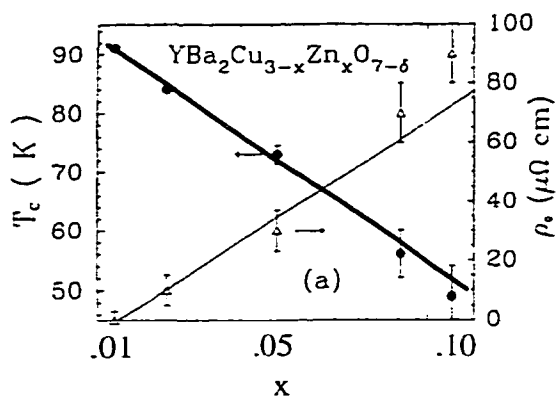

Fig. H.2.   Magnetic moment of
             Zn-doped YBCO
             crystals.

[2]T.R. Chien et al., Phys. Rev. Lett. **67**, 2088 (1991).

145

References

N. Alford, A. Templeton and S. Penn, Superdond. Sci. Technol. **11**, 703 (1998).

P. Ao and D.J. Thouless, Phys. Rev. Lett. **70**, 2158 (1993).

H. Asaoka et al., Jpn. J. Appl. Phys. **32**, 1091 (1993).

H. Asaoka et al., Phsica C **268**, 14 (1996).

L. Balents and D.R. Nelson, Phys. Rev. Lett. **73**, 2618 (1994).

J. Bardeen and M.J. Stephen, Phys. Rev. **140**, A1197 (1965).

A.L. Barr and J.T. Markert, Phys. Rev. Lett. **77**, 731 (1996).

A.L. Barr and J.T. Markert, J. Superconductivity **8**, 667 (1995).

A.L. Barr, K. Mochizuki and J.T. Markert, Czech. J. Phys. **46**, 1631 (1996).

A.L. Barr, Ph.D. thesis. (1996).

Blatter et al., Rev. Mod. Phys. **66**, 1125 (1994).

D.A. Bonn and W.N. Hardy, in Physical Properties of High Temperature Superconductors V, D.M. Ginsberg Ed., World Scientific, Singapore, 1996.

E.H. Brandt, P. Esquinazi, H. Neckel, J. Low Temp. Phys. **63**, 187 (1986).

E.H. Brandt, Phys. Rev. Lett. **68**, 3769 (1992).

F. Chang et al., Supercond. Sci. Technol. **6**, 484 (1993).

Chih-Wen Chen, Magnetism and Metallurgy of Soft Magnetic Materials, North-Holland P.C., Amsterdam, 1977.

P. Esquinazi, J. Low Temp. Phys. **85**, 139 (1991).

M.V. Feigel'man et al., JETP Lett. **62**, 834 (1995).

M.R. Geller et al., Phys. Rev. B **57**, R8119 (1998).

146

J. Giapintzakis et al., J. Low Temp. Phys. **77**, 155 (1989).

S.J. Hagen et al., Phys. Rev. B **47**, 1064 (1993).

H.E. Hall and J.R. Hook, Phys. Rev. Lett. **80**, 4356 (1998).

Y. Idemoto et al., Physica C **176**, 325 (1991).

W. Jiang et al., Czech. J. Phys. **46**, 1659 (1996).

G. Kaminsky, J. Val. Sci. Technol. B **3**, 1015 (1985).

Kirk-Othmer ed., Encyclopedia of Chemical Technology, Fourth Ed., Vol. 15, John Wiley & Sons.

N.B. Kopnin and M.M. Salomaa, Phys. Rev. B **44**, 9667 (1991).

N.B. Kopnin and A.V. Lopatin, Phys. Rev. B **51**, 16291 (1995).

A. I. Larkin and Yu. N. Ovchinnikov, Phys. Rev. B **51**, 5965 (1995).

R. Liang, D.A. Bonn, and W.N. Hardy, Physica C **304**, 105 (1998).

P. Mandal et al., Phys. Rev. B **43**, 13102 (1991).

S. Martin et al., Appl. Phys. Lett. **54**, 72 (1989).

M. McElfresh, Fundamentals of Magnetism and Magnetic Measurements, Quantum Design, 1994.

A.K. Niessen, F.A. Staas, and C.H. Weijsenfeld, Phys. Lett. **25 A**, 33 (1967).

K. Noto, S. Shinzawa, and Y. Muto, Solid State Commun. **18**, 1081 (1976).

P. Nozières and W. F. Vinen, Phil. Mag. **14**, 667 (1966).

A.V. Otterlo et al., Phys. Rev. Lett. **75**, 3736 (1995).

T.T.M. Palstra et al., Phys. Rev. B **38**, 5102 (1988).

R.B. Phelps et al., Phys. Rev. B **50**, 6526 (1994).

J.S. Schilling and S. Klotz, in Physical Properties of High Temperature Superconductors III, D.M. Ginsberg ed. World Scientific, Singapore, 1992, p.92.

G. Schröpfer et al., J. Micromech. Microeng. **7**, 71 (1997).

J. Shi, J.E. Berer and X. S. Ling, to be published.

E.B. Sonin, Phys. Rev. B **55**, 485 (1997).

S.E. Stupp and D.M. Ginsberg, in Physical Properties of High Temperature Superconductors III, D.M. Ginsberg ed. World Scientific, Singapore, 1992.

T. Tamegai et al., Jpn. J. Appl. Phys. **28**, L112 (1989).

D.J. Thouless, P. Ao and Q. Niu, Phys. Rev. Lett. **76**, 3758 (1996).

M. Tinkham, Introduction to Superconductivity, 2nd Ed., McGraw-Hill, New York, 1996.

V.I. Voronkova and Th. Wolf, Physica C **218**, 175 (1993).

C. Wexler, Phys. Rev. Lett. **79**, 1321 (1997).

X.-M. Zhu, E.Brändström and B. Sundqvist, Phys. Rev. Lett. **78**, 122 (1997).

M. Ziese, P. Esquinazi and H.F. Braun, Supercond. Sci. Technol. **7**, 869 (1994).

Vita

I was born in Yokohama, Japan on February 7, 1967 as the first child of Hisahiro and Tatsuko Mochizuki. I have always been proud of my home city and my parents. My home city is rich in history and in culture. My parents raised me in a very warm family. After graduating from Eiko High School, which was run by Jesuits and one of the best high schools in the nation, I attended the University of Tokyo in 1985. In my senior year during final exam week, I applied for a scholarship to The University of Illinois at Urbana-Champaign and was accepted. After receiving a Bachelor of Engineering from the University of Tokyo in 1989, I flew to the small city in the Midwest to study biophysics. Though the life in Illinois was fun, I found myself taking more physics courses than biology-related courses. Finally I decided to switch my major to pure physics. Though I had passed the qualifying exam, I left the university in 1992 with a Master's degree in biophysics. Then in the same year I joined the physics department of The University of Texas at Austin.

Permanent address: 907-19 Shimoiida, Izumi-ku, Yokohama 245, Japan

This dissertation was typed by the author.

IMAGE EVALUATION
TEST TARGET (QA-3)

150mm

6"
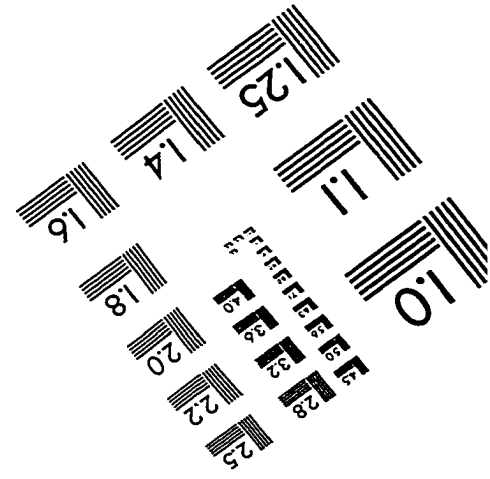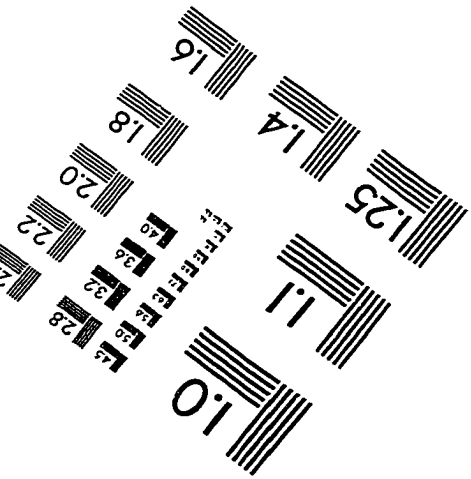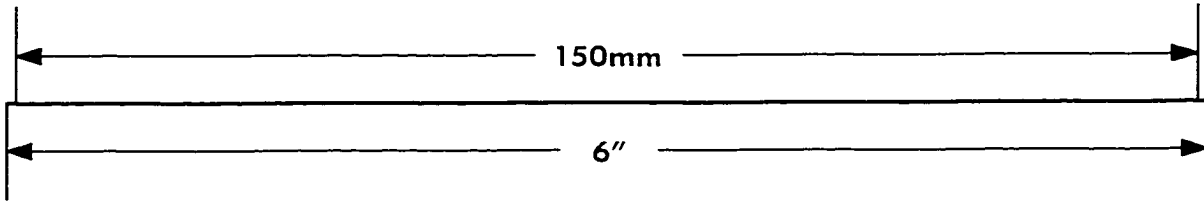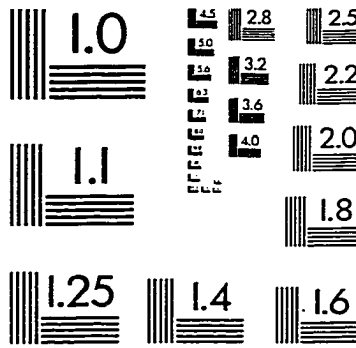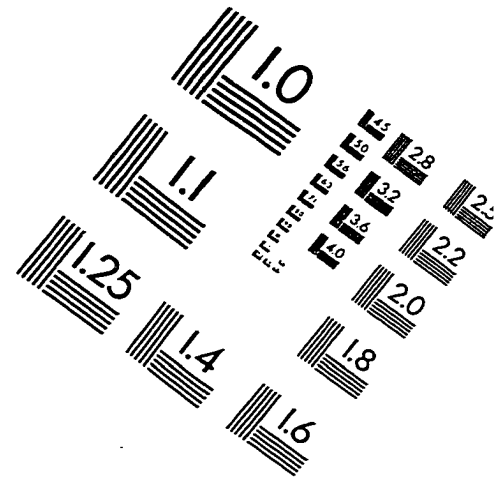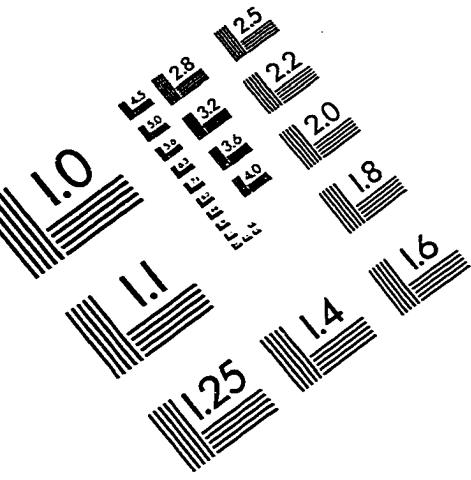
APPLIED ▟ IMAGE . Inc
1653 East Main Street
Rochester, NY 14609 USA
Phone: 716/482-0300
Fax: 716/288-5989

© 1993, Applied Image, Inc., All Rights Reserved